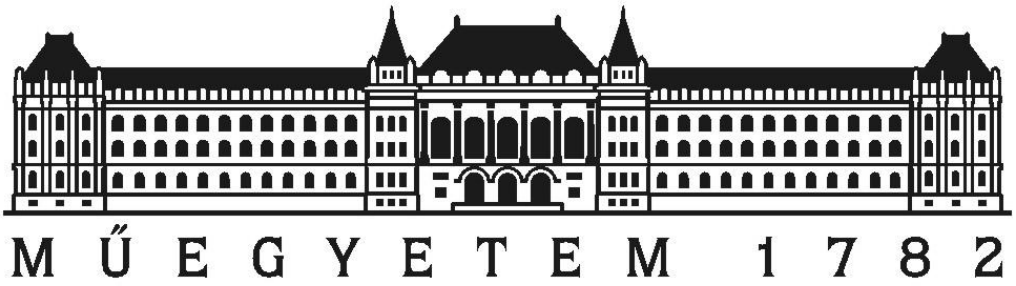

Budapest University of Technology and Economics
Faculty of Chemical Technology and Biotechnology

Master of Science Thesis

Preparation and characterisation of Pt based electrocatalysts for PEM fuel cells

by

Ilgar Ayyubov

External Supervisor: Dr. András Tompos
Internal Supervisor: Prof. Dr. Krisztina László
Consultant: Dr. Emília Tálas

Research Centre for Natural Sciences
Institute of Materials and Environmental Chemistry
Renewable Energy Research Group

2020

List of abbreviations

A.R.	**A**nalytical **R**eagent
AFC	**A**lkaline **F**uel **C**ell
AP	**A**uger **P**arameter
ATR-IR	**A**ttenuated **T**otal **R**eflection - **I**nfra**r**ed
BE	**B**inding **E**nergy
BET	**B**runauer–**E**mmett–**T**eller
BPs	**B**lack **P**earls
CNTs	**C**arbon **N**ano**t**ubes
CV	**C**yclic **V**oltammogram
DMFC	**D**irect **M**ethanol **F**uel **C**ells
DTG	**D**erivative **T**hermo**g**ravimetry
ECSA	**E**lectrochemical **S**urface **A**rea
EG	**E**thylene **G**lycol
FCEV	**F**uel **C**ell **E**lectric **V**ehicles
GC	**G**lassy **C**arbon
GO	**G**raphene **O**xides
HOR	**H**ydrogen **O**xidation **R**eaction
HTT	**H**igh **T**emperature Heat **T**reatment
IUPAC	**I**nternational **U**nion of **P**ure and **A**pplied **C**hemistry
KE	**K**inetic **E**nergy
LPG	**L**iquified **P**etroleum **G**as
MAS	**M**agic **A**ngle **S**pinning
MCFC	**M**olten-**C**arbonate **F**uel **C**ell
MWCNTs	**M**ulti-**W**all **C**arbon **N**ano**t**ubes
NMR	**N**uclear **M**agnetic **R**esonance
NPs	**N**ano**p**articles
NRR	**N**itrogen **R**eduction **R**eaction
ORR	**O**xygen **R**eduction **R**eaction
PEM	**P**olymer **E**lectrolyte **M**embrane
PEMFC	**P**olymer **E**lectrolyte **M**embrane **F**uel **C**ell
PAFC/FAFC	**P**hosphoric **A**cid **F**uel **C**ell
rGO	**R**educed **G**raphene **O**xides
RHE	**R**eversible **H**ydrogen **E**lectrode
SHE	**S**tandard **H**ydrogen **E**lectrode
SMSI	**S**trong **M**etal **S**upport **I**nteraction
SOFC	**S**olid **O**xide **F**uel **C**ells
SSA	**S**pecific **S**urface **A**rea
ST	**S**olvothermal **T**reatment
SWCNTs	**S**ingle-**W**all **C**arbon **N**ano**t**ubes
TEM	**T**ransmission **E**lectron **M**icroscopic
TG	**T**hermo**g**ravimetry
TGA	**T**hermo**g**ravimetric **A**nalysis
XPS	**X**-Ray **P**hotoelectron **S**pectroscopy
XRD	**X**-**R**ay Powder **D**iffraction

1. Introduction

The world population and industry are tremendously growing each year. Therefore, nowadays, one of the principal challenges is to meet humanity's ever-increasing energy needs by means of renewable energy sources to the greatest possible extent. Solar energy, wind energy or geothermal energy are only a few of them those can be shown as example. However, availability of all these renewable energy types varies through the whole world depending on the climate of the region, that the best climate for wind farms are in coastal areas, at the tops of rounded hills, open plains and gaps in mountains - places where the wind is strong and reliable or, period of the year, that solar energy is not effective in wintertime but in summertime, etc. Consequently, the sources of renewable energy and the use of renewable energy are often separated in space and time. A possible solution to this problem may be the conversion of renewable energies into chemical ones. This type of secondary energy sources can be stored and transported. High gravimetric energy density, abundance and storage potential make hydrogen a potential energy carrier [1].

Hydrogen can be one of the promising fuels for our future also because we are able to produce and utilize it in a clean, environmentally friendly way. The renewable primary energy sources can be used to generate electricity, from which hydrogen can be produced indirectly, *i.e.* the produced electrical energy can be converted into hydrogen with the electrolysis of water. Although the level of emissions to atmosphere is higher than that of the former approach, hydrogen can also be obtained from fossil resources by steam reforming [2]. The steam reforming process leads to conversion of hydrocarbons (from natural gas and LPG to liquid fuels including naphtha and in some cases kerosene) with steam into hydrogen, carbon oxides as main product, as well as methane, carbon monoxide, and unconverted steam mixture as by-products [3]. Thus, on-site reforming of natural gas might be a practical method to fuel the Fuel Cell Electric Vehicles (FCEVs) at fueling stations. However, high capital costs, high operation and maintenance costs, and design for manufacturing are the principal challenges of this approach. Since the critical issue for the hydrogen intended to be used as fuel in the fuel cells is purity not to poison the platinum-based catalyst of cell, the produced hydrogen output must have high purity, or further purification processes must be integrated, especially to remove carbon monoxide [2]. Hydrogen can be stored and transformed, when necessary, into electrical energy in fuel cells with high efficiency.

Fuel cells can have a wide range of size and power, varying from tiny devices producing few watts to huge power plants generating MWs of electricity. All the fuel cells have a common design consisting of two electrodes which are separated by a solid or liquid electrolyte for ion exchange between cathode and anode. In addition, catalyst is used to enhance the reactions carried out on electrodes. Depending on the application and amount of energy to be produced there can be used different types of fuel cells which are mainly classified according to the electrolyte that is used in. Each type of the fuel cells requires particular materials and design depending on the application that they will operate in.

Polymer Electrolyte Membrane (PEM) fuel cells may play a particularly important role amongst fuel cells, given that they are suitable because of their size, relatively low operating temperature, and rapid start-up. However, progress needs to be made in the material science development of individual fuel cell components, such as electrocatalysts, which have a significant impact on the cost of technology, environmental sustainability, and equipment lifespan. Technology can expect a significant market role if it competes with the other technologies in both price and technical performance.

PEM fuel cells operate with a platinum catalyst, the price of which is a significant item in large production costs. Commercially available platinum catalysts with carbon support are used in the PEM fuel cells. Although the decline in Pt content has been significant over the past decade, one direction of research and development remains to reduce the amount of platinum used (up to zero, by developing platinum-free electrodes). Also, at the heart of the improvements is the upgrading of the stability and lifespan of catalysts and electrodes made from them. According to the literature, the stability of electrodes can be improved primarily by increasing the stability of the catalyst support.

Carbon based support has an excellent conductivity but is prone to corrosion, especially when the electrode's potential fluctuates due to rapid load changes (*e.g.* as a vehicle's energy source). Carbon monoxide sensitivity of the catalyst on the anode side as a result of fuel oxidation is another issue to be solved. Currently, a significant part of the hydrogen used as fuel is still derived from the reforming of hydrocarbons, which as a result always contains carbon monoxide as a catalyst poison. Therefore, the development of anode-side catalysts with increased CO-tolerance is another important part of this task.

The staff of the Renewable Energy Research Group (hereinafter: research group) at the Institute of Materials and Environmental Chemistry of the Research Centre of Natural Sciences is working to address these challenges, to which I have joined in my master work.

2. Literature

2.1 Fuel cells

Fuel cells are electrochemical devices that are used to generate electricity by converting chemical energy in fuels into electrical energy directly, favorable power generation with high efficiency and minimal environmental impact [4]. The chemical reactions that bring about the generation of electric energy take place on the electrodes: positive electrode where oxygen is reduced (cathode) and the negative one where the oxidation of fuel is carried out (anode). Fuel cell contains an ion conducting separator between the electrodes, an electrolyte, conveying the ions between them [5]**.**

The first description of fuel cells appeared at the middle of 19th century by Sir William Grove (1838) [6, 7] and by Christian Friedrich Schönbein (1839), [8, 9] though no practical use was found. More than 100 years later the first fully operating fuel cell (hydrogen-oxygen fuel cell) was designed and first demonstrated publicly by Francis Thomas Bacon in 1959 [10, 11]. That type of fuel cells was first used by NASA in the 1960's as part of the Gemini space program and on seven missions. Reactants of those fuel cells were pure oxygen and hydrogen gases; however, those electrochemical devices were small scale, expensive and commercially not opportune. NASA's interest together with the energy crisis in 1973 pushed further advancement of fuel cells and they have been started to be utilized in a numerous applications [11].

Nowadays several types of fuel cells exist. Fuel cells can be classified by the type of electrolyte they use:

- Proton exchange membrane fuel cells/polymer electrolyte membrane fuel cells (PEMFCs)
- Alkaline fuel cell (AFCs)
- Solid acid fuel cell (SAFC)
- Phosphoric acid fuel cell (PAFCs, FAFCs)
- Solid oxide fuel cells (SOFCs)
- Molten-carbonate fuel cell (MCFC)
- Direct methanol Fuel Cells (DMFCs)

Important data demonstrating the characteristics and some key features of the above fuel cell types are summarized in Table 1 (from Ref. [5, 10]). Beside them other varieties (*e.g.* solid acid fuel cell (SAFC), microbial fuel cells, etc.) and other classification (*e.g.* based on fuel (direct methanol fuel cells, direct ethanol fuel cells, etc.)) can also be found.

Table 1. Typical characteristics and other essential features of fuel cell types [5, 10]

Specific disadvantages	Specific advantages	Operation temperature (°C)	Major contaminants	Charge carrier	Typical fuel	Typical anode/ cathode catalysts	Typical electrolyte	Acronym	Fuel cell type
Complex water and thermal management Low-grade heat High sensitivity to contaminants Expensive catalyst	Highly modular for most applications High power density Compact structure Rapid start-up due to low temperature operation Excellent dynamic response	60-80	Carbon monoxide (CO)	H^+	Hydrogen	Anode: Platinum supported on carbon Cathode: Platinum supported on carbon	Solid Nafion®	***PEMFCs***	Proton Exchange Membrane Fuel Cells
Extremely high sensitivity to contaminants Pure hydrogen and oxygen required for operation Low power density Highly corrosive electrolyte leads to sealing issues Complex and expensive electrolyte management for mobile electrolyte systems	High electric efficiency due to fast reduction reaction kinetics Wide range of operation temperature and pressure Inexpensive catalyst Catalyst flexibility Relatively low costs	Below zero–230	Carbon dioxide (CO_2)	OH^-	Hydrogen	Anode: Nickel Cathode: Silver supported on carbon	Potassium hydroxide (KOH) water solution Anion exchange membrane (AEM)	***AFCs***	Alkaline Fuel Cells
Slow start-up Low power density Strict material requirements High thermal stresses Sealing issues Durability issues High manufacturing costs	High electrical efficiencies High-grade heat High tolerance to contaminants Possibility of internal reforming Eliminated electrolyte issues Fuel flexibility Inexpensive catalyst	800–1000	Sulphides	O^{2-}	Methane	Anode: Nickel–YSZ composite Cathode: Strontium-doped lanthanum manganite (LSM)	Solid yttria-stabilized zirconia (YSZ)	***SOFCs***	Solid Oxide Fuel Cells
Slow start-up Low power density Electrolyte corrosion and evaporative losses Corrosion of metallic parts Air crossover Catalyst dissolution in electrolyte Cathode carbon dioxide (CO_2) injection requirement	High electrical efficiencies High-grade heat High tolerance to contaminants Possibility of internal reforming Less strict material requirements Fuel flexibility Inexpensive catalyst	600–700	Sulphides Halides	CO_2^{3-}	Methane	Anode: Nickel Chromium (NiCr) Cathode: Lithiated nickel oxide (NiO)	Liquid alkali carbonate (Li_2CO_3, Na_2CO_3, K_2CO_3) in Lithium aluminate ($LiAlO_2$)	***MCFCs***	Molten Carbonate Fuel Cells
Low cell voltage and efficiency Low power density Lack of efficient catalysts for direct oxidation of methanol Fuel and water crossover Complex water management High catalyst loading High cost Fuel toxicity	Compact size Simple system High fuel volumetric energy density Easy fuel storage and delivery Simple thermal management for liquid methanol systems	Ambient-110	Carbon monoxide (CO)	H^+	Liquid methanol–water solution	Anode: Platinum–Ruthenium supported on carbon Cathode: Platinum supported on carbon	Solid Nafion®	***DMFCs***	Direct Methanol Fuel Cells
Relatively slow start-up Low power density High sensitivity to contaminants Expensive auxiliary systems Low electrical efficiencies Relatively large system size Electrolyte acid loss Expensive catalyst High cost	Technologically mature and reliable Simple water management Good tolerance to contaminants High-grade heat	160-220	Carbon monoxide (CO) Siloxane Hydrogen sulphide (H_2S)	H^+	Hydrogen	Anode: Platinum supported on carbon Cathode: Platinum supported on carbon	Concentrated liquid phosphoric acid (H_3PO_4) in silicon carbide (SiC)	***FAFCs***	Phosphoric Acid Fuel Cells

Energy generating appliances fuel cell systems are mainly compared to the other energy supplying tools such as internal combustion engines and batteries. Fuel cells offer unique advantages over the systems mentioned above and at the same time have some disadvantages with respect to them.

One of the most principal advantages of the fuel cells over heat engines is their efficiency. Thermodynamic efficiency of combustion engines is related to the difference between the inlet and outlet temperatures of engine; however, the inlet temperature is limited by material considerations of the system and outlet temperature is ambient temperature that leads to limitation on the engine efficiency, too. Since, combustion is not the way fuel cells run on, their efficiency is not related to their maximum operating temperature. Therefore, their power conversion efficiency might be considerably higher. Overall system efficiency characteristics of fuel cells are compared with other electric power generating systems in Figure 1 (Figure 4-2 in Ref. [11]).

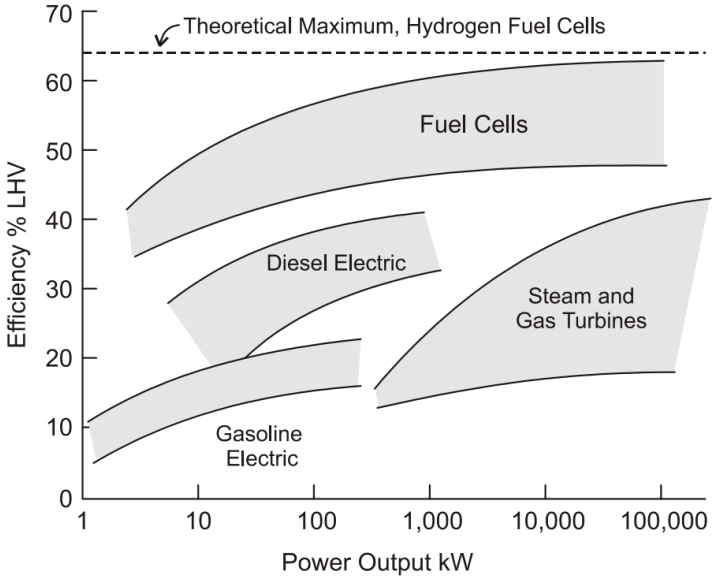

Figure 1. Power Generating Systems Efficiency Comparison *(Figure 4-2 in Ref* [11]*)*

In addition to electrical power, fuel cell systems produce clean hot water and medium-grade heat, both of which can potentially be used in co-generation applications such as domestic or industrial applications fuel cells. It also heightens the overall efficiency by combining efficiencies of all these systems [11].

Fuel cells are more suitable for electric energy generating devices rather than mechanical energy generating applications comparing with the heat engines. Because fuel cells utilized to generate electrical energy require a small number of energy transformations comparing with heat engines, in contrast, in case of fuel cell systems used for mechanical energy generation an equal number of the energy transformations are involved. Since each energy conversion leads to an associate energy loss, the fewer the energy transformations, the better the efficiency. Therefore, applications requiring electrical energy as the end product are more supremely suitable for fuel cells rather than

mechanical energy generating applications. Comparative energy transformations for each type of the energy producing systems in case of both electrical and mechanical energy output are demonstrated in Figure 2 (Figure 4-3 in Ref. [11]).

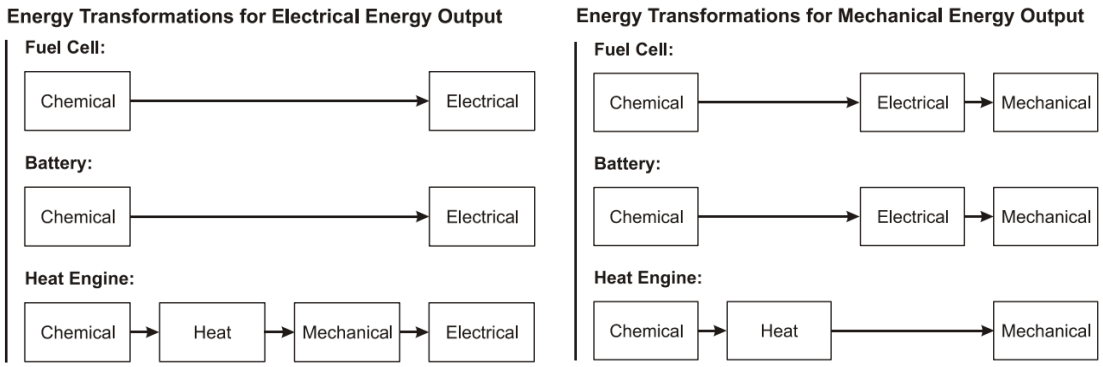

Figure 2. Comparative energy transformations *(Figure 4-3 in Ref.* [11]*)*

Comparing to batteries a benefit of fuel cells systems is that recharging is not required in them. Instead, fuel cells must be re-fueled, which is more rapidly carried out than charging a battery. In addition, depending on the size of the storage tank this feature can provide greater range for the application [11].

Fuel cells operating with hydrogen as fuel have further benefits because they run without pollution, the only by-products are pure water and heat. If fuel cells run on hydrogen-rich reformate gas mixtures some harmful emissions can be emitted but level of their emissions is much lower than that of internal combustion engine using conventional fossil fuels.

Certain types of fuel cells (PEMFCs, DMFCs) operate relative low temperature. These fuel cells are especially suitable for devices those run at low temperatures. The low temperature operation considerably reduces warmup time, avoids hazards caused by high temperature, and the thermodynamic efficiency of the electrochemical reaction gets better, too.

The applications of the fuel cells are categorized in three main groups according to their purpose of utilization and degree of power generated ranging from micro-fuel cells with less than 1W power outputs to power plants with more than 100 MW output [10]. Annual shipped units and megawatts by application types of fuel cells are demonstrated below in Figure 3 (Data sourced from Ref. [12]) and Figure 4 (Data sourced from Ref. [12]), accordingly.

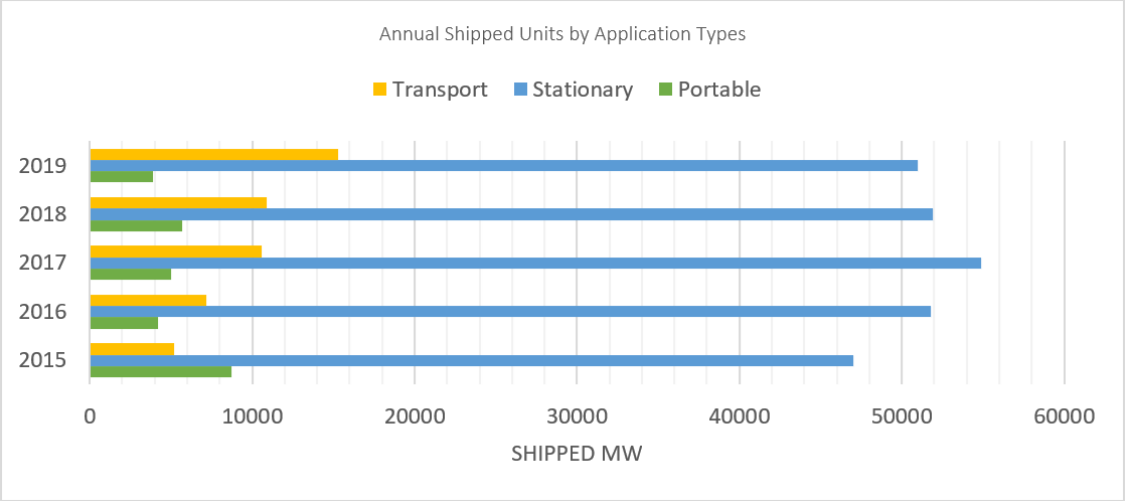

Figure 3. Annual shipped units by application types of FCs *(Data sourced from Ref.* [12]*)*

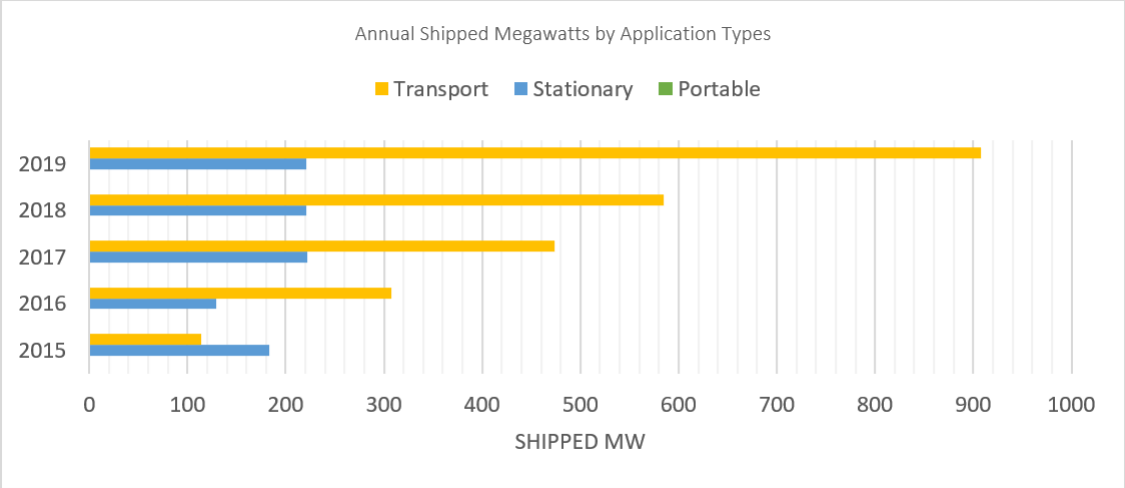

Figure 4. Annual shipped Megawatts by application types of FCs *(Data sourced from Ref.* [12]*)*

As it is demonstrated in the Figure 4 annually the most shipped megawatts belong to the transportation appliances. Buses for city and territorial carriage are viewed as the most probable kind of such vehicles for an early market presentation of fuel cell innovation. Generally, more power is required for the buses comparing with the passenger cars with about 150 kW or more power. In any case, the typical efficiency of a bus fuel cell system is approximately 15 % superior to that of a diesel motor [13, 14]. Another perspective market for the fuel cell technologies is scooters and bicycles market, especially in developing countries. During 2005–2010, such fuel cell scooters successfully and extensively used by the manufacturers themselves in Taiwan. [15, 16, 17, 18, 19]. Table 2 (Figure 16 of Ref. [10]) lists the applications those fuel cell systems have been utilized in.

Table 2. List of fuel cell applications *(Data sourced from Ref.* [10, 12]*)*

Application type	Portable applications	Stationary Applications	Transportation Applications
Definition	Units that are built into, or charge up, products that are designed to be moved, including small auxiliary power units (APU)	Units that provide electricity (and sometimes heat) but are not designed to be moved	Units that provide propulsive power or range extension to a vehicle
Typical power range	1 W to 20 kW	0.5 kW to 2 MW	1 kW to 300 kW
Example	Portable power generators Consumer electronics Portable military equipment Battery chargers Miniature toys Kits Gadgets	Distributed power generation Combined heat and power Combined cooling, heat, and power Back-up power supply	Auxiliary power units Light traction vehicles Light fuel cell electric vehicles Heavy fuel cell electric vehicles Marine propulsion Aerial propulsion

The global fuel cell race heated up by starting or stepping up of fuel cell development programs by many main developed world governments in the beginnings of 2000s, as illustrated in Figure 5 (Figure 6 in Ref [20]).

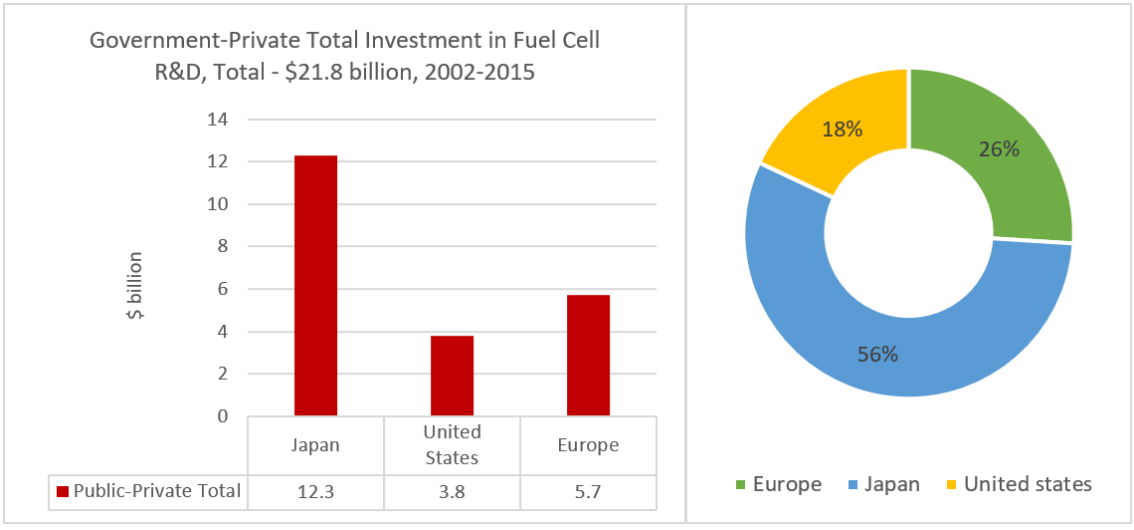

Figure 5. Estimated combined public and private-sector fuel cell R&D investment, 2002–2015, by Japan, Europe, and US *(Figure 6 in Ref.* [20]*)*

2019 has been a landmark year for fuel cells as the shipments globally grew significantly up to 1.1 GW. Hyundai and Toyota are the major corporate players with

their NEXO and Mirai models respectively, and these two companies together accounts for approximately two-thirds of total shipments by MWs [12].

Figure 6. Top seller fuel cell electric vehicles (FCEVs); A: Hyundai NEXO *(sourced from https://tech.hyundaimotorgroup.com/gallery/hyundai-nexo)*, B: Toyota Mirai *(sourced from https://www.toyota.co.uk/new-cars/new-mirai/meet-mirai)*

2.1.1 Polymer electrolyte membrane fuel cells (PEMFCs)

Figure 7 (Data sourced from Ref. [12]) demonstrates the PEMFCs are becoming the most popular fuel cells, since solid electrolytes used in these fuel cells have unique characteristic of conducting protons (H^+ ions) [21].

Figure 7. Annual shipped units (left) and megawatts (right) by fuel cell types *(Data sourced from Ref.* [12]*)*

PEM fuel cells operate at relatively low temperatures, usually between 60 ºC and 100 ºC [22]. These fuel cells are built using polymer electrolyte membranes (particularly Nafion®; partially meets numerous requirements such as good proton conduction,

electrical insulation, thermal, mechanical and chemical stability) as proton conductor and Platinum-based catalysts mostly deposited on the electrode (but more recently in some projects, on the proton conducting membrane) [5, 6, 22]. High power density, light weight compact structure, more sensitivity characteristic, rapid start-up process, small size, no requirement for maintenance work and no emissions of the greenhouse gases to the atmosphere as compared with other types of fuel cells makes transportation the main application sector of PEM fuel cells [6, 22, 23].

In PEMFCs, molecular hydrogen is distributed from a gas-flow stream activated by catalyst to be oxidized and form proton by ejecting an electron at the anode. The formed protons migrate from the anode to the cathode through the acidic electrolyte membrane while electrons are forced to flow to the external circuit, thus, electric current is generated. At the cathode, the electrons and the hydrogen ions interact with the oxygen delivered from an external gas-flow stream to form water. The chemical reactions occurring at each electrode and overall redox reaction are presented in the following equations (1), (2) and (3) [5, 10, 22, 23, 24]:

Reaction in anode (oxidation):

(1) $2H_2 \rightarrow 4H^+ + 4e^-$

Reaction in cathode (reduction):

(2) $O_2 + 4H^+ + 4e^- \rightarrow 2H_2O$

Overall reaction (redox):

(3) $2H_2 + O_2 \rightarrow 2H_2O$ + Electricity + Heat

The basic working principle of a typical PEMFC is illustrated in Figure 8 (Figure 5 in Ref. [23]).

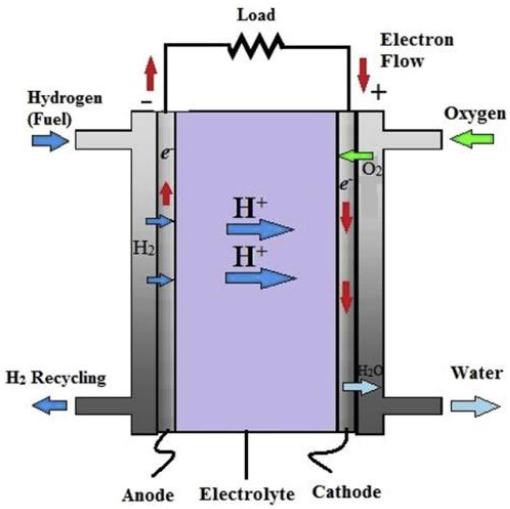

Figure 8. Schematic design of PEM fuel cell *(Figure 5 in Ref.* [23]*)*

While the higher efficiency or no emissions of ecology contaminating gases such as SO_x, NO_x, CO_2, CO, and lack of noise are the benefits of fuel cells in comparison with energy generating systems based on fossil fuels, the only drawback of fuel cells is their higher cost. In order to solve this issue and to supply the market decreasing Pt content of

the stacks, innovative technological solution based on disruptive materials in stack components and mass production exceeding a critical number are being applied. [25]

2.2. Electrocatalysts for polymer electrolyte membrane fuel cells (PEMFCs)

As electrocatalysis takes place at the interface of the electrode the electrocatalytic reaction rate depends on activity of the electrocatalyst and double layer on the electrolyte [26]. Usually, platinum nanoparticles (NPs) loaded on a carbon support (Pt/C) are the first choice both on anode and cathode site as a fuel cell mostly benefiting from its higher catalytic activity and better stability comparing with other noble metals in strongly acidic electrolytes. However, demanding operating conditions can affect the electrocatalytic activity and stability of catalyst, since platinum can easily be dissolved and aggregated [27]. This problem has been compensated with increased amount of Pt which is expensive. In the 1960s, when the fuel cell is started to be utilized in Gemini Pt loading was several mg cm^{-2}. In the end of the 1980s this amount was decreased to 2–4 mg cm^{-2} with Pt black in Ballard's Mark V, but still it was large amount for such expensive metal with limited resource [26]. Thus, researchers focused on introducing another component and/or catalyst support to the catalyst in order to increase fuel cells' lifetime and reliability and decrease their cost to make them commercially available in mass market.

2.2.1 State of art catalyst for polymer electrolyte membrane fuel cells (PEMFCs)

Limited platinum resource and high cost of Pt led to the discovery of carbon supported Pt alloys that built by replacement of pure platinum by transition metals with higher electrochemical surface area and higher activity for oxygen reduction reaction (ORR) [26, 28]. Conductivity of the proton exchange membrane might be declined if the metal would leach into the membrane. This drawback constrains the types of Pt alloys for PEMFCs to more stable metal alloys such as PtCr, PtZr, PtTi [29], PtSn [30, 31], PtMo [32] or PtRu [33] those are not leached into the electrolyte. Since even ppm CO content in the fuel can lead to the platinum poisoning PtRu referred to in the literature as the most modern CO tolerant PEMFC catalyst and is commercially available and, as the best such oxophilic metal, has already been widely studied [34]. Because Ru nearby Pt atoms can promote the CO anti-poisoning properties of them [27, 35]. However, despite its good catalytic properties, ruthenium has a relatively high cost and dissolves easily [26]. In the case of Pt-Ru/C catalysts dissolution of ruthenium can be enhanced and it may be dissolved from the surface of catalyst in sulfuric acid solutions at potentials of 0.9 to 1.0 V (SHE) as a result of corrosion [24].

2.2.2 Problems of activated carbon supported electrocatalysts

Hydrogen used as a fuel in PEMFCs is mainly produced by reforming of hydrocarbons which is the most economical and widespread method on an industrial scale at this moment. The hydrogen obtained in this way inevitably contains very small amounts of

carbon monoxide which adversely affects the operation of fuel cells: CO molecules irreversibly bind to the surface of the platinum catalyst, thereby preventing the electrochemical reaction from taking place. In addition, CO molecules also reduce the activity of the remaining free sites through dipole interaction. This problem can be solved by a catalyst that allows the oxidation of CO occupying active sites at a potential less positive than that of pure platinum, thus contributes to the release of active sites required for the oxidation of hydrogen [36].

In addition to CO tolerance, catalyst stability is also an important issue. Many studies report that the main reason of the decline in the performance of PEMFCs is loss in Pt electrochemical surface area (ECSA) by time [37, 38, 39] as a result of dissolution of Pt catalyst particles and the corrosion of the carbon support [40]. Although Pt is quite stable, there is a range where it dissolves in electrolyte rapidly when potential fluctuates from ca. 0 V (*vs.* RHE) reaching high positive values, too, in start up shut down processes [37]. Agglomeration and growth of nano-sized platinum particles in long-term PEMFC operation leads to decline in electrochemical surface area of the catalyst and lowers the oxygen reduction reaction activity [41].

According to the recent studies Pt catalyzes not only the target reaction, but also the corrosion of the carbon support [42, 43]. Fast load change conditions in fuel cell operations may lead to corrosion of active carbon even with platinum metals [44], and thus overall activity of the catalyst tend to be gradually lost, and turn into less active catalysts [45]. The complete electrochemical carbon-support corrosion (oxidation) by water is a four-electron process with the production of four protons and proceeds as given in equation (4) [46, 47]:

(4) $C + 2H_2O \rightarrow CO_2 + 4H^+ + 4e^-$ $\quad E=0.207V$ (vs. RHE)

Even if a small overpotential exists, the complete oxidation of carbon to CO_2 by water may be catalyzed at potentials as low as 550 mV versus the reversible hydrogen electrode (RHE) [48]. According to the early studies of phosphoric acid fuel cells CO_2 is generated through the intermediate formation of carbon surface oxides [49]. Recent studies on PEMFCs concluded in the similar results [50].

Therefore, one of the main research directions is the development of a suitable stable catalyst support. In general, the requirements of support materials are as follows: (i) high surface area, (ii) low electrical resistance, (iii) strong interaction between the Pt nanoparticles and the support, (iv) a pore structure suitable for fuel or oxidant contact and by-product release, and (v) high corrosion resistance across the anticipated potential/pH window.

Carbon offers most of the primary required features such as its availability, high surface area and good electrical conductivity. However, since carbon is lacking in resistance to corrosion, major technical barriers for PEMFCs particularly in the appliances with high power demand origin from use of carbon supports; the electrode integrity and durability [51].

2.3 New approaches to prepare active and stable electrocatalyst

As platinum based and carbon supported catalysts suffer from severe disadvantages regarding stability and tolerance to CO poisoning researchers keep exploring new and alternative materials those can distribute further improvements to the catalyst to overcome these drawbacks.

By use of graphitic, nano-structured carbon materials, such as graphene nano-sheets, carbon nanotubes, and carbon nanofibers as catalyst supports stability of electrodes from corrosion can be improved [52, 53]. As these compounds have high degree of graphitized structures resistance to chemical and electrochemical oxidation is enhanced while providing adequate conductivity. Detailed review of the new types of carbonaceous materials will be given in Chapter 2.4

Ceramic catalyst supports such as titanium-oxides [54, 38], molybdenum-nitride [55], tungsten-oxide [56] can improve mechanical properties, thermal stability, chemical corrosion resistance, though their properties do not include good electrical conductivity and high surface area [47]. The role of TiO_2 and molybdenum-oxides will be detailed in the following subchapter (2.3.1)

Recent studies suggest that some problems with the Pt/C system can be overcome using a second oxophilic metal. In general, reactive hydroxyl groups are more easily formed on the oxophilic dopant material than on platinum, which not only increases the hydrogen oxidation reaction rate [57, 58], but also slows down the oxygen reduction process, making the catalysts selective to hydrogen oxidation reaction (HOR) vs. oxygen reduction reaction (ORR) on the anode side [59, 60]. It has importance in the start up process when there is still air on the anode side as well. Its reduction at low potentials (close to 0 V *vs.* RHE) has to be suppressed, which is a big challenge. Moreover, the doped metal is less noble than Pt, consequently, water is activated at lower potential and formation rate of CO_2 is accelerated [42].

2.3.1 Metal oxides for electrocatalyst supports

Metal oxides are inorganic compounds with several compatible properties those are used for catalyst supports in order to improve the qualities of fuel cells. Supports containing additional components such as molybdenum-oxide [61], tungsten-oxide [42, 62], titanium-oxides [63] and others were synthesized. According to these studies, molybdenum or tungsten oxides as components of platinum electrocatalysts have a number of beneficial properties [64, 65, 66].

Although reducing oxides of oxophilic metals are indeed valuable co-catalysts or carriers for PEMFC electrocatalysts, their dissolution is always cause for concern in the operational conditions of the metal cations that dissolve may bind to the polymer membrane, resulting in a decrease in proton conduction [67].

Regarding the effect of molybdenum oxides, the enhanced CO tolerance of the electrocatalysts has to be mentioned. It is well known that the CO can adsorb on the

surface of platinum very strongly and block the active sites of catalyst for hydrogen oxidation reaction, a second oxophilic surface metal can help to overcome this drawback [68, 45]. It has to be mentioned that beside Mo other transition metals have been studied as alloys to improve the CO tolerance of platinum-based catalysts, for instance, W or Sn [26]. Mo is very promising metal regarding its co-catalytic characteristics. Although Mo has a beneficial co-catalytic feature in the electrooxidation of CO and alcohols, its behavior is very complex as it can be present in several oxidation states and different solubility conditions and can form various oxides [69]. In literature, information on the stability of molybdenum-containing catalysts is still contradictory. While some studies report the dissolution of non-alloyed molybdenum as a result of a few voltammetric cycles [70], other studies show that stable forms of molybdenum are present even after several cyclisation between 0 and 1.2 V potential limits [71]. In the study of Pt_4Mo/C catalysts [72] it was found that the CO oxidation process is accompanied by oxidation of Mo^{x+} (x=4 or 5) into MoO_3, and this oxide of molybdenum dissolves easily in the electrolyte. When catalytic polarization is used, it is separated again with electrochemical reduction followed by regaining its catalytic activity. When testing Pt_xMo_y/C catalysts, it was found that the bond between metals stabilizes molybdenum on the surface of anode in practical use [73]. Although at potentials over 0.4 V molybdenum oxidizes to Mo^{+6}, and dissolves in the case of pure metal, in the case of alloys, molybdenum in this oxidation state is stabilized on the surface due to bonding between metals. It has been reported that $Pt_{0.8}Mo_{0.2}$ alloy electrocatalysts effectively improve the performance of the anode side electrode as well as have higher CO tolerance and stability [74]. According to the research results, it is possible to mitigate leaching by a well-ordered alloy or core–shell catalyst architecture with a seemingly pure Pt surface [45]. It was found that strong metal support interaction (SMSI) between platinum and MoO_3 significantly improves the stability of electrocatalysts [59, 60].

The role of TiO_2 can be related to the improvement of the stability of the electrocatalyst. The stability and corrosion resistance of TiO_2 itself is well known. TiO_2 is non-toxic oxide with high mechanical, chemical and redox stability [75, 76]. However TiO_2 is an n-type semiconductor [42] having a wide band gap (3.0–3.5 eV) and therefore its conductivity is insufficient for a support material without modification such as doping [47]. The n-type dopants such as transition metals with higher oxidation states than that of Ti^{4+} (*e.g.* W, Nb and Ta) have been extensively used for doping of titania to increase its electrical conductivity [62]. Combination of TiO_2 with conductive carbonaceous materials is also widely used to reach the desired conductivity of the electrocatalyst support.

Beside own stability TiO_2 can also stabilize metals in a highly dispersed state [77]. The strong interaction between the TiO_2 coating on carbon and the Pt results in drastically increased electrochemically active surface area (ECSA) of the Pt and inhibits the agglomeration and corrosion of the metal nanoparticles [78, 79, 80]. Preparation of stable TiO_2 thin films on carbon nanotubes [81, 82] or on microfibrous carbon paper [83] is feasible, giving enhanced activity towards oxygen reduction reaction (ORR, cathode reaction). Decreasing of the micropore volume in mesoporous carbon by the TiO_2 coating

can positively influence the catalytic behavior [84, 85, 86]. Composite support materials, such as TiO_2-C also show improved stability in accelerated aging tests [86, 87, 88].

Dissolution problem of oxophilic metals can be eliminated by incorporation of them into the TiO_2-rutile lattice. Mixed oxides produced in this way have been shown to be stable under electrochemical tests [68]. According to the literature there are three main polymorphic phases of titanium dioxide: rutile, anatase and brookite [42]. Previous studies of the research group has shown that formation of the rutile phase titanium dioxide on catalyst support before the high temperature treatment is a prerequisite for the complete oxophilic metal incorporation into the rutile lattice [48, 68].

Although mixed oxides of oxophilic metals with TiO_2 provided stabile catalyst supports but their specific surface area (SSA) and conductivity remained still substantially lower than that of carbon. In order to increase the conductivity, mixed oxides were mechanically mixed with carbon powder [89]. Even more favorable catalytic properties could be achieved by formation composite type support materials developed by the co-workers of the research group [45].

2.4 New carbonaceous materials: their properties and use for composites

Recently, new types of carbonaceous materials like carbon nanotubes (CNTs) graphene, reduced graphene oxides (rGOs) have been reported to provide extreme good properties to TiO_2-carbonaceous composites due to their special electronic structure.

2.4.1 Carbon nanotubes

CNTs are one of the allotropes of carbon. Single-wall carbon nanotubes (SWCNTs) were discovered independently by Iijima and Ichihashi [90] and Bethune et al. [91] in carbon arc chambers. SWCNTs have diameters in the range of a nanometer. Multi-wall carbon nanotubes (MWCNTs) consist of nested single-wall carbon nanotubes [92]. SWCNTs and MWCNTs have long been considered promising catalyst carriers [93]. Their composites formed with TiO_2 have most frequently used as photocatalysts [94, 95, 96, 97, 98] etc. Great number of electrocatalytic application of CNTs has also been described [99]. Some examples are given below. TiO_2-MWCNT composite supported Pd catalyst has been prepared for electrocatalytic oxidation of formic acid [100]. In another work of TiO_2/CNTs composite was used as an anode material for lithium-ion batteries [101]. In direct ethanol fuel cell Pt-sulfated–TiO_2/MWCNT catalysts have shown higher catalytic activity for ethanol oxidation compared with Pt supported on non-sulfated TiO_2/MWCNT composites and commercial Pt/C catalysts [102]. TiO_2-nanowire/MWCNT composite has shown enhanced performance and durability for polymer electrolyte fuel cells [103]. MWCNT support for fuel cell electrocatalyst has exhibited a significantly enhanced cycling durability compared to the Vulcan XC 72R support of comparable BET surface area [104]. Pt supported by MWCNTs@TiO_2–TiC mixed support has exhibited both higher activity and stability [105]. Oxygen reduction reaction (ORR) activity and long-term stability of platinum nanoparticles supported on

TiO_2-CNT composites have also been reported [106, 107]. Microwave assisted synthesis Pt/CNT electrocatalyst proved to be beneficial for PEMFC [108]. General feature of the electrocatalysts prepared from TiO_2-carbon nanotube composite supported catalyst is the enhanced corrosion stability. However, a close connection between the hydrophilic TiO_2 and the strongly hydrophobic carbon nanotube must be ensured in order to prepare a well-functioning TiO_2-carbon nanotube composite. Upon composite preparation pristine carbon nanotube is subjected to various oxidative treatments or other surface modifications [109].

2.4.2 Graphene

Graphene is a nanostructured allotrope of carbon. Ideally, graphene is a one-atom-thick layer of graphite formed by carbon atoms in a honeycomb array. Graphene is considered to be an infinite aromatic giant molecule or an extreme size polycyclic aromatic hydrocarbon, too [110]. It was originally observed in electron microscopes in 1962, but only studied while supported on metal surfaces [111]. The material was later rediscovered, isolated, and characterized in 2004 by Novoselov et al. [112] at the University of Manchester. Graphene exhibits outstanding physicochemical properties, including: (i) an extremely large specific surface area (up to ca. 2,600 m^2g^{-1}); (ii) a very high mobility of the charge carriers (more than 200,000 $cm^2V^{-1}s^{-1}$). These features distinguish graphene from conventional graphitic carbon that is characterized by significantly lower specific surface area and mobility of charge carriers [113]. These features have made graphene a very promising candidate for the development of electrocatalysts [113, 114, 115]. For example, graphene powder with less than three graphene layers was applied for the preparation of TiO_2-functionalized graphene nanosheets supported Pt catalyst. Pt/TiO_2-functionalized graphene nanosheets utilized for a catalyst activity investigation toward ORR exhibited a relatively high electrocatalytic activity for the four-electron reduction of oxygen to water [116]. Multi-layer graphene can be synthesized by (i) epitaxial growth, (ii) chemical vapor deposition, (iii) solvothermal synthesis and (iv) electrochemical exfoliation which can be used as catalyst and support in the electrochemical energy conversion [99]. Chemical methods for the production graphene were summarized in a recent review by Park and Ruoff [117].

Although there are many examples for the application of graphene in composite preparation, the most common precursor for the preparation of the so-called graphene–metal oxide nanohybrid materials is graphene oxide or other name exfoliated graphite oxide [113]. Graphene oxide can be chemically/electrochemically reduced to multi-layer graphene with various reducing agents including hydroquinone, hydrogen sulfide, sodium borohydride and hydrazine hydrate. However, the multi-layer graphene produced by exfoliation exhibits lower conductivity due to chemical process-induced defects and attached chemical groups [99].

Based on the literature [118] the formation and nomenclature of new carbon materials derived from graphite are summarized in Figure 9.

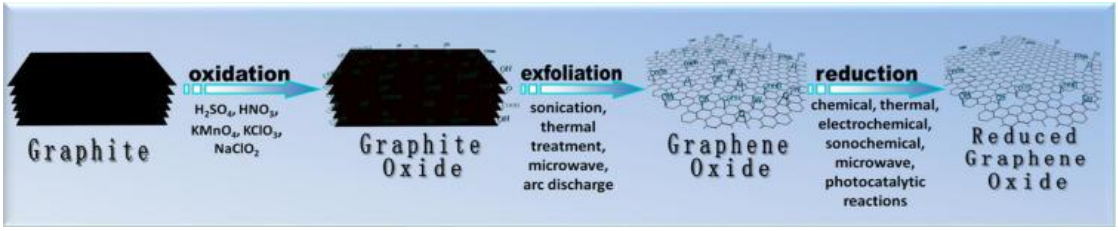

Figure 9. Formation and nomenclature of graphite derived new carbon materials *(from Ref* [118]*)*

2.4.3 Reduced graphene oxides (rGOs)

GO is an inorganic compound although it contains carbon, oxygen and hydrogen in variable ratios but it does not contains C-H bonds. GO can be prepared from graphite by electrochemical oxidation [119] or by use of strong oxidizing agents. Two main chemical oxidation procedures exist *i.e*. Brodie's method [120] and the Hummers-Offeman method [121]. According to Brodie's method $NaClO_3/HNO_3$ while to the Hummer's method $KMnO_4$, H_2SO_4, $NaNO_3$ is used. Besides, developed versions of these methods are also used [122]. GO preserves the layer structure of the parent graphite, but the interlayer spacing is about two times larger than that of graphite. The structure of GO depends on the type of the oxidation method [123, 122]. Interlayers spacing of Hummer's and Brodie's GO are 6.6-6.7 Å and 6.0 Å, respectively. Hummer's GOs is likely to contain small amount of S and Mn. GO is a non-stoichiometric compound; Brodie found that the empirical chemical formula of GO was $C_{2.19}H_{0.80}O_{1.00}$ [120] while that of well-oxidized samples was found to be C_4O_2H [124].

Since its discovery, various models have been created to describe the structure of the GO, taking into account the results of continuously evolving structure analysis methods. These models, *i.e.* the Hofman (1938) [125], Ruess (1946) [126], Scholz-Boehm (1969) [127], Nakajima-Matsuo (1988-94) [128, 129], Lerf-Klinovski (1996-98) [130, 131] model are shown in Figure 10. In the Hofmann model epoxy groups spread across the basal planes of graphite were supposed. In order to account the hydrogen content of GO, the Ruess's model incorporated hydroxyl groups, too. Furthermore, the sp^3 hybridized system was supposed rather than sp^2. The Scholz-Boehm model suggested regular quinoidal species in a corrugated backbone. The model by Nakajima and Matsuo assumed a lattice framework akin to poly(dicarbonmonofluoride), $(C_2F)_n$, which forms a stage 2 graphite intercalation compound. The recent models of GO focused on a nonstoichiometric, amorphous alternative. The Lerf-Klinovski model was created on the basis of solid-state NMR results. According to the authors, the compound contained two domains in random distribution: (i) alicyclic parts consisting of oxidized six-membered rings (ii) aromatic areas consisting of condensed benzene rings protected from oxidation. The ratio of the two domains depended on the degree of oxidation. NMR data indicated that the functional groups on the oxidized part of the GO were tertiary alcohols and ethers, most likely 1,2-ethers (*i.e.* epoxides). Based on infrared spectroscopic data the revised Lerf–Klinowski model also supposed the presence of carboxylic acid groups in very low quantities at the periphery of the graphitic platelets, in addition to other keto groups. One

of the newest models of GO was created by Szabó and coworkers (Figure 11) [124]. According to this model two distinct domains exist: trans-linked cyclohexyl species interspersed with tertiary alcohols and 1,3-ethers, and a corrugated network of keto/quinoidal species. It was also hypothesized that the quinones introduce rigidity and plane boundaries and were a possible source of the macroscopic wrinkling of the platelets commonly seen in TEM images.

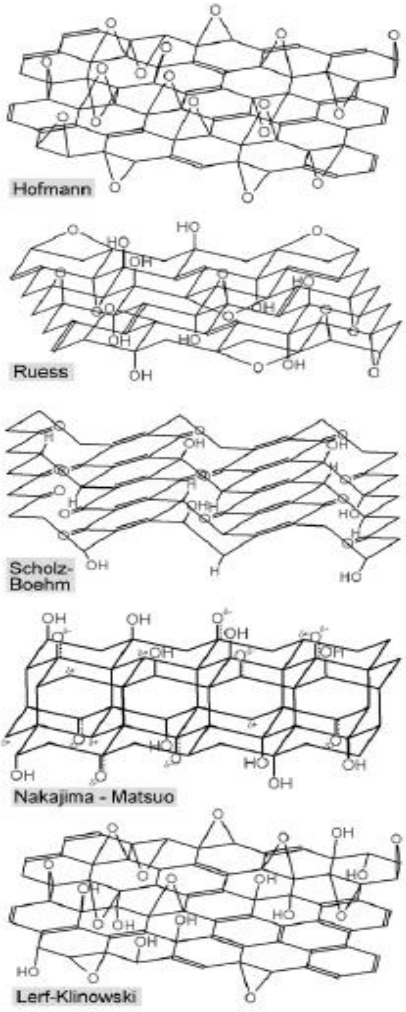

Figure 10. Different models for the description of the structure of GO *(from Ref.* [124, 132]*)*

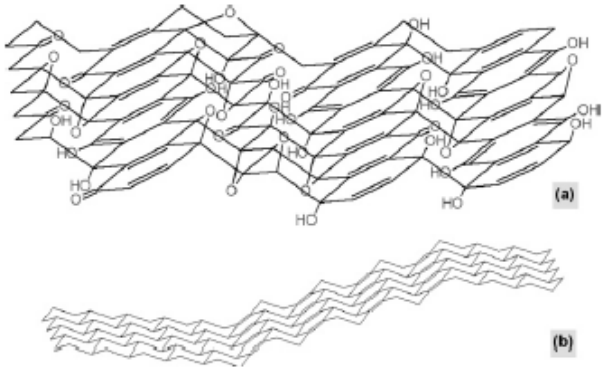

Figure 11. Model of GO by Szabó and coworkers *(from Ref.* [124]*)*

GO is weakly acidic material [133] due to its O and H-containing functional groups which are covalently attached to the carbon skeleton [124, 134]. Due to its O-containing functional groups GO is highly hydrophilic unlike the hydrophobic graphene [118]. The hydrophilic GO is capable of swelling in the presence of damp and other polar liquids or dispersible therein. The GO is thermally unstable; it decomposes slowly at relatively low temperatures (60-70°C) with formation of CO, CO_2, H_2O and turbostratic carbon. The turbostratic word means describing a crystal structure in which basal planes have slipped out of alignment. The turbostratic carbon has been considered as a unique class of carbon having structural ordering in between that of amorphous carbon phase and crystalline graphite phase [135]. Thermal instability of GO could be associated with the exothermic decomposition reactions of oxygen-containing groups in the basal plane and periphery of graphite layers [136]. The decomposition of GO under very slow heating could be regulated but an increased heating rate could lead to thermal explosion [136]. The phenomenon was also called as deflagration. A great amount of formed gaseous products lead to the delamination of GO particles, a sudden decrease in the oxygen content of the material, and the formation of a certain type of turbostratic carbon, a graphene-like substance with high specific surface area [137]. It has been also described that the oxygen-containing groups of GO were generally decomposed in three temperature regions of 170–250, 500–600, and 750–1000 °C [136]. The above carbonaceous materials of extra-large surface area obtained by "thermal exfoliation" were regarded as candidates for hydrogen storage [138].

Regarding TiO_2–carbonaceous material composites derived from GO, functional groups of GO provide reactive and anchoring sites for nucleation and growth of nanomaterials when TiO_2 is *in situ* prepared in the presence of GO [139, 140, 141]. The intimate contact between the graphitic carbon material and the metal oxide in the TiO_2-GO systems can be provided by electrostatic interactions [142, 143], but chemical bond formation between Ti-OH and functional groups of GO is also suggested [144]. Solvothermal or more frequently hydrothermal procedure is (*i.e.* treatment with organic solvents such as alcohol or with the mixture of water and ethanol at elevated temperature in autoclave) used in order to connect pre-prepared TiO_2 nanoparticles to GO sheet [145, 146, 147], while reduced rGO (considered as GO derived graphene) is formed. During this treatment the O-containing functional groups of GO were removed [144] which led to re-establishment of conjugated graphene network [148] and led to possible appearance of C-O-Ti bonds [149, 146, 144, 150]. Consequently, solvothermal or hydrothermal treatment provided excellent properties to TiO_2-rGO composites.

The key point for usage of GO is its exfoliation also known as delamination. Different methods, such as sonication, thermal treatment, microwave treatment, etc., can be used for the above purpose [118]. Sonication is a clean and comfortable method to separate the GO sheets from each other however it is successful only in case of Hummers's GO. Sonication itself is not satisfactory for delamination of Brodie's GO [123, 151]. Slightly basic conditions can help to achieve larger degrees of dispersion, because GO layers decorated with functional groups with the same negative charge repel each other [133].

The advantage of GO as starting material for composite preparation is that GO is a relatively cheap compound, it is easily available and suitable for mass production. Huge amount of work deals with the preparation and characterization of GO derived TiO_2–carbonaceous material composites on the field of photocatalysis [152, 153, 118, 154, 155] etc. Electrocatalytic applications also can be found, some examples are listed below. TiO_2 nanoparticles–reduced graphene oxide hybrid (TiO_2–rGO) has been described to behave as an efficient non noble-metal N_2 reduction reaction (NRR) electrocatalyst for N_2-to-NH_3 conversion with excellent selectivity [156]. TiO_2 nanofibers heterogeneously wrapped with reduced graphene oxide were found as efficient Pt electrocatalyst support for methanol oxidation [144]. Pd-TiO_2/rGO hybrid catalysts with uniform Pd and TiO_2 nanoparticles supported has been synthesized by an easy green route via a two-step process using deionized water as solvent merely, first hydrothermal synthesis and then reducing reaction under room temperature. This new type of electrocatalyst showed improved activity in methanol oxidation [157]. Pt/graphene-TiO_2 hybrid catalysts have been synthesized by a one-pot solvothermal method. Single fuel cell tests showed the maximum power density of the direct methanol fuel cell using Pt/graphene-TiO_2 as the anode catalyst is increased by 55 % compared with that using Pt/graphene catalyst at the same operating conditions. The significantly enhanced electrochemical performance could be ascribed to (i) the synergetic effect between Pt, graphene and TiO_2; (ii) strong metal-support interaction (SMSI) between Pt nanoparticles and TiO_2 [158]. A Pt/graphene-TiO_2 catalyst prepared by a microwave-assisted solvothermal method exhibited a significant improvement in activity and stability towards the oxygen reduction reaction compared with Pt/C [159]. N-doped TiO_2 nanorods/graphene nanocomposite, which comprise the N-doped TiO_2 nanorods (40–60 nm diameter and 90–300 nm length) and self-assembled nitrogen-doped graphene networks has been successfully synthetized by use of GO starting material prepared by Hummer's method. Above nanocomposite exhibited great ORR activity and long durability and methanol tolerance than that of the commercial 20 % Pt/C catalyst [160]. A unique electrocatalyst composed of a dimensionally stable anode of graphene oxide and rGO combined with RuO_2 and TiO_2 nanoparticles has been synthesized [161]. Graphene oxide obtained from graphite by the modified Hummers's method could be used to improve the electrocatalytic performance of dimensionally stable anodes. The rGO was obtained from GO by hydrazine reduction method [161].

Among the new types of carbonaceous materials, the carbon aero gels with their beneficial pore structure also have to be taken into account as electrocatalyst support. For example, GO containing resorcinol-formaldehyde and resorcinol-formaldehyde-melamine polymer aerogels were converted to carbon aerogels were tested in ORR. When both N and graphene were present in the matrix, the dominant pathway of ORR changed from the 2-electron pathway to the 4-electrone one [162].

3. Objectives

The production and testing of heterogeneous platinum based electrocatalyst for PEMFCs has been targeted with high carbon monoxide resistance, sufficient stability, and high electrocatalytic activity.

I have set a goal to prepare electrocatalysts based on former results obtained over novel composite supported $Pt/Ti_{(1-x)}Mo_xO_2$-C (C= active carbon) electrocatalysts developed by the research team, which showed better stability and increased CO tolerance compared to the state-of-art PtRu/C catalyst.

As new types of carbonaceous materials reduced graphene oxides have been reported to provide extreme good properties to TiO_2-carbonaceous composites due to their special electronic structure, my work has aimed the preparation of a novel $Ti_{0.8}Mo_{0.2}O_2$-C (C= GO derived carbonaceous material) composite type of catalyst support. For this work I have used GO obtained from graphite by modified Hummers's method. In order to adapt to GO, the preparation method commonly used in the research group has to be modified taking into consideration (i) the effect of unavoidable presence of $NaNO_3$, (ii) the effect of the high temperature treatment on the GO derived carbonaceous part of the composite and (iii) the effect of the basic solution of exfoliated GO on the formation of crystalline phase.

To design the intended electrocatalyst, 20 wt.% platinum loading has been planned onto the $Ti_{(1-x)}Mo_xO_2$-C (x=0.0, 0.2; C=active carbon, GO derived carbonaceous material) composite type catalyst supports. The catalytic properties of the new electrocatalysts have been compared to those of commercially available 20 wt.% platinum-based carbon supported Quintech catalyst, which is one of the most commonly used catalysts in PEMFCs.

The new types of composites have to be characterized by physical-chemical methods such as XRD, TEM, ^{13}C NMR, ATR-IR, TG, and XPS techniques. To find correlation between the electrochemical behavior (carbon monoxide tolerance, activity, and durability) and the structure of the newly prepared electrocatalysts is one of the important missions.

4. Experimental

4.1 Materials used

Table 3-6 summarize the chemical compounds and gases used for the work presented here.

Table 3. Chemical compounds used for the preparation of catalyst supports

Material	Chemical formula/ Abbreviation	Purity	Manufacturer/ Distributor
Milli-Q Water	H_2O	Millipore, 18.2 MΩ cm	MTA TTK AKI
Nitric acid (65 %)	HNO_3	a.r.	Molar Chemicals
Titanium (IV) isopropoxide	Ti(O-*i*-Pr)$_4$	97 %	Sigma-Aldrich
Ammonium heptamolybdate tetrahydrate	$(NH_4)_6Mo_7O_{24}$*$4H_2O$	99 %	Sigma-Aldrich
Sodium hydroxide	NaOH	>98 %	Sigma-Aldrich
Graphite oxide (Hummers' method)	GO (I) GO (II)	3.2 wt.% 0.95 wt.%	University of Szeged (Tamás Szabó)
Black Pearls Active Carbon	BP	-	CABOT

Table 4. Chemicals used in platinum loading

Material	Chemical formula/ Abbreviation	Purity	Manufacturer/ Distributor
Hexachloroplatinic acid hexahydrate	H_2PtCl_6*$6H_2O$	37.5 % Pt	Sigma-Aldrich
Ethanol	C_2H_5OH	99.95 %	Molar Chemicals
Sodium borohydride	$NaBH_4$	99.99	Molar Chemicals
Ethylene glycol	$(CH_2OH)_2$	99.8 %	Molar Chemicals
Hydrochloric acid (37%)	HCl	-	Molar Chemicals

Table 5. Gases used in electrochemical measurements

Gas	Chemical formula/ Abbreviation	Purity	Manufacturer/ Distributor
Argon	Ar	5.0	Linde Gas Hungary Co
Hydrogen	H_2	5.0	Linde Gas Hungary Co
Carbon monoxide	CO	4.7	Messer Hungarogas

Table 6. Chemicals and materials used in electrochemical measurements

Material	Chemical formula/ Abbreviation	Purity	Manufacturer / Distributor
Milli-Q Water	H_2O	Millipore, 18.2 MΩ cm	TTK AKI
Sulphuric acid (96%)	H_2SO_4	PA	Merck
2-propanol	i-C_3H_5OH	99.9 %	Molar Chemicals
5% Nafion® dispersion	-	-	Dupont
20 wt.% Pt-based Catalyst	20 wt.% Pt/C	-	Quintech

4.2 Catalyst production

4.2.1 Preparation of catalyst support

In order to synthesize Ti-Mo mixed oxide/carbonaceous material composite or Ti-oxide/ carbonaceous material composite based catalyst supports I have carried out room temperature sol–gel-based multistep synthesis routes A, B, C, D and E as shown in Figure 12. In each synthesis method represented (excluding AI006), the nominal mass ratio of the metal oxide to the carbonaceous material was 75/25. In addition, Table 7 summarizes the quantities of the titanium and molybdenum precursors as well as amount of the carbonaceous material used in the production of support materials.

Table 7. Nominal composition of the $Ti_{(1-x)}Mo_xO_2$-C composites; the starting materials used in the synthesis

Name	Route	Ti $_{1-x}Mo_xO_2$/C nominal value	Ti/Mo nominal value	Ti(O-*i*-Pr)$_4$, cm^3	GO sol, g[a]; (wt.%)[b]	$(NH_4)_6Mo_7O_{24}\cdot 4H_2O$, g
AI001	**C**[c]	75/25	100/0	1.079	5.27 (3.20)	-
AI001/II	**C**[c]	75/25	100/0	1.079	5.27 (3.20)	-
AI001/III	**C**[c]	75/25	100/0	1.079	5.27 (3.20)	-
AI002	**C**[c]	75/25	100/0	1.079	17.78 (0.95)	-
AI003	**A**	75/25	100/0	1.079	0.100[d]	-
AI004	**C**	75/25	100/0	1.079	17.78 (0.95)	-
AI005	**D**	75/25	80/20	1.572	35.56 (0.95)	0.2344
AI005/II	**D**	75/25	80/20	0.786	17.78 (0.95)	0.1172
AI005/III	**E**	75/25	80/20	0.786	17.78 (0.95)	0.1172
AI006	**D**	80.5/19.6	80/20	1.079	17.78 (0.95)	0.1609
AI007	**B**	75/25	80/20	2.1	0.250[d]	0.299

[a]the amount was calculated on the $C_8O_4H_2$ general formula of GO, [b]concentration of GO in the sol, [c]sample is not washed with diluted HNO_3 after aging, [d]the carbonaceous material Black Pearls 2000 (Cabot) active carbon

In case of GO derived samples the volume of H_2O and cc. HNO_3 was calculated to adjust the concentration to 0.115 M for Ti(O-*i*-Pr)$_4$ and 0.69 M for HNO_3 in the first step of the preparation (5 h stirring).

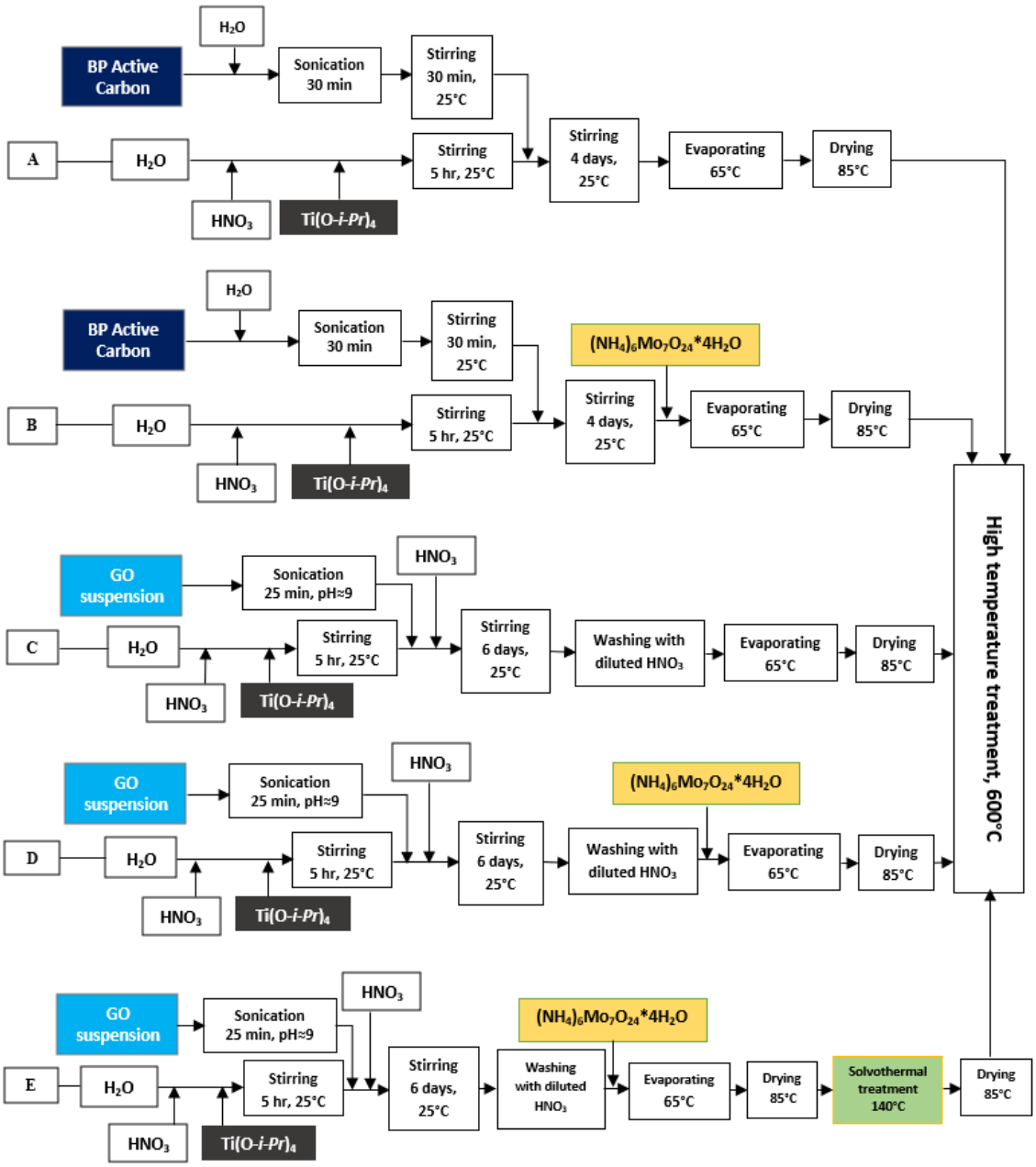

Figure 12. Flow charts for preparing carbon based composite support materials by using sol–gel-based multistep synthesis routes A, B, C, D and E.

Route A

In order to prepare the composite support containing TiO_2 and activated carbon in a mass ratio of 75:25 between the oxide and the carbon, first a transparent acidic TiO_2 colloidal solution was made by adding Ti(O-*i*-Pr)$_4$ into a vigorously stirred mixture of cc. HNO_3 and distilled water. After 5 h stirring at room temperature a sonicated activated carbon-water mixture was added into the transparent acidic TiO_2 colloidal solution. This

slurry was aged at room temperature for 4 days to facilitate rutile nuclei formation. After four days of aging, the mixture evaporated at 65 °C with further continuous stirring. At last, the synthesized sample was dried overnight in the oven at 85 °C.

Route B

In order to prepare the composite support containing mixed oxide with Ti/Mo atomic ratio of 80/20 ($Ti_{0.8}Mo_{0.2}O_2$) and activated carbon in a mass ratio of 75:25 between the oxide and the carbon, first a transparent acidic TiO_2 colloidal solution was prepared by adding Ti(O-*i*-*Pr*)$_4$ into a vigorously stirred mixture of cc. HNO_3 and distilled water. After 5 h stirring at room temperature a sonicated activated carbon-water mixture was poured into the transparent titanium oxide sol. The mixture was aged at room temperature for 4 days to facilitate rutile nuclei formation. After four days of aging, the molybdenum precursor compound [$(NH_4)_6Mo_7O_{24}\times4H_2O$] was added into the acidic solution. After 2 hrs of continuous stirring at room temperature the slurry was evaporated at 65 °C. As the last step, the evaporated sample was dried overnight in the oven at 85 °C.

Route C

In order to prepare the composite support containing TiO_2 and GO derived carbonaceous material with a mass ratio of 75:25, first a transparent acidic TiO_2 colloidal solution was made by adding Ti(O-*i*-*Pr*)$_4$ into the vigorously stirred mixture cc. HNO_3 and distilled water similarly as in route A and B. For exfoliation of GO NaOH solution (~pH14) was added to the GO suspension till its pH became ~9. Then the mild basic GO suspension was sonicated for 25 min. After that, rutile nucleus containing suspension prepared beforehand was poured to the GO suspension quickly under vigorous stirring. Then aqueous HNO_3 solution was added into the slurry and the reaction mixture was stirred continuously for 6 days at room temperature for aging in order to facilitate rutile nuclei formation. After six days of aging the mixture was centrifuged. The solid part was washed three times with diluted nitric acid in order to remove the well soluble $NaNO_3$. Finally, the slurry was prepared to the original volume with diluted HNO_3. After the removal of $NaNO_3$ the slurry was evaporated at 65 °C. As the last step, the evaporated sample was dried overnight in the oven at 85°C. For comparison samples without $NaNO_3$ removal were also prepared.

Route D

In order to prepare composite support containing mixed oxide with Ti/Mo atomic ratio of 80/20 ($Ti_{0.8}Mo_{0.2}O_2$) and GO derived carbonaceous material with a mass ratio of 75:25, a transparent acidic TiO_2 colloidal solution was prepared as written above. For exfoliation of GO NaOH solution (~pH14) was added to the GO suspension till its pH became ~9. This suspension was sonicated for 25 min. Then the rutile nucleus containing suspension prepared beforehand was poured to the GO suspension quickly under vigorous stirring. Then aqueous HNO_3 solution was added into the slurry and the reaction mixture was stirred continuously for 6 days at room temperature for aging in order to facilitate rutile nuclei formation. After six days of aging, the mixture was centrifuged. The solid part was

washed three times with diluted nitric acid in order to remove the well soluble $NaNO_3$. Finally, the slurry was prepared to the original volume with diluted HNO_3. After the removal of $NaNO_3$ the molybdenum precursor compound [$(NH_4)_6Mo_7O_{24}\times 4H_2O$] was added into the acidic slurry and it was stirred for 2 h at room temperature. After that the slurry was evaporated at 65 °C. As the last step, the evaporated sample was dried overnight in the oven at 85 °C.

Route E

The sample obtained from preparation route D (after the drying step) was solvothermally treated in order to make attempt to heat-stabilization of the GO part of the composite by removing reducible functional groups. The solid sample was sonicated in 2-propanol in a short time (5-10 min) then the slurry was placed into the autoclave. The autoclave was rinsed with nitrogen. Temperature inside the autoclave was heated up to 140 °C in ~1-1.5 h and kept at that temperature for ~3 h. Then the heater is turned off and the sample left to be cooled down. The reaction mixture was centrifuged, the solid part dried in air. As the final step, the sample was dried overnight in the oven at 85°C.

High temperature heat treatment

As a final step of synthesis of catalyst support material, high temperature heat treatment (HTT) is performed for the molybdenum incorporation: to replace the Ti^{4+} ions of rutile TiO_2 with Mo^{n+} ions. The heat treatment was performed under argon atmosphere by use of a quartz reactor fitted in to a furnace. HTT process consisted of several steps. In order to remove the oxygen from the system totally and to create an inert condition for avoiding burning out of the carbon content of composite materials the reactor was purged with Ar for 3 h at room temperature. Then, the temperature was increased from 25 °C up to 300 °C with the rate of 5 °C/min. After reaching 300 °C the sample was kept at this temperature for 1 h. In the following step, the sample was heated up to 600 °C in with rate of 1 °C/min and keep it under this condition for 8 h. As the last step, the furnace was turned off and let the sample to cool down in Ar flow. Figure 13 shows the temperature program of the furnace for HTT.

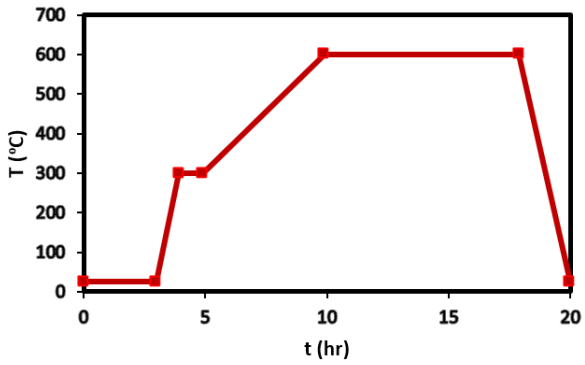

Figure 13. Temperature program for high temperature heat treatment (HTT)

Denominations of the samples from the different phases of the preparation are the following. The name used in Table 7 means samples after drying 85° C; Roman numeral

means parallel preparations with the same composition. ST means solvothermally treated sample while HT means high temperature heat treated sample. For example, AI005/III/ST/HT means the sample obtained at the end of route E. The name of the catalyst samples obtained with Pt load onto the above composite support is AI005/III Cat.

4.2.2 Introduction of platinum onto the support

The support materials were loaded with 20 wt.% Pt via a modified, sodium borohydride ($NaBH_4$) assisted ethylene-glycol (EG) reduction-precipitation method [62, 38] in order to obtain platinum containing electrocatalyst. The flowchart of this process can be seen in Figure 14.

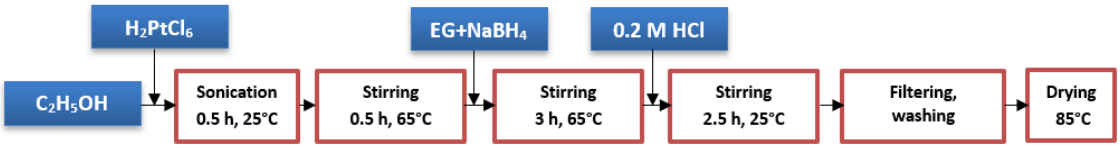

Figure 14. Platinum loading process flow chart

As a first step of preparation procedure, $H_2PtCl_6 \cdot 6H_2O$ was dissolved in ethanol (EtOH) in a round bottom flask. The support material was dispersed in the solution by sonication at room temperature and the suspension (EtOH + Pt precursor + support material) was heated up to 65 °C with continuous stirring. A mixture of $NaBH_4$ and ethylene glycol (EG) was added dropwise to the suspension very slowly and carefully with a syringe pump in 30 minutes at 65 °C under continuous stirring. After the addition of 30 minutes the system was stirred at 65 °C for 3 hours. Hydrogen chloride solution (HCl) was added to the suspension and it was stirred for an additional 2.5 hours at room temperature in order to allow the Pt particles to settle on the surface of the support. At the end of the experiment the sample was washed with distilled water and filtered by centrifugation four times in order to remove the chloride ions. Finally, the wet, mud-like material was dried at 85 °C in an oven overnight.

4.3 Chemico-physical characterization of the prepared materials

ATR-IR spectroscopy was used to characterize the functional groups of carbonaceous part of the composite samples in the penetration depth between 0.5 and 2 μm.

Raman spectra was performed to get detailed information about chemical structure of the catalyst supports, however the analysis did not provide any information as they were all in dark color and high level of fluorescence appeared.

Solid-state ^{13}C NMR spectroscopy with magic angle spinning (MAS) technique was used to determine the functional groups and the structure of the carbonaceous part of the composite samples in whole bulk phase.

X-ray photoelectron spectroscopy (XPS) measurements were carried out to determine the surface composition and chemical state of the elements on the surface of the composite samples.

I performed *X-ray powder diffraction (XRD)* analyses in order to characterize the crystalline structure of the oxide parts of the composite samples.

Nitrogen adsorption measurements were carried out to obtain adsorption isotherms and to calculate the specific surface area (SSA) of the composite supports by BET method.

Thermogravimetric (TG) measurement was carried out with the purpose of determining the ash content and inferring from this the carbon content of the composite samples.

Transmission electron microscopic (TEM) images were used to get information both about the carbonaceous part and the platinum nanoparticles loaded on the surface of the composites.

Details of the chemico-physical characterizations are described in the Appendix.

4.4 Electrochemical test

During the electrochemical test CO_{ads}-stripping and stability tests on electrocatalysts were performed using cyclic voltammetry technique. Biologic SP 150 potentiostat and standard three-electrode electrochemical cell with the electrolyte of 0.5 M H_2SO_4 solution inside were used. The 0.5 M H_2SO_4 solution was prepared by using Milli-Q water and concentrated H_2SO_4. Selected catalysts for electrochemical tests were the following: **AI003 Cat, AI004 Cat, AI005/II Cat, AI005/III Cat, AI007 Cat**.

Hydrogen electrode that immersed into the electrolyte was utilized as the reference electrode. Both the counter electrode (straight or spiral shaped platinum wire) and working electrode were immersed into the same electrolyte. Electrode potential values are given on the reversible hydrogen electrode (RHE) scale. In order to prepare the working electrode, a drop of catalyst ink with an amount of 3.6 µl was dripped on a freshly polished glassy carbon (GC) electrode and let to become dry in ambient conditions for 30 min. The geometric surface area of the GC electrode was 0.0707 cm^2 (d =0.3 cm).

In order to prepare catalyst ink, 2-3 mg of catalyst powder was dispersed in the same amount of 0.4 v/v% Nafion solution, 20 v/v% isopropanol and 79.6 v/v% Milli-Q water by sonication at room temperature. Duration of sonication was 30 min for active carbon derived samples and 2.5 h for GO derived ones.

Electrochemical measurements were performed at room temperature and before starting the test, argon was bubbled into the electrolyte for 30 min. After 30 min Ar purging, 10 cyclic polarization voltammograms (CVs) were recorded in a given potential range, typically between 50 and 1000 mV, with 10 mV/s or 100 mV/s polarization rate for the so-called ‘‘pre-leaching’’ procedure. During the measurements, the electrolyte was continuously purged with Ar.

Electrochemically active surface area (ECSA), *i.e.* the area of the platinum surface on which electrochemical reactions may occur can be determined from CVs in the so-called hydrogen underpotential deposition region, between 0-350 mV, according equation 5.

(5) $$ECSA_{Hupd}\ (cm^2) = Q_{ox_{Hupd}}\ (\mu C) / 210\ (\mu C/cm^2),$$

where $Q_{ox_{Hupd}}$ is the charge accompanies oxidation of underpotentially deposited hydrogen, while 210 μC is the charge necessary to oxidize monolayer of H atoms over 1 cm^2 Pt surface.

After conditioning the catalyst, CO_{ads}-stripping measurements were conducted. During these measurements, the potential of the working electrode was set to 50 mV and then CO was bubbled through the electrolyte for 15 minutes. While purging carbon monoxide through the electrolyte, CO is chemisorbed to the surface of the platinum. In the following step, the CO gas flow was replaced with argon by keeping the potential at 50 mV for the following 15 minutes. In that way, carbon monoxide dissolved in the electrolyte and physically adsorbed on the surface of the catalyst is removed. The working electrode is then subjected to 2 cyclic voltammetry scans at a polarization rate of 10 mV/s between 50 and 1000 mV potential limits, while argon is kept still flowing in the cell gas space over electrolyte. The carbon monoxide chemically adsorbed on the surface of catalyst was oxidized in the first polarization cycle. Finally, the second cycle of the voltammetry is recorded in which theoretically no CO oxidation peak can be recorded proving that all of the catalyst poisoning species was totally oxidized in the first cycle.

ECSA from CO_{ads}-stripping current peak can also be determined according to equation 6:

(6) $$ECSA_{CO}\ (cm^2) = Q_{ox_{CO}}\ (\mu C) / 420\ (\mu C/cm^2),$$

where $Q_{ox_{CO}}$ is the charge concomitant with electrooxidation of CO, while 420 μC is supposed to by the charge released in oxidation of monolayer CO chemisorbed over 1 cm^2 Pt.

In order to determine effect of aging onto ECSA, the first CO-stripping was followed by an aging process consisting of 500 polarization cycles at a 100 mV/s polarization rate in a range of 50 to 1000 mV potential and then CO_{ads}-stripping was recorded second time.

Commercially available Quintech catalyst with 20 wt.% Platinum on Active Carbon support Vulcan XC-72 was used as reference.

5. Results and Discussion

5.1 Effect of $NaNO_3$ on the composite preparation

$NaNO_3$ could appear on two reasons in the GO derived composite samples. One hand, the GO used as the carbonaceous component of catalyst support was prepared by $NaNO_3$ utilized Hummers-Offeman method. It is important to mention that GO(I) solution was purified by osmosis while GO(II) suspension was not purified from $NaNO_3$. On the other hand, NaOH was added for delamination of GO then delaminated GO was mixed with rutile nuclei formed in HNO_3 solution. It has to be mentioned that the introduced amount of NaOH was different in case of the delamination of GO(I) and GO(II) suspensions. In my early experiments 10 ml NaOH (pH= 9) was added to GO(I) suspension to delaminate it while in the series of experiments with GO (II) the whole volume of the GO (II) suspension was adjusted to pH 9 with concentrated NaOH solution for a better delamination.

The effect of $NaNO_3$ was investigated in case of samples AI001, AI002, AI004, *i.e.* in a series of TiO_2/GO composites without Mo introduction.

The appearance of AI002 sample differed from the others. It was difficult to grind, it looked to be crystalline, and its color was shiny gray. Soaking in water changed its character. These findings let us to conclude that crystalline $NaNO_3$ was present. We used XRD measurements to prove the presence of crystalline $NaNO_3$. Figure 15 shows the XRD pattern of this series of samples.

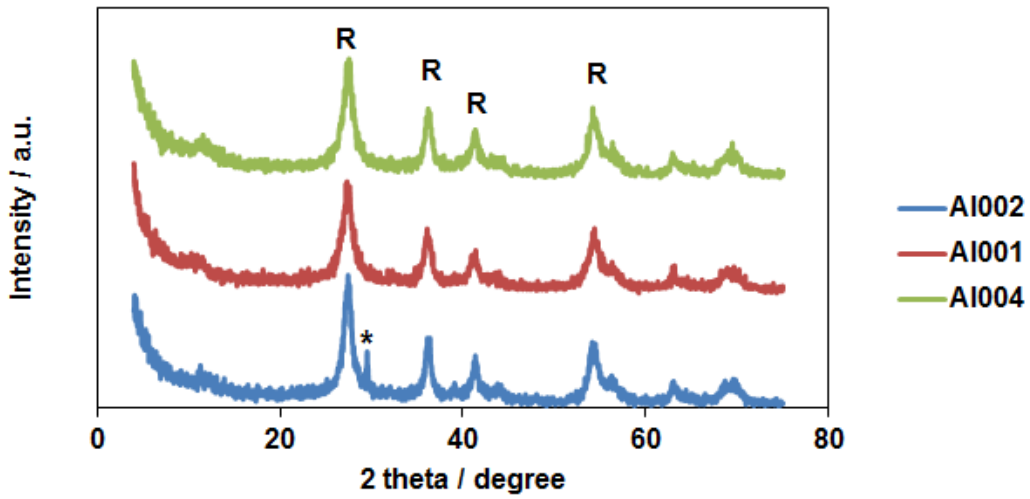

Figure 15. XRD pattern of the TiO_2/GO composite samples after drying at 85 °C R: characteristic for rutile-TiO_2 phase *: characteristic for $NaNO_3$ [163]

The amount of crystallized $NaNO_3$ in the composite dried at 85 °C was significant only in case of the unpurified GO (II) suspension (see AI002 in Figure 15). Furthermore, for samples prepared from GO (II) we also introduced a larger amount of NaOH during the delamination of the GO. In case of sample AI004 prepared from GO (II) an additional

washing step was inserted to remove the $NaNO_3$ (see Chapter 4.2.1 in Experimental part). This step was not used before by the research group [38]. As it can be seen in Figure 15, $NaNO_3$ was successfully removed by this washing procedure.

According to XRD results, samples AI001HT, AI002HT and AI004HT which were obtained from AI001, AI002, AI004 by HTT (Chapter 4.2.1 in Experimental part) contained only rutile phase TiO_2 (see Figure 16), the characteristic signal for $NaNO_3$ was absent.

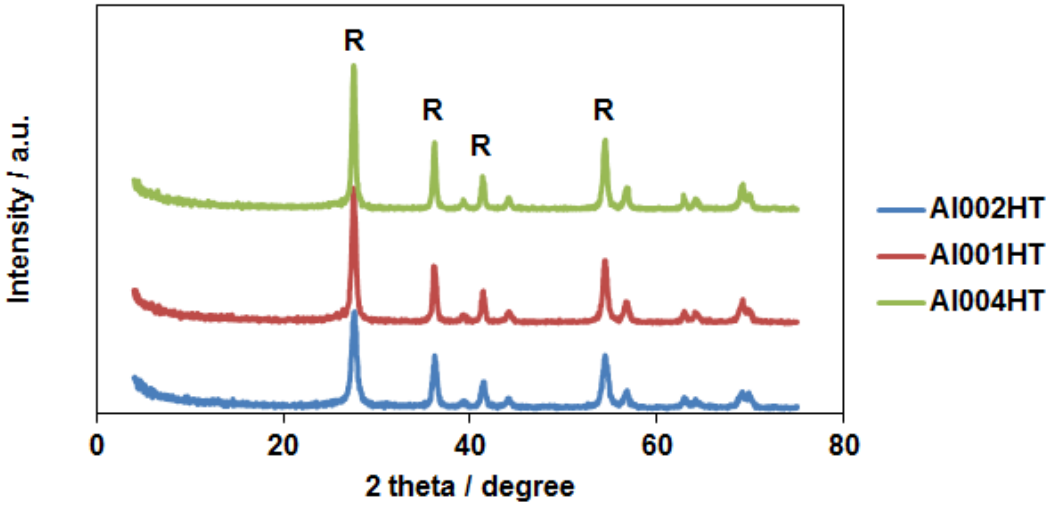

Figure 16. XRD pattern of the TiO_2/GO composite samples after high-temperature heat treatment in Ar (HTT, 600 °C, 8 h); R: characteristic for rutile-TiO_2 phase

Although the signal of $NaNO_3$ in XRD disappeared after the HTT needed for the incorporation of Mo into the TiO_2 lattice [38], the presence of $NaNO_3$ during HTT can be harmful, because it can be decomposed thermally above 450 °C with oxygen formation (equation 7) [164] leading to uncontrolled treatment conditions during the composite preparation. Oxygen might burn a part of the carbonaceous material. The decomposition of $NaNO_2$ under the further heating leads to Na_2O (equation 8), [165]. The presence of the Na compounds is supposed to be unfavourable for utilization as electrocatalyst supports.

(7) $2NaNO_3 \rightarrow 2NaNO_2 + O_2$

(8) $NaNO_2 \rightarrow Na_2O + NO + NO_2$

It is essential to mention that $NH_4(NO)_3$ which is also a compound possibly formed during the preparation of $Ti_{(1-x)}Mo_xO_2$ mixed oxide/carbon composites decomposes in another way (with formation of N_2O and H_2O) at elevated temperature [166].

The effect of the presence of $NaNO_3$ was also indicated by TG measurements. TG and DTG curves of samples AI001HT, AI002HT and AI004HT derived from GO and sample AI003HT derived from BP active carbon are presented in Figure 17. The most important features of the thermal behaviour of above samples are collected in Table 8. The remained material obtained after the heating the samples up to 900 °C in air was called the ash

content. The mass loss was related to the burning of the carbonaceous part. The ash content in each sample was slightly higher than 75 % which was expected from the nominal 75/25 ratio. The difference was the smallest in case of the BP derived sample. The ash content of the unwashed samples was 3-5 % higher than that of washed one (*cf.* AI001HT and AI002HT to AI004HT in Table 8). This difference could be attributed to the fact that some of the carbon material was really burned due to O_2 evolution from $NaNO_3$ during HTT step of the composite preparation and/or the Na-containing residue increased the ash content. Comparing the ash content of sample AI004HT and AI003HT only a slight difference can be found. Perhaps the real C/H/O ratio of the GO was slightly different from that we used for the calculations of the recipe and/or the samples may have contained O and H functional groups even after HTT.

The mass loss of these samples occurred in one step (see Figure 17). It is clearly visible from the data that the combustion of carbon material appeared at lower temperatures in case of GO than in case of BP (see $T_{DTG\ max}$ in Table 8).

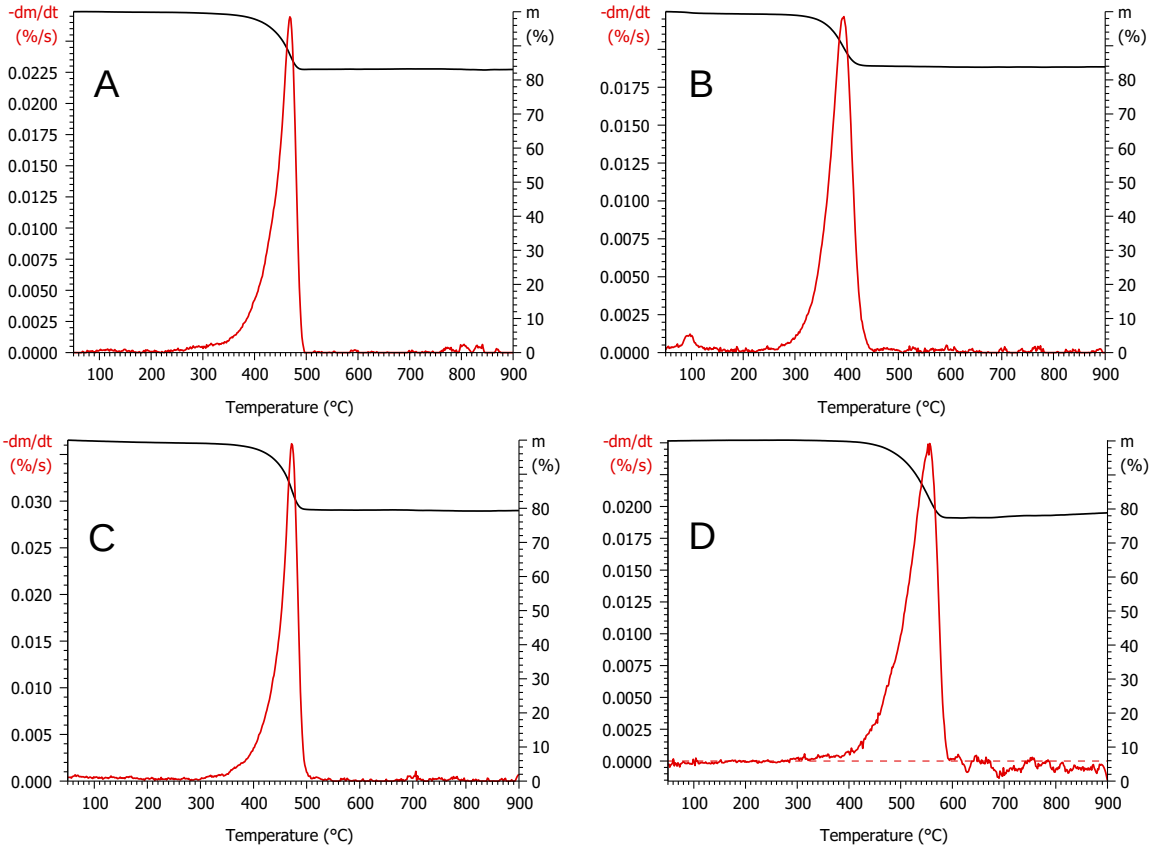

Figure 17. TG and DTG patterns of TiO_2/carbonaceous material composite type of samples. A: AI001HT (carbonaceous part derived from GO(I)), B: AI002HT (carbonaceous part derived from GO(II)), C: AI004HT (carbonaceous part derived from GO(II)), D: AI003HT (carbonaceous part derived from BP active carbon)

Furthermore, the presence of $NaNO_3$ shifted the maximum of DTG curve to lower value. This finding can be explained with the catalytic effect of Na^+ similarly to the observations described in the literature [167].

Table 8. Thermal features of TiO_2/carbonaceous material composite type of samples

Sample ID	Type of carbonaceous part	$NaNO_3$ removal	$T_{DTG\ max}$, °C	Ash content at 900°C, %	Carbonaceous part, %
AI001HT	GO (I) derived	-	465	82.92	17.08
AI002HT	GO (II) derived	-	400	83.71	16.29
AI004HT	GO (II) derived	+	475	79.21	20.79
AI003HT	BP derived	Nr	555	77.35	22.65

GO: graphite oxide, BP: Black Pearls (Cabot), nr: not relevant

Results of XPS study of sample AI002/HT and AI004/HT are shown in Table 9. Sodium appeared only in the AI002/HT sample which was obtained without nitric acid wash prior to HTT. According to the Na-related spectral features, sodium was present in oxide form on the surface after the HTT. Presence of Na-nitrate compounds could be ruled out as no nitrogen signal was observed in the AI002/HT sample. The surface carbon content of the unwashed sample was lower than that of the washed one while the surface oxygen content of the unwashed sample was a bit higher than that of the washed one. Appearance of carbonate was also observed only in the unwashed sample. These findings were consistent with the supposed burning effect of the $NaNO_3$ decomposition during the HTT.

In conclusion, it can be stated that $NaNO_3$ can be successfully removed with the washing step we introduced, thus replacing the long pre-purifying of GO, too.

Table 9. Results of XPS study of unwashed and washed composite supports

Sample ID	$NaNO_3$ removal by washing with HNO_3	Composition		Chemical state			Comment
		(in at%)	(in wt.%)	BE[a] assign. Ti 2p	BE[a] assign. O 1s	BE[a] assignment C 1s	
AI002/HT	no	Ti: 7.3 O: 30.3 C: 52.9 Na: 9.5	C: 37.0	458.7 TiO_2	530.0 metal oxide 531.4 -OH[b] 533.1 water[b]	284.4 graphitic C 285.9 C-O (8%) 288.1 C(O)-O (2%) 289.9 carbonate (4%)	Significant Na content. Na 1s BE: 1072.1 Na KLL KE[c]: 990.4 Na AP[d]: 2062.5 Assign.: Na_2O
AI004/HT	yes	Ti: 5.0 O: 16.3 C: 78.7 Na: --	C: 64.1	459.0 TiO_2	530.3 metal oxide 531.7 -OH[b] 533.3 water[b]	284.4 graphitic C 286.1 C-O (4%) 288.4 C(O)-O (1%)	No sodium was detected

[a]BE: binding energy (in eV)

[b]the O 1s component around 531 eV contains also contributions from epoxide groups on the carbon backbone and the peak around 533 eV contains also contributions from –OH and carboxylic groups bound to carbon

[c]KE: kinetic energy (in eV) for Auger lines

[d]AP: Auger parameter defined as the sum of a core level binding energy and an Auger transition kinetic energy for a given element

5.2 Changes of the carbonaceous part during the composite preparation

The pure GO is known to be thermally instable [136]; upon heating it turbostratic carbon is formed which lost the original layered structure of GO derived from graphite. The reason for this explosion-like change is the exothermic decomposition reactions of oxygen-containing groups of GO. Nevertheless, previous works of the research group with active carbon showed that high temperature heat treatment (HTT, 600 °C, 8 h, Ar atmosphere) is required for the formation of the mixed oxide phase of the composite, *i.e*. for the incorporation of Mo into the rutile TiO_2 lattice of the $Ti_{(1-x)}Mo_xO_2$/activated carbon composites [38]. However, we have not had information about the behavior of GO derived carbonaceous part during the HTT. It is also known from the literature that GO serves as binding site for Ti species during the hydrolysis of the Ti-precursor [139], but we have not been aware of how the close contact formed in this way between TiO_2 and GO in the composite influences on the thermal stability of the GO part.

In order to map out the changes in the carbonaceous phase during the preparation of the composite, we examined molybdenum-free samples to make the system easier to understand. Portions of sample AI001/II dried at 85 °C were treated in Ar at different temperatures (150 °C, 300 °C, 600 °C) for 8 h then characterized by Raman spectroscopy, ATR-IR spectroscopy and ^{13}C solid state NMR. Selected samples were studied by TEM, too.

Although there are a lot of report about Raman spectra of GO [168], we were not able to characterize our samples by this method. The reason why we were not able to get information about the carbonaceous part was a strong fluorescence during the laser irradiation (1064 nm excitation laser).

ATR-IR spectroscopy was a suitable method to characterize our samples (see Figure 18). Signals of oxygen-bearing groups (carbonyl vibration at 1711 cm^{-1}, carboxyl group vibrations at 1623, 1406, 1328 cm^{-1} and C-O-C and C-O-H stretching bands of ether and/or alcoholic groups around 1059 cm^{-1}) appeared in the spectrum of the untreated sample (line ***a*** in Figure 18). The band around 1623 cm^{-1} can be assigned to C=C bonds, too. This spectrum was very similar that was reported by Majrik et al. for 10 % GO/TiO_2 sample prepared by heterocoagulation method [155]. Upon heating the sample AI001/II at 150 °C in Ar the character of the spectrum did not change (line ***b*** in Figure 18). After the treatment of sample AI001/II at 300 °C the vibrational bands characteristic for carboxyl groups and/or C=C double bond (1623, 1406 and 1328 cm^{-1}) disappeared while a broad band attributed to surface carbonate/hydrocarbonate (1559 cm^{-1}) appeared indicating the significant changes of the sample (line ***c*** in Figure 18). Further increase in the temperature of the treatment resulted in a featureless spectrum due to the significant change in the structure of the carbonaceous part with the loss of the functional groups (line ***d*** in Figure 18). It has to be noted, however, that the background correction was problematic because this sample was too black.

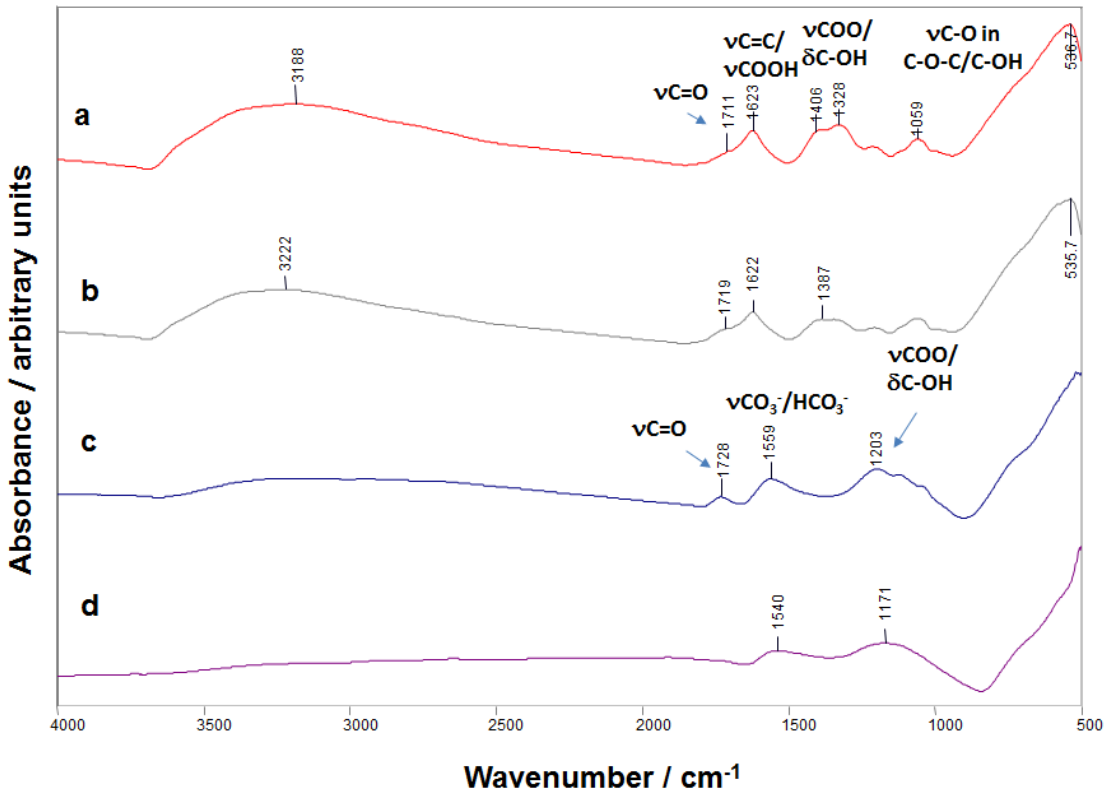

Figure 18. ATR-IR spectra of the AI001/II sample after treatment in Ar at different temperatures. ***a***: no heat treatment (only drying in air at 85 °C), ***b***: heat treatment at 150 °C, ***c***: heat treatment at 300 °C, ***d***: heat treatment at 600 °C

^{13}C solide state NMR spectra of TiO_2/GO derived samples can be seen in Figure 19. Line ***a*** in Figure 19A confirmed the ATR-IR results *i.e.* the untreated sample had several type of functional groups (carbonyl, C-OH, O-C-O) and sp^2 hybridized carbon. NMR results indicated the presence of certain aliphatic carbon, too. As a result of the heat treatment in Ar at 600 °C (line ***b*** in Figure 19A) the intensity of the signals decreased except of that of the phenolic OH and the sp^2 hybridized carbon which indicated again the removal of the functional groups under the HTT. However, we could not get information about a possible rupture of the GO sheets appeared under the HTT by means of these methods.

Use of hydrothermal/solvothermal treatment of suspension from GO and TiO_2 often has been described in order to obtain rGO/TiO_2 composite type of materials. Removal of the functional groups of and formation of Ti-C bond has also been suggested by hydrothermal treatment [146]. Based on the above knowledge, we hypothesized that an rGO-like carbon moiety obtained by solvothermal treatment below 150 °C would be more stable during HTT needed for the Mo incorporation. Most frequently, ethanol-water mixture was used for solvothermal treatment, but we decided to avoid the use of it in order to decrease the leaching of the added $(NH_4)_6Mo_7O_{24}$ during the real mixed oxide type composite preparation if our hypothetic method works. We choose pure 2-propanol which was also known as agent for catalytic transfer hydrogenations [169].

The sample used without solvothermal treatment, solvothermally treated sample and sample treated in Ar at 600 °C after the solvothermal treatment were characterized by ATR-IR spectroscopy (Figure 20). No well-defined bands related to functional groups can be detected in the IR spectrum of the sample after the solvothermal treatment at 140 °C (line ***b*** in Figure 20). The appearance of a sample obtained with HTT after solvothermal treatment differed from that without solvothermal treatment, it had a shiny, grayish black color. The background correction was not problematic but an almost "band-free spectrum" was obtained (line ***c*** in Figure 20).

Above results were consistent with the results of ^{13}C NMR measurements. By ^{13}C NMR 2-propanol was also detected (line ***d*** in Figure 19B). It has been known that due to its layered structure and oxygen containing functional groups GO strongly intercalates H_2O between its layers [170]. Obviously, during the solvothermal treatment the intercalated water more or less could be exchanged to 2-propanol. Probably, we observed its remanences after drying at 85 °C. Decreased intensity of the carbon containing functional groups (except of phenolic OH) after the solvothermal treatment was in line with the picture developed in the literature [146].

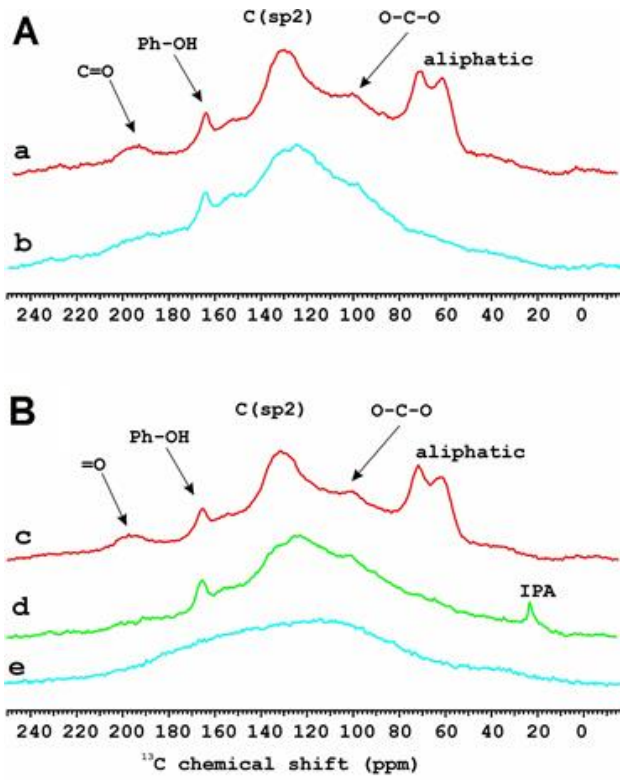

Figure 19. ^{13}C solide state NMR spectra of TiO_2/GO derived samples after treatments. A: samples from AI001/II, B: samples from AI001/III. IPA:2-propanol

a: no heat treatment (only drying in air at 85°C), ***b***:, heat treatment at 600°C, ***c***: no solvothermal treatment (ST), no heat treatment (only drying in air at 85°C), ***d***: ST, ***e***: ST followed by heat treatment at 600°C in Ar.

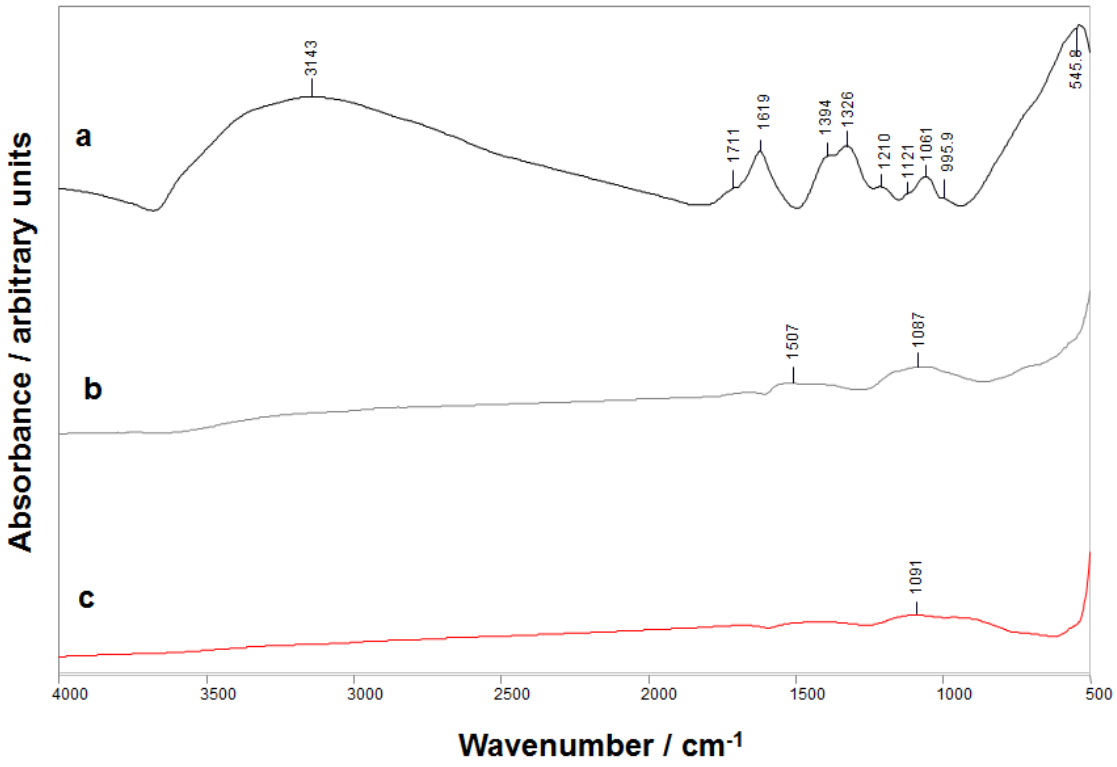

Figure 20. Effect of solvothermal treatment (ST) on the GO derived part of the AI001/III sample. ***a***: no ST, no heat treatment (only drying in air at 85 °C), ***b***: ST, ***c***: ST followed by heat treatment at 600 °C in Ar.

The most important observation was that the ^{13}C NMR spectra of the different samples treated at 600 °C were different (*cf.* line ***b*** and ***e*** in Figure 19). After HTT followed the solvothermal treatment the sample appeared to be completely graphitic in nature. Presence of this strongly graphitic carbon without functional groups let us to conclude that the structure of the carbonaceous part in the solvothermally treated sample was closer to the desirable rGO structure than that was in the non-solvothermally prepared one. Therefore, the composite material obtained from solvothermally treated samples was considered a promising electrocatalyst support.

Both ATR-IR and ^{13}C NMR measurements proved that the first stage of the composite production method resulted in a well-reproducible product regarding the carbonaceous part. AI001/II and AI001/III from parallel preparations resulted in very similar patterns by ATR-IR spectroscopy (*cf.* line ***a*** in Figure 18 and line ***a*** in Figure 20) as well as by ^{13}C NMR spectroscopy (*cf.* line ***a*** and ***c*** in Figure 19).

The pictures showed by ATR-IR and ^{13}C NMR spectroscopy for the same sample were slightly different which could be explained by the fact that in case of ATR techniques the penetration depth into the sample is typically between 0.5 and 2 μm while magic angle spinning (MAS) technique in solid state NMR spectroscopy provides information about the whole bulk phase.

The comparison of the TEM images samples obtained from the solvothermally treated and solvothermally untreated samples after HTT also clearly showed the differences in the formed carbon materials.

In case of sample AI001/II treated at 600 °C, composite particles containing both carbon and titania species as well as separated titania and carbon species were found with the same frequency. Separated particles might come either from the original sample or from the TEM sample preparation. It should be noted that for preparation of an appropriate sample for TEM the aqueous suspension had to be "shaken" with a lab-shaker at a relatively high speed for an hour in order to disperse evenly particles. The typical lowest resolution image of composite particles in the simply high temperature treated sample showed that micrometer size particles formed as a result of heat treatment; the metal oxide phases were not well visible (Figure 21 A). The "waviness" of the particles which were visible even under the middle darkest area was clearly corresponding to the presence of the reduced GO, and at greater magnification, this can be seen even better in the edges/around the edges (Figure 21 B). The magnified middle-top part of Figure 21 A has already characterized the nanostructure of the sample and made the two phases visible (Figure 21 B). TiO_2 appeared mainly in the form of elongated, stick-shaped particles. In addition, near the edges of the composite particle, the wrinkled (typical thermally degraded GO) carbon phase was well noticeable. Both the thermally degraded graphene oxide lamellae and the isometric particles (the lower part) can be seen in Figure 21 C.

In case of sample solvothermally treated before HTT (Figure 22), the morphology of the carbon phase differed significantly from that presented in Figure 21. The crystallinity of the carbon was improved, and the lamellae were less crumpled, and much more graphitic than without solvothermal treatment. However, much smaller amount of catalyst particles seemed to be remained on the carbon lamellae, which could be consistent with the fact that the polarity of the carbon phase had been severely reduced and it might have lost most of the charge carrier groups.

For more detailed analysis of the carbonaceous part it would be necessary to record the diffraction patterns using a well calibrated XRD apparatus and compare 002 reflections around 26 degrees in the future.

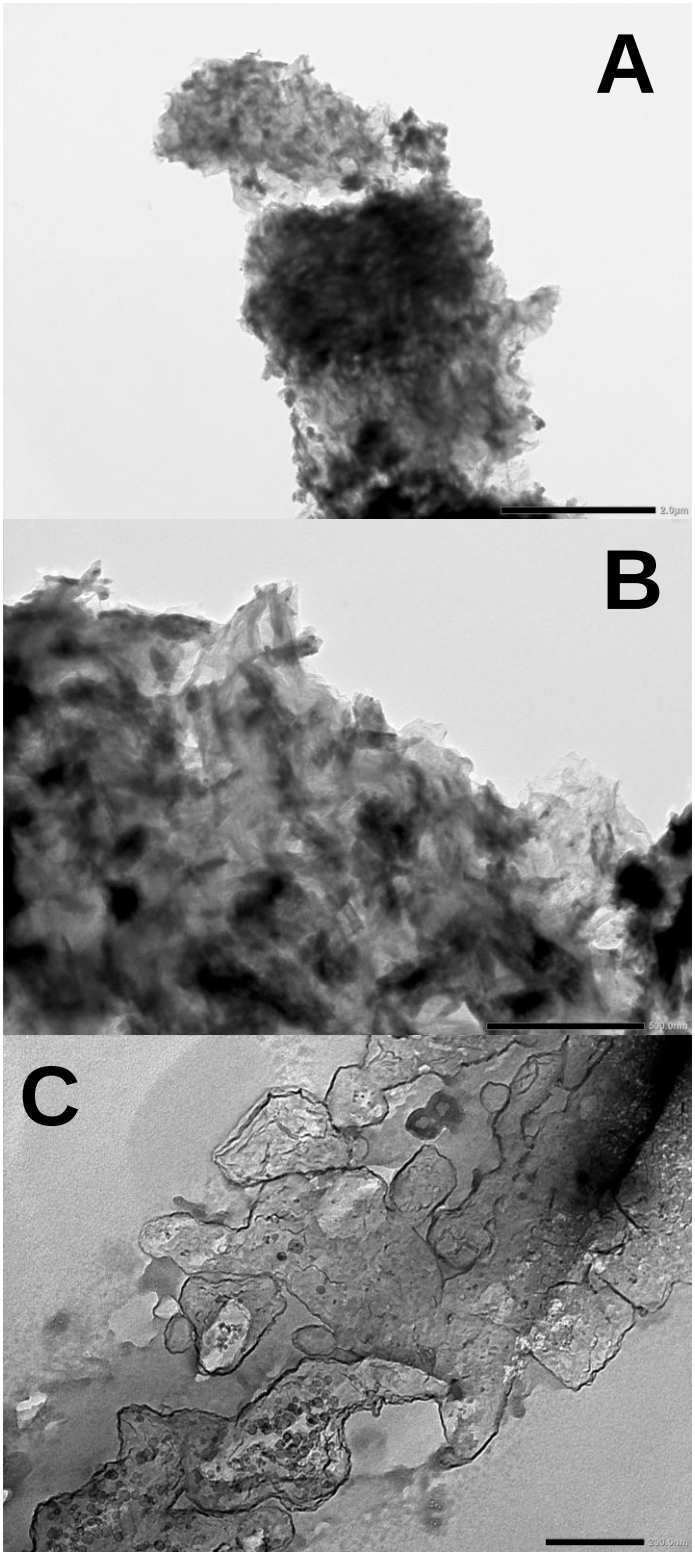

Figure 21. TEM images of sample obtained by only HTT from AI001/II.
Bar: A – 2 μm, B-500 nm, C: 200 nm

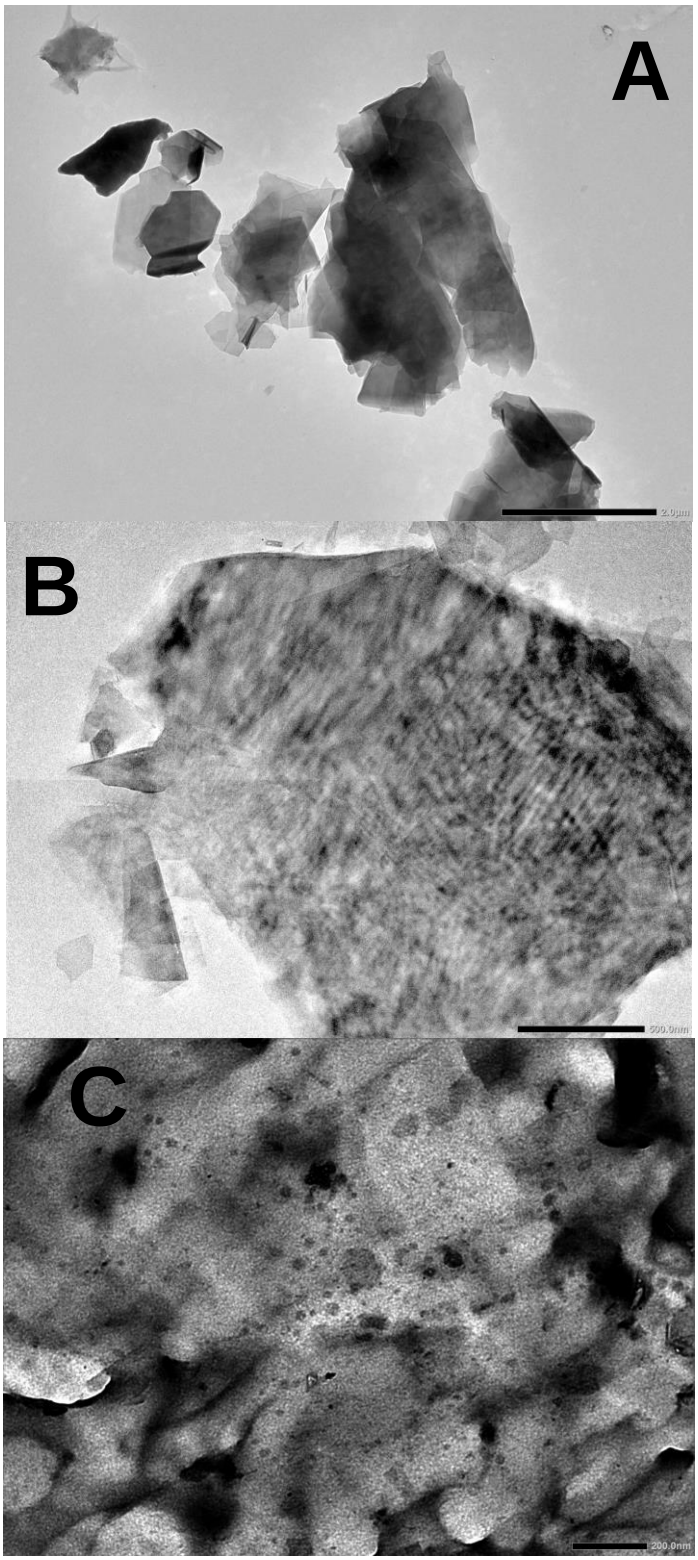

Figure 22. TEM images of sample obtained by HTT from solvothermally treated AI001/III.
Bar: A – 2 μm, B-500 nm, C: 200 nm

5.3 Formation of mixed oxide part during the composite preparation

It is known from the previous works of the research group [171] that Mo incorporation into rutile lattice of TiO_2 strongly depends on the Ti/Mo ratio. As 80/20 Ti/Mo ratio leads to almost completely incorporation of Mo, we choose above ratio in our preparation. Previous studies of the research group also reveal that the exclusive formation of the rutile phase TiO_2 nucleus on catalyst support before the high temperature treatment is prerequisite for the complete incorporation of the oxophilic metal into the rutile lattice [48, 68]. Therefore strong acidic media has been used during the hydrolysis and polycondensation reaction of Ti(O-*i*-Pr)$_4$ used as Ti precursor [171]. In order to adapt the composite preparation method for GO, we had to overcome the difficulty that strong acidic media is necessary for the formation of the rutile nuclei (consequently to Mo incorporation), in contrast the mild basic media is necessary for the delamination of GO. During the preparation we choose the strong acidic media (0.69 M HNO_3) to form rutile nucleus and we added the delaminated solution of GO (pH is adjusted to 9 with NaOH) suddenly to the reaction mixture by use of vigorous stirring. The original pH was then restored with cc. HNO_3. According to the XRD pattern of samples obtained after the drying step at 85 °C (see Figure 12 in Experimental) this procedure resulted in rutile nuclei beside the amorphous part (Figure 23).

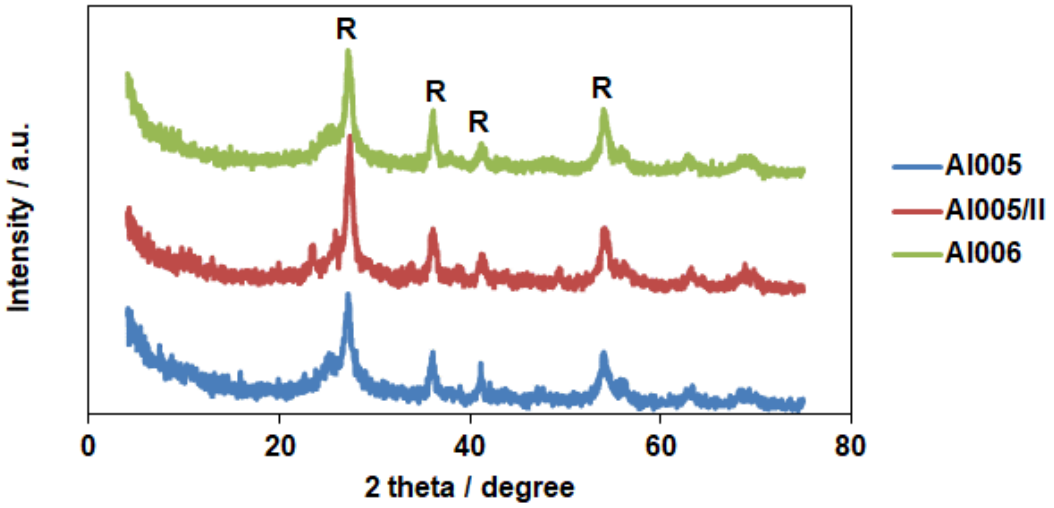

Figure 23. XRD pattern of samples obtained after the drying step at 85 °C. Ti/Mo: 80/20; R: characteristic for rutile-TiO_2 phase

Subjecting these samples to HTT, further crystallization occurred. XRD patterns of samples after HTT showed almost exclusive appearance of rutile phase which was a prerequisite of the Mo incorporation (Figure 24).

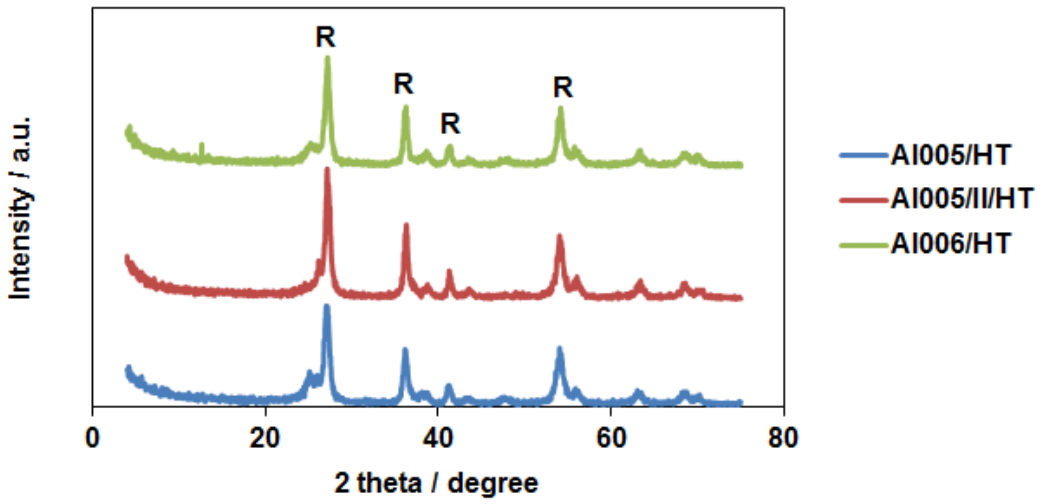

Figure 24. XRD pattern of samples obtained after HTT (600 °C, 8 h, Ar atmosphere). Ti/Mo: 80/20; R: characteristic for rutile-TiO_2 phase

As the effect of solvothermal treatment on the carbonaceous part of the composite was studied (Chapter 5.2), we also checked the effect of it on the crystalline phase. Figure 25 showed that rutile nucleus was kept after the solvothermal treatment.

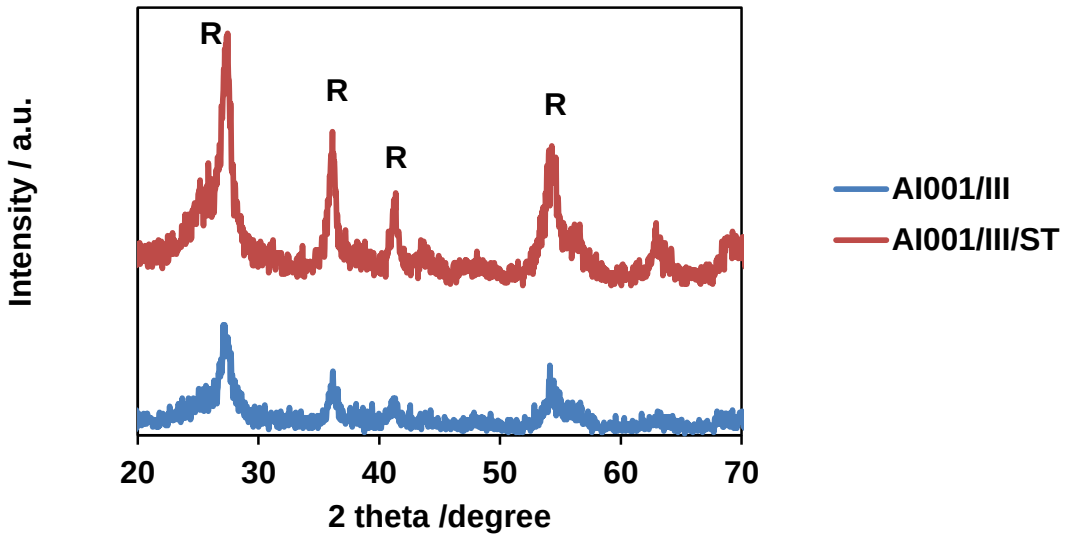

Figure 25. Effect of solvothermal treatment on composite treated at 85 °C. R: characteristic for rutile-TiO_2 phase

HTT of a solvothermally treated sample resulted in exclusive formation of rutil phase (Figure 26).

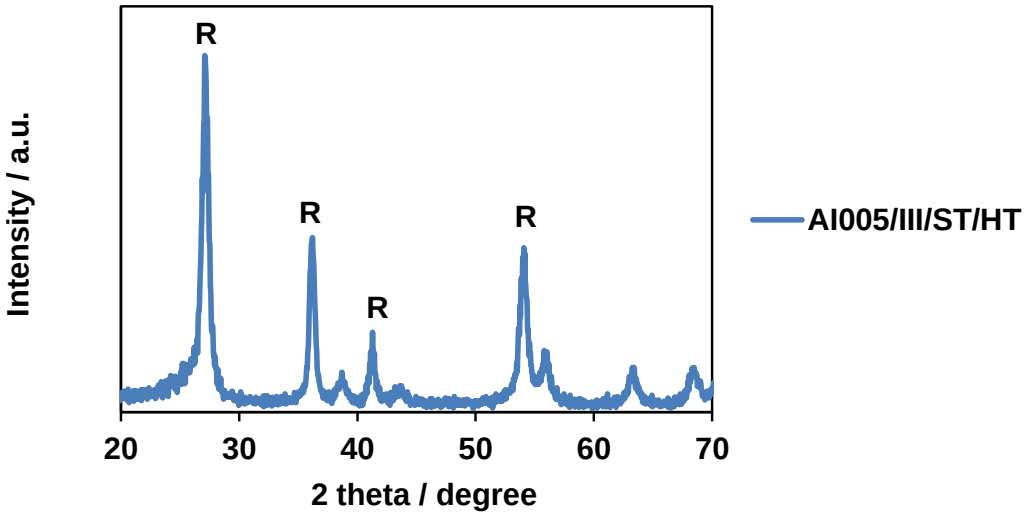

Figure 26. XRD pattern of a composit sample obtained by HTT (600 °C, 8 h, Ar atmosphere) after the solvothermal treatment. R: characteristic for rutile-TiO_2 phase

In conclusion, it can be stated that the preparation method previously developed for carbon-based composites can be adapted to GO. Furthermore, the solvothermal treatment does not influence the formation of crystalline phase of the composite.

5.4 Electrochemical behavior of selected samples

The selected electrocatalysts were the following:

AI003Cat (BP derived, Mo-free support, 20 wt.% Pt),
AI007Cat (BP derived, Mo-containing support, 20 wt.% Pt),
AI004Cat (GO derived, Mo-free support, 20 wt.% Pt),
AI005/IICat (GO derived, Mo-containing support, 20 wt.% Pt),
AI005/III/STCat (GO derived, Mo-containing, solvothermally treated support, 20 wt.% Pt).

For detailed description of sample preparation see chapter 4.2.1, Table 7, Figure 12. These samples were tested by cyclic voltammetry and CO_{ads}-stripping voltammetric measurements. Ar-purged CO_{ads}-stripping measurements were done before and after the 500-cycle stability test (for details see Experimental part).

Investigation of commercial 20 wt.% Pt/C electrocatalyst

Cyclic voltammetry and CO_{ads}-stripping voltammetry curves, obtained on the commercial 20 wt.% Pt/C (Quintech) electrocatalyst used as reference, are depicted in Figure 27. The Pt electrocatalyst had characteristic hydrogen adsorption/desorption peaks in the potential range between $0 < E < 400$ mV (Figure 27A). Hydrogen oxidation peaks were not seen on the CO_{ads}-stripping voltammogram (Figure 27B), suggesting that CO_{ads}-completely blocked the active Pt sites. Figure 27 demonstrates good reproducibility of the measurements obtained on the Pt/C catalyst. ESCA can be estimated from CO_{ads}-stripping voltammetry curves and from the charge of the hydrogen adsorption/desorption

according to according to equations 5 and 6, respectively. The values obtained from H desorption are collected in Table 10.

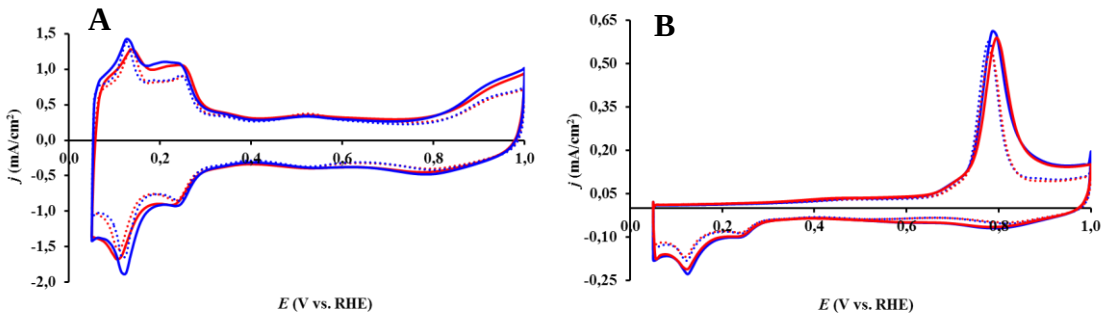

Figure 27. Cyclic voltammograms (A) and CO_{ads}-stripping voltammograms (B) of the 20 wt.% Pt/C (Quintech) electrocatalyst recorded in 0.5 M H_2SO_4 before (solid curves) and after 500 cycles (dotted curves) of the stability test. Sweep rate: 100 mV/s (A) and 10 mV/s (B). Reproducibility of the measurements was demonstrated by different colours.

Electrochemical behavior of the BP derived composite supported Pt catalysts

Stability and CO tolerance of a Mo-free 20 wt.% Pt/75 wt.% TiO_2 - 25 wt.% C and 20 wt.% Pt/75 wt.% $Ti_{0.8}Mo_{0.2}O_2$ - 25 wt.% C mixed oxide – carbon composite supported electrocatalysts were previously studied in details in the research group [38, 172]. Thus, these catalytic systems can be a good reference for evaluating the electrochemical behavior of new Pt electrocatalysts prepared by using GO derived $Ti_{0.8}Mo_{0.2}O_2$-C composite support materials. For this purpose, AI003Cat and AI007Cat catalysts were prepared and characterized by means of cyclic voltammetry and CO_{ads}-stripping voltammetry measurements.

The AI003Cat sample (Figure 28), which is a TiO_2-active carbon composite supported Pt catalyst, demonstrates a typical voltammogram characteristic for the reference Pt/C and to the Pt/TiO_2-C electrocatalysts, which resemble those commonly observed in the previous studies of the research group [172].

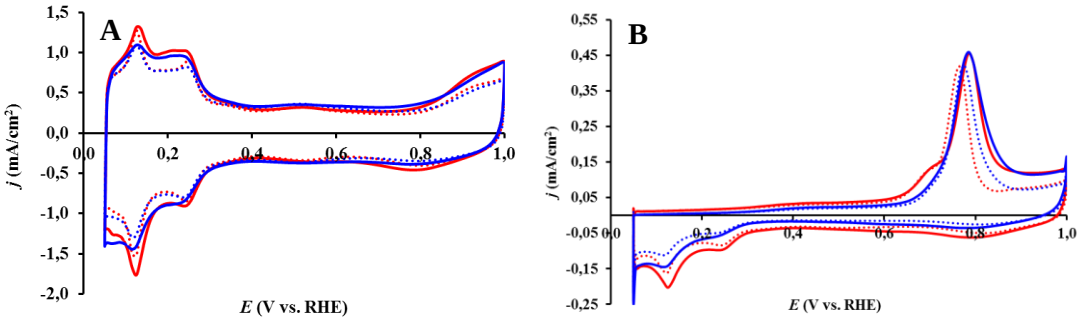

Figure 28. Cyclic voltammograms (A) and CO_{ads}-stripping voltammograms (B) of the **AI003Cat** electrocatalyst recorded in 0.5 M H_2SO_4 before (solid curves) and after 500 cycles (dotted curves) of the stability test. Sweep rate: 100 mV/s (A) and 10 mV/s (B). Reproducibility of the measurements was demonstrated by different colours.

The maximum of CO oxidation peak on the CO_{ads}-stripping voltammogram of the AI003Cat sample appeared at 785 mV, at a slightly less positive potential value than on that of the Pt/C. It is necessary to mention that besides the main CO_{ads}-stripping peak small shoulder at 705 mV was also observed on the AI003Cat catalyst. The shoulder at 705 mV could be attributed to oxidation of CO adsorbed on Pt-metal-oxide boundary sites [172].

Moreover, the presence of two electrooxidation peaks could also be attributed to inhomogeneous Pt particle size distribution according to literature analogies [76, 173]. Thus, in Refs. [76, 173] the presence of two overlapping peaks was ascribed to electrooxidation of the CO adsorbed on Pt nanoparticles with different structures (for example, due to the agglomeration of Pt nanoparticles and formation of nano-grained structures with high surface defect density).

The behaviour of the Mo-containing active carbon derived AI007Cat sample (Figure 29) was also similar to that found in previous works of the research group [68].

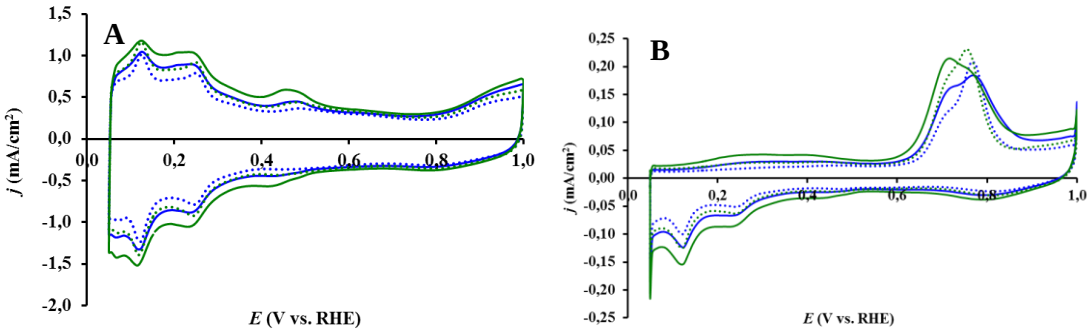

Figure 29. Cyclic voltammograms (A) and CO_{ads}-stripping voltammograms (B) of the **AI007Cat** electrocatalyst recorded in 0.5 M H_2SO_4 before (solid curves) and after 500 cycles (dotted curves) of the stability test. Sweep rate: 100 mV/s (A) and 10 mV/s (B). Reproducibility of the measurements was demonstrated by different colours.

Beside the hydrogen adsorption/desorption peaks characteristic for Pt, an oxidation-reduction peak pair can be observed on the cyclic voltammogram between 380 mV and 530 mV (Figure 29A), which is generally attributed to the oxidation and reduction of Mo species [38, 45].

As shown in Figure 29B during the first cycle after CO admission on the AI007Cat catalyst the electrooxidation of CO started at very low potential values (the onset of so-called 'pre-peak' is at ca. 50 mV). Regarding the CO_{ads}-stripping voltammograms a "pre-peak" consisting of two small overlapping peaks centred at ca. 215 and 400 mV which may be attributed to partial oxidation of weakly adsorbed CO and oxidation of Mo surface species, respectively [45]. It has been suggested that only CO adsorbed on specific Pt sites, where Pt and Mo atoms are in atomic closeness, can be oxidised below 400 mV potential [45]. The maximum of the main peak, which is related to the oxidation of the strongly bound CO on platinum, was shifted on the AI007Cat catalyst to less positive potential values comparing to the AI003Cat sample (*cf.* Figure 28B and Figure 29B). These observations demonstrated the increased CO tolerance of mixed oxide-activated

carbon composite supported Pt catalysts compared to the TiO_2-active carbon composite supported one [68].

Reproduction is very important in electrochemical measurements but parallel voltammograms recorded on active carbon derived composite supported samples were slightly different. I can presumably avoid these anomalies in the future with more experimental practice and electrochemical experience. Despite the differences, the main trends could be well observed.

Electrochemical behaviour of the GO derived composite supported catalysts

During the catalyst ink preparation by the conventional method used in the research group [171] the ink of GO derived samples was not homogeneous even visually, probably due to the different wetting properties of it compared to the BP derived samples. Consequently, a significant deviation was obtained for the shape of cyclic voltammograms and for the ECSA values calculated from parallel tests on the same sample. In order to overcome this problem, the prolongation of duration of the sonication seemed to be a solution. However, it has been described that 30 min sonication applied during the ink preparation most likely resulted in further exfoliation of the few layer thick graphene units of rGO containing carbon aerogels, increasing the actual surface area [162]. Therefore, I studied the time dependence of duration of the sonication of catalyst ink on the electrochemical behaviour of the AI004Cat sample. I prepared the ink and then I did tests by 30 min interval (the whole procedure including dropping, drying, and testing would take approximately 30 min). The voltammograms obtained after different time of the sonication reflect the surface changing of the catalysts during the cyclic polarization. The influence of the duration of the sonication on the shape of the cyclic voltammograms obtained on the AI004Cat was compared on Figure 30. It can be seen that the shape of the cyclic voltammograms characteristic of Pt catalysts was retained even after 4.5 hours of sonication (Figure 30). As shown in Figure 30 an increase of the duration of the sonication treatment results in an increase of the current density. The increasing tendency with increase of the duration of the sonication was also observed on the calculated ECSA values (Figure 31).

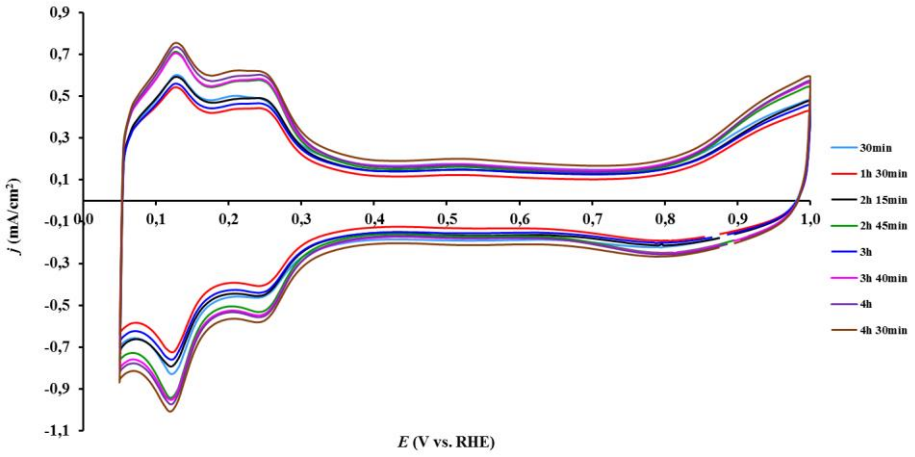

Figure 30. Influence of the duration of the sonication on the shape of the cyclic voltammograms obtained on the AI004Cat. Sweep rate: 100 mV/s

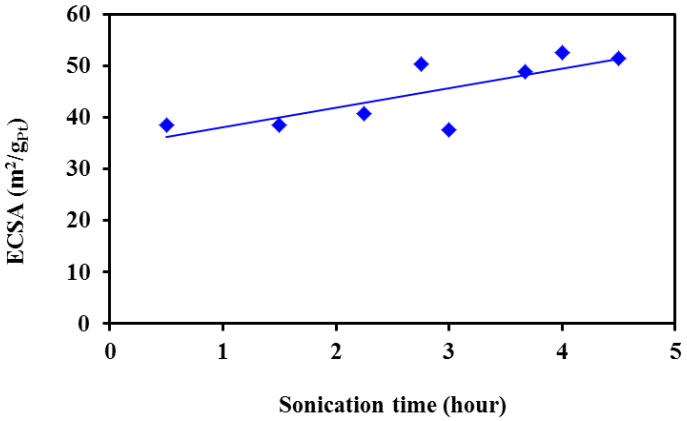

Figure 31. Influence of the duration of the sonication on the electrochemically active Pt surface area (ECSA) of the AI004Cat.

Taking into account the results presented on above two figures, 2.5 h of sonication was chosen for ink preparation of GO derived samples. The inhomogeneity of the catalyst over GC electrode after the drying of ink could also be observed (Figure 32) probably due to different adhesion forces compared to active carbon derived samples.

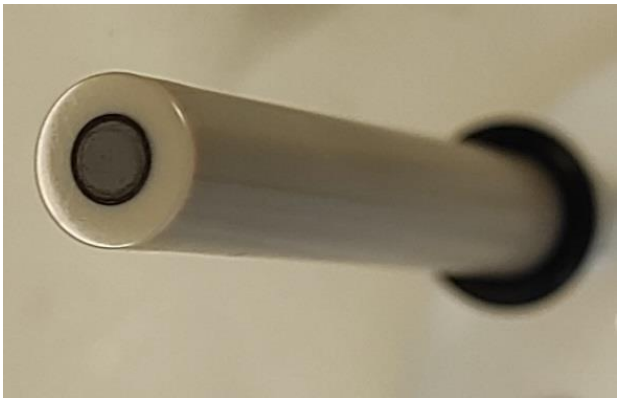

Figure 32. Photograph of inhomogeneous catalyst thin film obtained on a GC electrode after drying the catalyst ink in air. Catalyst: AI004Cat.

The deviation appeared during the measurements of time dependence (Figure 30, 31) can probably explained by varying inhomogeneity of the ink. Nevertheless, adequate reproducibility for GO derived molybdenum-free AI004Cat (see Figure 33) and molybdenum-containing AI005/IICat (see Figure 34) by use of elongated sonication time could be achieved both by cyclic voltammetry and CO_{ads}-stripping voltammetry measurements. It has to be mentioned that hydrothermally treated sample AI005/III/STCat did not show the problem of ink preparation.

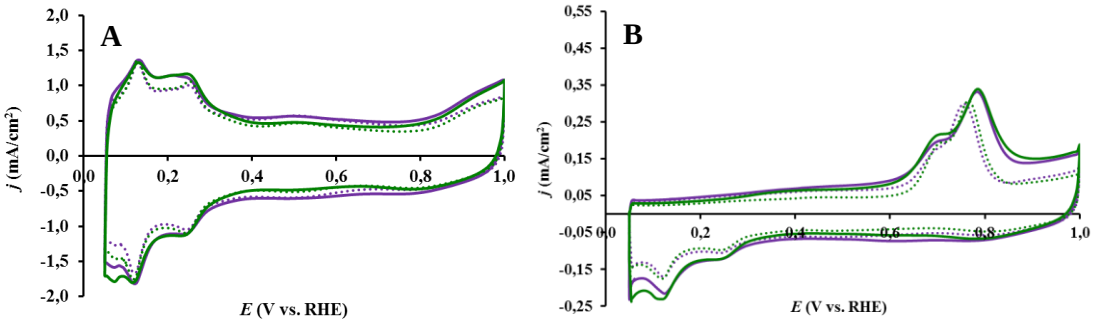

Figure 33. Cyclic voltammograms (A) and CO_{ads}-stripping voltammograms (B) of the **AI004Cat** electrocatalyst recorded in 0.5 M H_2SO_4 before (solid curves) and after 500 cycles (dotted curves) of the stability test. Sweep rate: 100 mV/s (A) and 10 mV/s (B). Reproducibility of the measurements was demonstrated by different colours.

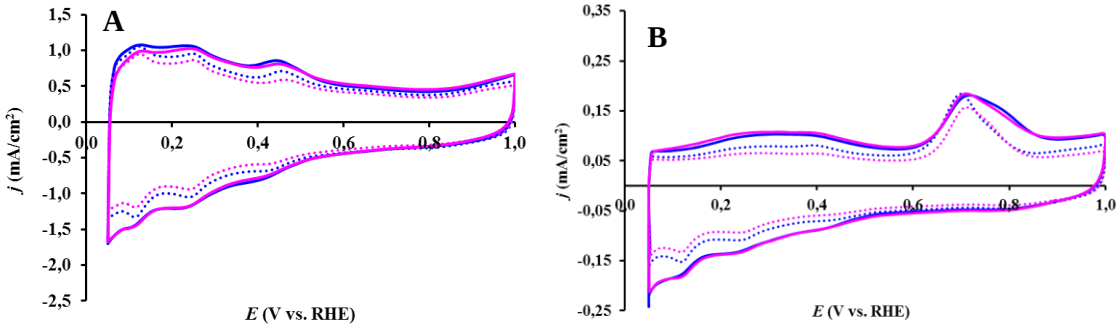

Figure 34. Cyclic voltammograms (A) and CO_{ads}-stripping voltammograms (B) of the **AI005/IICat** electrocatalyst recorded in 0.5 M H_2SO_4 before (solid curves) and after 500 cycles (dotted curves) of the stability test. Sweep rate: 100 mV/s (A) and 10 mV/s (B). Reproducibility of the measurements was demonstrated by different colours.

The character of cyclic voltammograms as well as CO_{ads}-stripping voltammograms of Mo-free electrocatalysts supported either on BP derived composite (AI003Cat) or GO derived one (AI004Cat) were quite similar; no significant difference in the shape of the main CO oxidation peak and the location of the maximum of this peak was observed on these catalysts (*cf.* Figure 28 and Figure 33), although in case of the AI004Cat sample the shoulder at 705 mV on the CO_{ads}-stripping voltammogram was more pronounced. We do not have sufficient information for a mechanistic interpretation of this growth at this moment.

In case of Mo-containing catalysts there was also a certain similarity in the CO_{ads}-stripping voltammograms of the BP-derived and the GO-derived samples (catalysts AI007Cat and AI005/IICat, respectively, *cf.* Figure 29B and Figure 34B). On these catalysts the main CO oxidation peak and shoulder were located at about 705-715 and 745-755 mV, respectively. As shown in Figures 29B and 34B the main difference observed on these catalysts was the intensity of the "pre-peak" area. It should be noted that "pre-peak" area observed on the GO-derived AI005/IICat catalyst was higher comparing to that one observed on the AI007Cat. All these observations indicate that both

Mo-containing catalysts have an enhanced CO tolerance compared to that of the reference 20 wt.% Pt/C (Quintech) catalyst.

Sample obtained by solvothermal treatment (Figure 35) showed very similar behaviour to that of the other Mo-containing ones. As shown in Figure 35B the CO electrooxidation (the so-called "pre-peak") started on the AI005/III/STCat sample at ca. 50 mV. Moreover, quite pronounced "pre-peak" area was characteristic for this catalyst. On the AI005/III/STCat sample the main CO_{ads}-stripping peak (oxidation of strongly bonded CO) was observed at ca. 725 mV (see Table 10 and Figure 35). Thus, enhanced CO tolerance of the Pt electrocatalyst prepared by solvothermal treatment was evidenced by the appearance of a CO-oxidation related "pre-peak" and by considerable shift of the maximum of the main CO oxidation peak towards less positive potential compared to the reference commercial Pt/C.

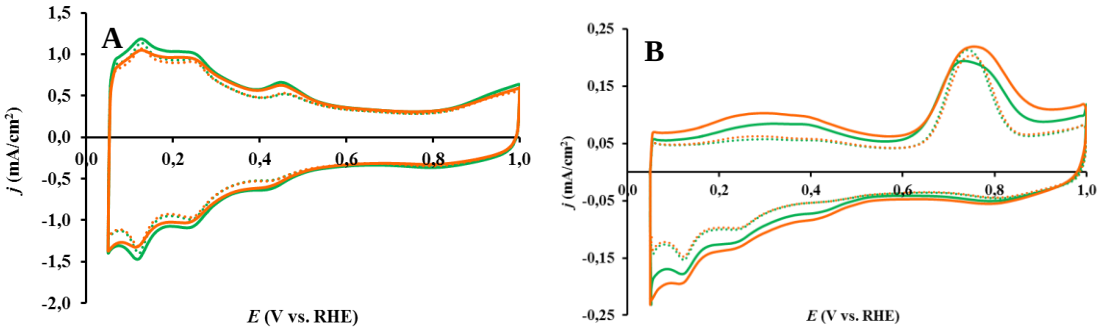

Figure 35. Cyclic voltammograms (A) and CO_{ads}-stripping voltammograms (B) of the **AI005/III/STCat** electrocatalyst recorded in 0.5 M H_2SO_4 before (solid curves) and after 500 cycles (dotted curves) of the stability test. Sweep rate: 100 mV/s (A) and 10 mV/s (B). Reproducibility of the measurements was demonstrated by different colours.

The position of the maximum of the main CO oxidation peak observed on the CO_{ads}-stripping curves for various composite supported Pt electrocatalysts are summarized in Table 10.

I also performed accelerated stability tests on each catalyst, which were 500-cycle cyclic voltammetric measurements in the potential range between 50 and 1000 mV with a polarization rate of 100 mV/s. Only relatively small changes of the voltammogram shape can be seen during the 500 cycles of the stability test. $ECSA_H$ values calculated from the amount of charge accompanying the electrooxidation of underpotentially deposited hydrogen, changes of ECSA values during the 500 cycle of the stability test (Δ ECSA**)** are also presented in Table 10.

Table 10. Electrochemical performance of the different composite supported Pt electrocatalysts

Sample ID	$E_{CO,max}$,[a] mV	$ECSA_H$, m^2/g_{Pt}	Δ ECSA, % [b]
Quintech (20% Pt/C)	~794	76.1	15.1
AI003Cat	785 (sh: 705)	76.9	14.2
AI007Cat	715 (sh: 755)	84.2	13.4
AI004Cat	785 (sh: 705)	78.6	9.7
AI005/IICat	705 (sh: 745)	77.6	8.4
AI005/III/STCat	~725	96.0	7.8

[a] The position of the main CO_{ads}-stripping peak measured on fresh catalysts.

[b] Δ ECSA= {1-($ECSA_{500}$/$ECSA_1$)}×100%; ***sh***= shoulder.

Despite the significantly smaller BET specific surface area of the GO-derived electrocatalyst supports (see Chapter 5.5) than those of the activated carbon derived ones, the $ECSA_H$ values were in the same range (Table 10). Further investigation of the electrochemical behaviour (HOR, ORR reactions) of the GO-derived samples goes beyond the scope of the present thesis, as does the further exploration of the relationships between electrochemical performance and detailed structural features (see Chapter 5.5).

The Δ ECSA values were slightly lower for the GO-derived catalysts than for the active carbon derived ones, which indicated certain benefits of the GO-derived composites as electrocatalyst support. In order to prove that GO-derived carbonaceous material in the composite type of support results in a more stable electrocatalyst further investigations, including long-term stability tests for 5,000 or even 10,000 cycles, are required. Because the TiO_2 $Ti_{(1-x)}Mo_xO_2$/C ratio of the composite-type supports prepared in this work was very high, there was little difference in the behaviours of the electrocatalysts made from them. Since the mixed oxide phase provides the increased stability and CO tolerance of the composite, while the carbon material provides the appropriate electrical conductivity of the support, it is necessary to optimize the mixed oxide / GO- derived carbon ratio in my next research.

In summary, preparation of active and stable Pt electrocatalysts using GO derived composite supports is feasible.

5.5 Detailed characterization of selected samples

The selected composite supports were the following: **AI003/HT** (BP derived, Mo-free), **AI004/HT** (GO derived, Mo-free), **AI005/II/HT** (GO derived, Mo-containing), **AI005/III/ST/HT** (GO derived, Mo-containing, solvothermally treated) and **AI007/HT** (BP derived, Mo-containing). For detailed description of sample preparation see chapter 4.2.1, Table 7, Figure 12.

Results obtained from BET measurements are summarized in Table 11. Isotherms can be found in Appendix. Both two the BP activated carbon derived composites showed isotherm type of II according to UPAC which is typical of non-porous or macroporous materials. The total pore volume was mainly given the by space between the aggregated

particles although a slight microporosity was also found. GO derived samples showed isotherm with hysteresis indicating the presence of mesopores. The hysteresis loop had typical H3 shape which may indicate the presence of aggregated flat particles or wedge-shaped pores. The H3 loop is also linked with the non-rigid nature of the adsorbent. If the hysteresis loop is type H3, the mesopore size distribution cannot be assessed reliably from either branch of the loop [174]. A minimal microporosity could be imagined, but it was not typical. The BET surface area of the BP derived composites significantly decreased compared to the parent activated carbon (1475 m^2g^{-1}) but still was large enough to use as support for electrocatalyst. GO derived composite samples also achieved the value of 100 m^2g^{-1} expected from electrocatalyst supports.

Table 11. Some characteristic features of selected samples

Sample ID	Pore volume, cm^3g^{-1}	BET surface area, m^2g^{-1}	$Ti_{11-x)}Mo_xO_2$/C from thermal analysis	T_I in DTG, °C	T_{II} in DTG, °C
AI003/HT	0.60	300	80/20[a] (77.4/22.6[b])	555	-
AI004/HT	0.69	264	80/20[a] (79.2/20.8[b])	475	-
AI005/II/HT	0.39	130	80/20[a]	440	745
AI005/III/ST/HT	0.53	120	80/20[a]	490	720
AI007/HT	0.51	238	80/20[a]	430	735

[a]estimated from the first step in the TGA curve, [b]from the ash content, T_I: temperature of the maximum of the DTG curve related to the oxidation of the carbon component, T_{II}: temperature of the second maximum of the DTG curve related to the Mo leave

In order to find the real ratio of (mixed) oxide and carbonaceous material, thermal analysis was carried out (ash content measurement by use of heating up in air). Mass (TGA) and mass loss rate (DTG) curves of the Mo-free selected samples are presented in Figure 17 C and D (AI003/HT, AI004/HT) while those of Mo-containing samples are presented in Figure A6-8 in the Appendix. In case of Mo-free samples DTG curves showed only one maximum in the range of 400-600 °C which can be related to burning of the carbonaceous part of the composite. In this case the ash content can be considered the oxide part while the [100-ash content] value can be considered the carbonaceous part of the composite. The values were not corrected with the amount of adsorbed water in the starting state of the samples and the ash content of the starting carbonaceous material was also neglected which may cause inaccuracy. However, in case of Mo-containing samples a second maximum of DTG curve appeared over 700 °C related to the sublimation of volatile MoO_3 which was present and/or was formed during the burning. The DTG curve took a negative value in the range of 470-620 °C which means an oxygen uptake. This observation supported the idea of oxidation of Mo. As the ratio of evaporated and residual Mo was unknown, the ash content did not give any information about the $Ti_{(1-x)}Mo_xO_2$/C ratio of the Mo-containing samples. We could estimate the carbon content only from the mass lost in the first step of the TGA curve. The estimated $Ti_{(1-x)}Mo_xO_2$/C values (80/20) were somewhat larger than the nominal one (75/25).

It could also be observed that temperature of the maximum of the DTG curve related to the oxidation of the carbon component (T_I in Table 10) was lower in the presence of

Mo than in the absence of Mo (*cf*. AI003/HT and AI007/HT for BP; *cf*. AI004 and AI005/II for GO), which could be explained the catalytic activity of Mo-oxides in oxidation reactions. However, the behavior of AI005/III/ST/HT did not fit into this trend. The reason of this exceptional behavior of AI005/III/ST/HT should be further investigated.

The XRD patterns of catalysts obtained from the selected composite supports by Pt load (20 wt.%) are presented in Figure 36.

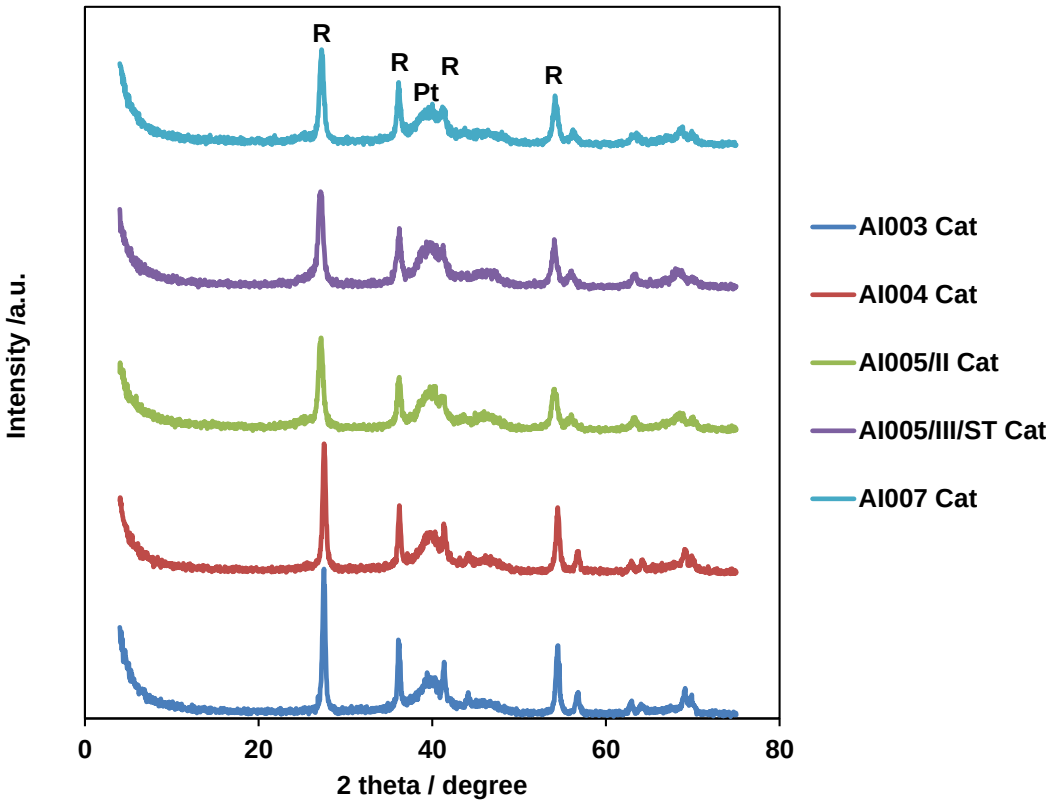

Figure 36. XRD patterns of catalysts obtained from the selected composite supports by 20 wt.% Pt load. R: characteristic for rutile-TiO_2 phase, Pt: characteristic for metallic Pt

All the selected samples contained TiO_2 or mixed oxides in rutile phase. In case of the Mo-free samples the sharp signal probably indicates a more crystalline oxide phase than that existed in the Mo-containing samples. Separated Mo-oxide phases did not appear. The broad band at 2 theta= 40 degree can be related to the presence of nanodispersed Pt metal. The presence of well dispersed, uniformly distributed Pt on the surface of the all selected catalysts was also evidenced by TEM images (Figure 37-40).

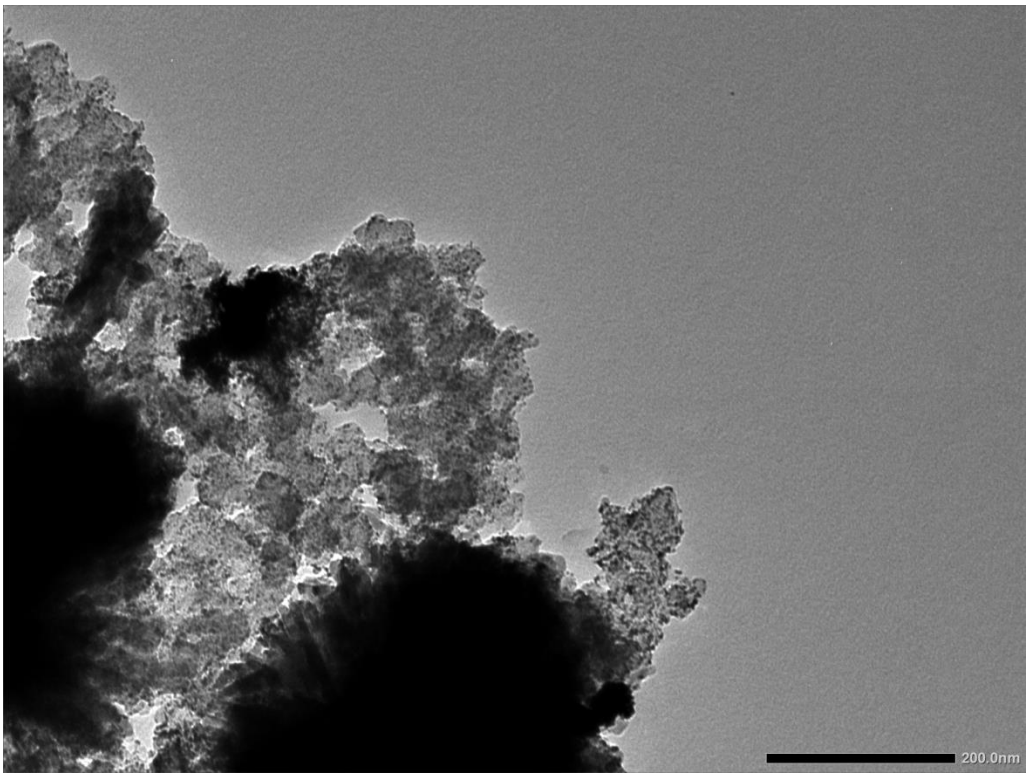

Figure 37. TEM image of AI003 Cat sample

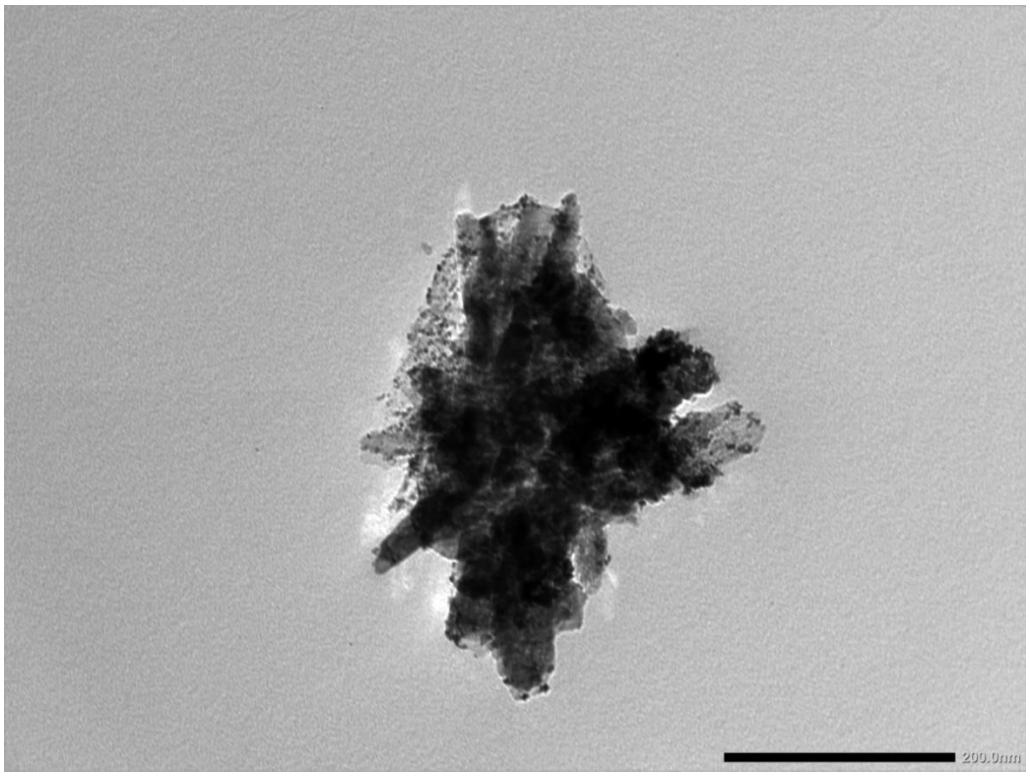

Figure 38. TEM image of AI005/II Cat sample

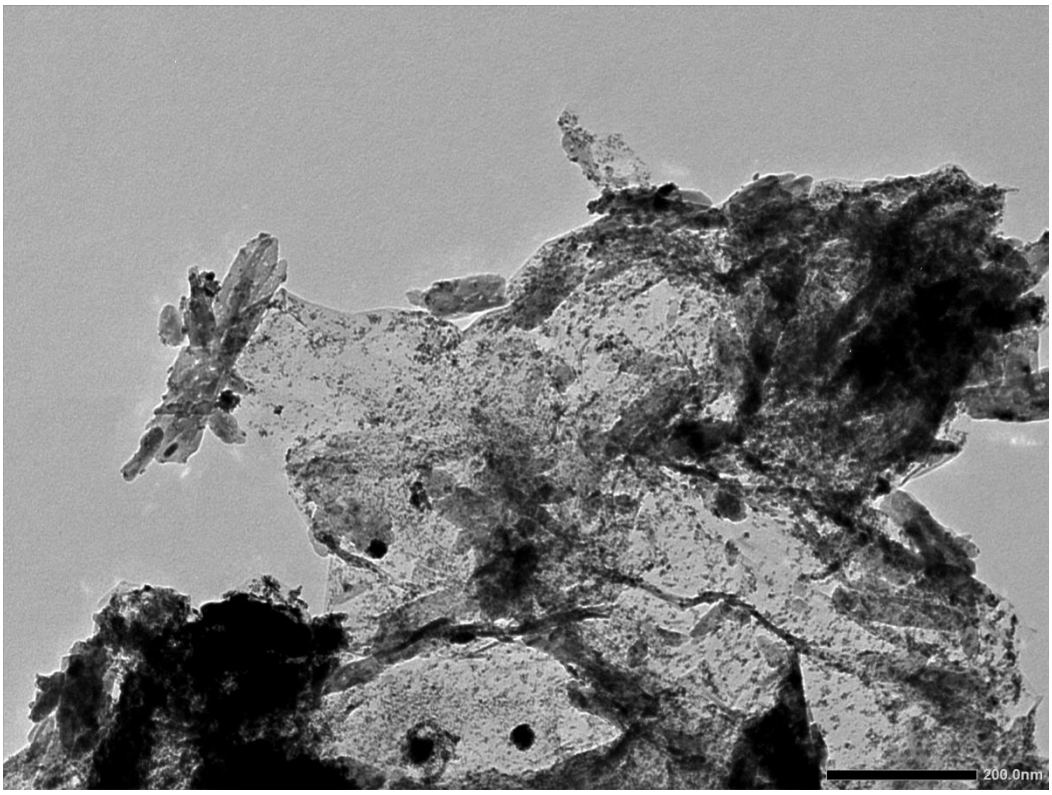

Figure 39. TEM image of AI005/III ST Cat sample

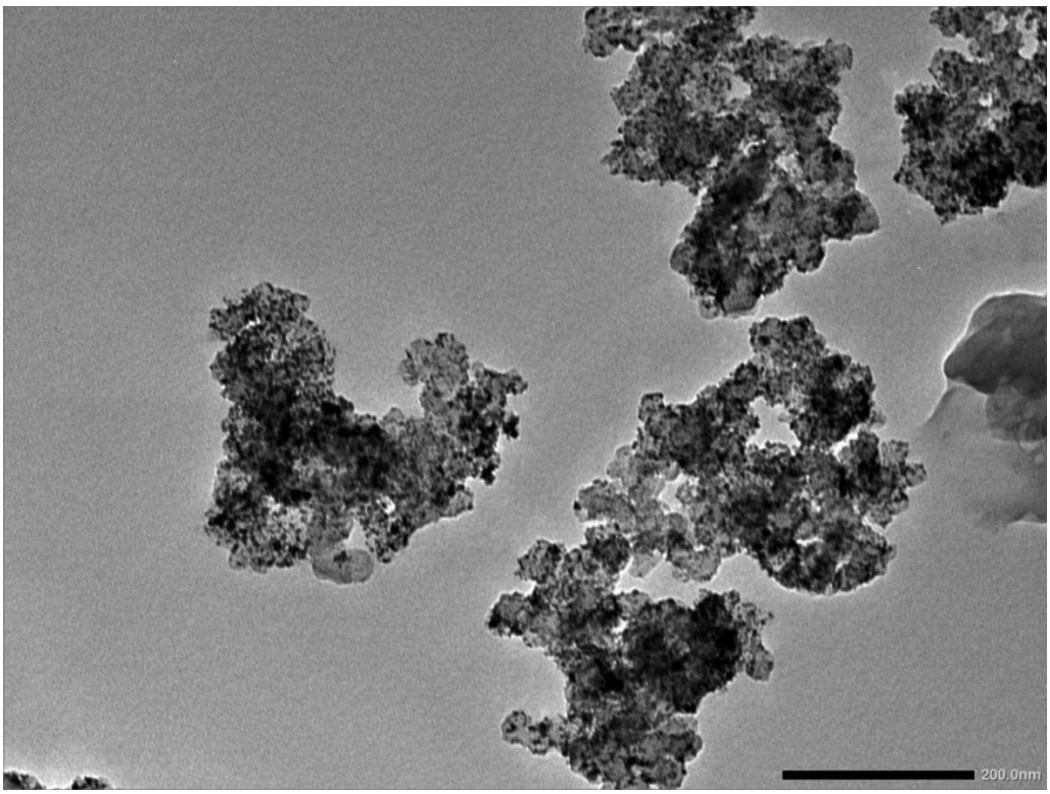

Figure 40. TEM image of AI007 Cat sample

The activated carbon derived Mo-free and Mo-containing catalyst samples showed very similar TEM images (*cf.* Figure 37 and 40) and were accordance those obtained in

previous works of the research group [38]. However, activated carbon-derived and GO-derived composite supported catalyst samples show somewhat different morphology (*cf.* Figure 37, 39, and Figure 38, 40). A creased GO derived film holds the rutile rods. Pt grains on could be seen on both rGO sheets and rutile crystals.

XPS results obtained on selected supports and catalysts are summarized in Table 12. As it is well documented in previous works [45] of the research group, the Mo 3d spectra of these composites are rather complex and contain contributions from several ionic states. In order to decompose these contributions, the measured Mo 3d spectrum was fitted with a combination of pre-defined features assigned to different chemical states of Mo. The Mo^{6+} ionic state was modeled by a spin-orbit doublet ($3d_{5/2}$ and $3d_{3/2}$ components) with line widths, intensity ratio and peak separation derived from the spectrum of a MoO_3 reference sample. The Mo $3d_{5/2}$ peak from the Mo^{6+} species arises around 232.5 eV [175]. For the Mo^{5+} ionic state the same spin-orbit doublet line shape was used with the $3d_{5/2}$ peak around 231 eV [175]. In case of Mo^{4+}, literature data and our own experience suggest a complex line shape consisting of two partially overlapping spin-orbit doublets with its lowest binding energy peak around or somewhat below 230 eV [175, 176], which arises as a result of two differently screened final states. Oxidation states lower than +4 were not observed for Mo in this study.

A single spin-orbit doublet was in all studied samples enough to model the Ti 2p spectra. The lowest binding energy contribution (Ti $2p_{3/2}$) was typically found around 458.8 eV, which indicated the exclusive presence of Ti^{4+} in the composite materials.

The C 1s spectrum had in all studied samples the characteristic asymmetric line shape of graphitic carbon. In addition, smaller contributions arising slightly above 286 eV indicating the presence of carbon atoms singly bound to oxygen (like in C-OH or in C-O-C in epoxide or lactone groups) and around 288.5 eV from more highly oxidized carbon species (carboxylic or anhydride functionalities) [177, 178] were also observed.

The O 1s spectrum in all cases consists of a strong leading peak slightly above 530 eV binding energy (arising from O ions bound to metal (Ti or Mo) cations), which is accompanied by a tail region towards high binding energies containing contributions from hydroxyl groups on the mixed oxide and C-O-C groups in epoxide from the carbon backbone (around 531 eV) and hydroxyl and carboxyl groups on the carbon backbone along with adsorbed water (around 533 eV) [177, 178].

Table 12 shows the main qualitative and quantitative results of the XPS measurements. A general observation was that XPS detected more carbon in all samples than the nominal 25 wt.% carbon content. It indicated that the structure deviates from the homogeneous mixture of the components assumed during the quantitative evaluation process. Indeed, the surface specific XPS technique tends to underestimate the mixed oxide content if a certain fraction is present in the form of crystallites thicker than the information depth of the method (around 10 nm). According to previous results of the research group, an apparent carbon content around 40 wt.% is typical for mixed oxide composites with a 75/25 nominal oxide/carbon weight ratio [38]. In these samples a few larger mixed oxide crystallites coexisted with more dispersed mixed oxide species on the

carbon, while the catalytic behavior of the Pt electrocatalysts prepared on these supports is still determined by the Pt-mixed oxide interactions [38].

As it turns out from the Table 12, in this series of samples a carbon content around or somewhat above 40 wt.% was typically found. The exceptions are the AI004/HT and AI003/HT composites, which contain only TiO_2 in the oxide component. In these samples the carbon content is around 60 wt.%, which suggests that the oxide forms large crystallites with relatively low coverage on the carbon backbone, regardless to the source of the carbon. The somewhat increased Ti $2p_{3/2}$ binding energy (459 eV) indicates that the electronic coupling of these TiO_2 crystallites to the carbon backbone is different (probably weaker) than in the case of the other samples with more dispersed mixed oxide content.

The carbon content itself is predominantly graphitic, regardless if it was reduced from graphite oxide during the sample preparation or it was originally an active carbon material. However, the results in the Table indicate that while the BP-derived samples and the solvothermally prepared AI005/III/ST/HT composite contain relatively small amount of carbon atoms bound to oxygen, the other GO-derived samples remain somewhat more oxidized.

Another general feature of the Mo-containing composites is that the Mo content deduced from the XPS measurements is somewhat higher than the nominal value. It indicates that Mo tends to be a surface species [38, 179]. In particular, the Mo/Ti ratio of the AI005/II/HT composite is unusually high, which suggests some Mo segregation in the support material. Disappearance of the excess Mo during Pt loading is a known feature of the mixed oxide-carbon composites [179], which is illustrated by the large decrease of the Mo/Ti ratio between the AI005/II/HT support and the AI005/II Cat catalyst. The solvothermally treated AI005/III/ST/HT support was very interesting in this sense, as the Mo/Ti ratio is very close to the nominal value even before Pt deposition.

As far as the chemical states of Mo are concerned, the AI007 Cat sample reproduces well the typical behavior of the Ti-Mo-mixed oxide-carbon composite supported electrocatalysts [38, 179]. Accordingly, Mo in these samples is relatively strongly oxidized; the dominant chemical state is Mo^{6+}, which is accompanied by smaller amounts of Mo^{5+} and Mo^{4+}. It is probably the result of air exposure after synthesis, during which Mo species at or near the surface of the mixed oxide particles are re-oxidized to the highest possible oxidation state, while species more inside of the mixed oxide particles are somewhat protected from this oxidation effect. Data suggest that the Mo content of the AI005 composites is more reduced, especially after the solvothermal treatment, which results in an unusually high Mo^{4+} contribution.

The Pt content well above the nominal value indicates that Pt is a well-dispersed surface species in the Pt-loaded catalysts. XPS data suggest only marginal oxidation of the Pt.

Table 12. Results of XPS measurements of selected support and catalyst samples

Sample ID	Composition		Chemical state				
	(in at%)	(in wt.%) and Mo:Ti ratio[a]	BE[b] ratio Mo 3d	BE[b] assign. Ti 2p	BE[b] assign. O 1s	BE[b] assignment C 1s	BE[b] ratio Pt 4f
AI003/HT	Mo: -- Ti: 7.0 O: 19.8 C: 73.2 Pt: --	C: 57.4	--	459.1 TiO_2	530.4 metal oxide 531.9 -OH[c] 533.1 water[c]	284.4 graphitic C 286.0 C-O (3%) 288.9 C(O)-O (1%)	--
AI004/HT	Mo: -- Ti: 5.0 O: 16.3 C: 78.7 Pt: --	C: 64.1	--	459.0 TiO_2	530.3 metal oxide 531.7 -OH[c] 533.3 water[c]	284.4 graphitic C 286.1 C-O (4%) 288.4 C(O)-O (1%)	--
AI005/II/HT	Mo: 4.0 Ti: 6.4 O: 27.5 C: 62.1 Pt: --	C: 39.9 Mo:Ti: 49:80	Mo^{4+}: 229.6 (19%) Mo^{5+}: 231.0 (20%) Mo^{6+}: 232.3 (61%)	458.6 TiO_2	530.0 metal oxide 531.4 -OH[c] 533.3 water[c]	284.4 graphitic C 286.1 C-O (5%) 288.2 C(O)-O (1%)	--
AI005/II Cat	Mo: 2.2 Ti: 5.4 O: 26.2 C: 60.9 Pt: 5.3	C: 45.2[f] Pt: 39.1 Mo:Ti: 33:80	Mo^{4+}: 230.0 (16%) Mo^{5+}: 231.1 (17%) Mo^{6+}: 232.4 (67%)	458.6 TiO_2	530.1 metal oxide 531.6 -OH[c] 533.3 water[c]	284.4 graphitic C 286.1 C-O (6%) 288.3 C(O)-O (3%)	71.2 Pt^0 72.5 Pt^{2+}: PtO, $Pt(OH)_2$ (9%) 75.0 Pt^{4+}: PtO_2 (4%)
AI005/III/ST/HT	Mo: 1.7 Ti: 5.7 O: 24.8 C: 66.3 Pt: --	C: 47.7 Mo:Ti: 24:80	Mo^{4+}: 229.7 (30%) Mo^{5+}: 231.0 (22%) Mo^{6+}: 232.4 (48%)	458.7 TiO_2	530.0 metal oxide 531.3 -OH[c] 533.4 water[c]	284.4 graphitic C 286.1 C-O (3%) 288.7 C(O)-O (1%)	--
AI007 Cat	Mo: 1.8 Ti: 5.7 O: 27.0 C: 59.4 Pt: 6.1	C: 44.7[d] Pt: 43.1 Mo:Ti: 26:80	Mo^{4+}: 230.0 (9%) Mo^{5+}: 231.2 (19%) Mo^{6+}: 232.6 (72%)	458.7 TiO_2	530.1 metal oxide 531.5 -OH[c] 532.8 water[c]	284.4 graphitic C 288.4 C(O)-O (3%)	71.3 Pt^0 72.6 Pt^{2+}: PtO, $Pt(OH)_2$ (5%) 75.1 Pt^{4+}: PtO_2 (2%)

[a] nominal Mo:Ti ratio: 20:80; [b] BE: binding energy (in eV); [c]the O 1s component around 531 eV contains also contributions from epoxide groups on the carbon backbone and the peak around 533 eV contains also contributions from –OH and carboxylic groups bound to carbon; [d]calculated for the support material only, not involving Pt

6. Summary

The previously developed methods for the preparation of the $Ti_{(1-x)}Mo_xO_2$/active carbon composite type of electrocatalyst support were adapted to the use of GO. The following difficulties had to be overcome:

(1) Strong acidic media adjusted by HNO_3 was necessary for the formation of the rutile nuclei (which are needed for good Mo incorporation); while media of much higher pHs (added NaOH) is necessary for the delamination of GO. It was proved by XRD measurements that addition of 5 hours aged solution of Ti(O-*i*-Pr)$_4$ to delaminated GO under vigorous stirring resulted in exclusively rutile phase of mixed oxide after HTT.

(2) The $NaNO_3$ crystallized by use of the delaminated GO in the conventional preparation method of the research team. Under HTT needed to incorporate Mo into the rutile-TiO_2 phase $NaNO_3$ decomposed leading to uncontrolled treatment conditions. Therefore, before addition of the Mo precursor, the liquid phase in the slurry had to be changed and the solid part had to be washed. XRD and XPS measurements proved that using this procedure $NaNO_3$ could be removed. The presence of Na^+ decreased the maximum of DTG curve of the composite through its likely catalytic effect on burning of the carbonaceous part.

(3) As GO plates may be fractured during HTT, it was thought that this effect could be reduced by solvothermal treatment. Therefore, a new step, *i.e.* a solvothermal treatment in *i*-PrOH was added to the procedure prior to HTT. ^{13}C NMR, TEM and XPS measurements proved that the carbon structure of solvothermally treated sample differed significantly from that of samples without solvothermal treatment. Meanwhile, the rutile structure of the mixed oxide was retained. BET specific surface areas of these GO derived composites were in the range 100-300 m^2/g, which corresponded to the requirements for electrocatalyst carriers. The presence of aggregated flat particles indicated by the H3 shape of hysteresis loop were consistent with the expected structure of the composite which is built from plate structures of the parent delaminated GO.

The catalyst ink developed for the electrochemical study of carbon-based composite electrocatalysts did not give well-reproducible results for GO-derived composite supported catalysts except of the solvothermally treated one. For successful electrochemical testing of these electrocatalysts the duration of ultrasonic treatment had to be optimized.

The beneficial effect of the Mo on the CO tolerance of the $Ti_{(1-x)}Mo_xO_2$-carbonaceous material composite supported Pt electrocatalyst were observed in case of GO derived carbonaceous material, too. The Δ ECSA values were slightly lower for the GO-derived catalysts than for the active carbon derived ones which may indicate the enhanced stability of the GO-derived composite supported Pt catalyst. In order to prove that GO-derived carbonaceous material results in more stable electrocatalysts further investigations, including long-term stability tests are required. Since the TiO_2/C and $Ti_{(1-x)}Mo_xO_2$/C ratio of the composite-type supports prepared in this work was very high there was little difference in the behaviour of the electrocatalysts made from them, consequently it is necessary to optimize the mixed oxide / GO- derived carbon ratio. I consider these studies to be a necessary continuation of my work.

Acknowledgements

I would like to thank my supervisor Dr. *András Tompos* for his inspiring thoughts while guiding my work for the Master Thesis. I am grateful to Prof. Dr. *Krisztina László* for helping me with her remarks and suggestions as an internal supervisor. My deepest gratitude is to my consultant *Emília Tálas* for her constructive guidance and valuable advices in the experimental work and in the evaluation of my results. Special thanks to Dr. *Tamás Szabó* for providing me graphite oxide and for TEM measurements. I am thankful to my colleagues in the Natural Sciences Research Centre for their measurements in catalyst characterization and for their help in the evaluation of results (*Attila Domján* - ^{13}C NMR, *Szilvia Klébert* - BET measurements, *Judith Mihály* -ATR-IR, *Zoltán Sebestyén* - thermal analysis, *Zoltán Pászti* - XPS). Very special thanks to *Irina Borbáth* for her help in the evaluation of electrochemical results, to *Gábor Szijjártó, Ádám Vass,* and *Ildikó Turi* for their technical assistance in the catalyst preparation and in the electrochemical measurement.

The financial supports by the following projects are greatly acknowledged.

VEKOP-2.3.2-16-2017-00013. "The excellence of strategic R & D workshops, Material science excellence workshop: development of environmentally friendly processes for efficient use of renewable energy and raw materials and for controlled release of their energy content".

Project no. 2017-2.3.7-TÉT-IN-2017-00049 has been implemented with the support provided from the National Research, Development, and Innovation Fund of Hungary, financed under the TÉT-IN-2017 funding scheme.

Project no. NNE130004 has been implemented with the support provided from the National Research, Development and Innovation Fund of Hungary, financed under the TR-NN-17 funding scheme.

This work was performed within the framework of the "Holistic design of fuel cell electrocatalysts for the least power applications" (CATALEAST) M-ERA.NET project. Project No. NNE 131270 has been implemented with the support provided from the National Research, Development and Innovation Fund of Hungary financed under the M-ERA.NET funding scheme.

APPENDIX

Experimental

ATR-IR spectra were recorded by the means of a Varian 2000 (Scimitar Series) FT-IR spectrometer (Varian Inc, US) equipped with an MCT (Mercury-Cadmium-Telluride) detector and with a 'Golden Gate' diamond single reflection ATR unit (Specac Ltd, UK). 64 scans were collected at a spectral resolution of 4 cm^{-1}. Baseline correction was performed using the GRAMS/AI (7.02) software (ThermoGalactic Inc., US).

Raman spectra were recorded with a dynamically aligned Bio-Rad (Digilab) dedicated FT-Raman spectrometer equipped with a Spectra-Physics Nd-YAG-laser (1064 nm) and high sensitivity liquid-N_2 cooled Ge detector. The laser power used was about 250 mW at the samples. The resolution of the Raman instrument was ca. 4 cm^{-1} and a backscattered geometry was used. For each spectrum 256 individual spectra were averaged.

Solid state NMR magic angle spinning (MAS) spectra of the fresh and recovered samples were recorded on a Varian NMR System (Varian Inc., Palo Alto, CA, U.S.A.) operating at ^{1}H frequency of 400 MHz with a Chemagnetics T3 4.0 mm narrow bore double resonance probe. The ^{1}H MAS spectra were measured with a rotor spinning rate of 12 kHz. The ^{1}H $\pi/2$ pulse was 3 μs and a repetition delay of 30 seconds was used. For the ^{13}C CP MAS (cross-polarization magic angle spinning) [180] spectra 20000 transients were recorded with 2 ms of contact time with SPINAL-64 decoupling [181] and 5 seconds of recycle delay. The direct polarization ^{13}C MAS spectra were recorded with 60 s of relaxation delay and 20000 transients were collected. For the ^{13}C spectra adamantane was used as external chemical shift reference (38.55 and 29.50 ppm), $\pi/2$ pulse lengths were 3.0 μs for carbon and 3.0 μs for the proton channel. For the ^{13}C measurements a rotor spinning rate of 8 kHz were used. The measuring temperature was 20°C in all cases.

X-ray photoelectron spectroscopy (XPS) measurements were performed using an electron spectrometer manufactured by OMICRON Nanotechnology GmbH (Germany). The photoelectrons were excited by MgKα (1253.6 eV) radiation. Spectra were recorded in the Constant Analyser Energy mode of the EA125 energy analyser with 30 eV pass energy resulting in a spectral resolution around 1 eV. The powdered composite supports and catalysts were suspended in isopropanol or hexane and drops of this suspension were dried onto stainless steel sample plates, which resulted in mechanically and electrically conductive samples. After measuring a survey spectrum, high resolution spectra were collected from the regions of interest (Mo 3d, Ti 2p, C 1s, O 1s, Na 1s).

Spectra were processed with the CasaXPS package [182] by fitting the measured data with a combination of Gaussian-Lorentzian product peaks over a Shirley-type background, while quantitative evaluation of the data was performed with the XPSMultiQuant package [183, 184], during which a homogeneous depth distribution was assumed for all components.

Chemical states were identified using the NIST database [185], the publication [186] or other literature as indicated. Binding energies were referenced to the lowest binding energy contribution of the C 1s envelope, which was assigned to graphite-like (sp^2-hybridized) carbon in the active carbon backbone (284.4 eV).

X-ray powder diffraction (XRD) patterns were obtained in a Philips model PW 3710 based PW 1050 Bragg-Brentano parafocusing goniometer using CuKα radiation (λ= 0.15418 nm), graphite monochromator and proportional counter. Silicon powder (NIST SRM 640) was used as an internal standard and the scans were evaluated with profile fitting methods. The cell parameters of the crystalline phases were determined from the fitted values.

Nitrogen physisorption measurements were carried out at −196 °C using Thermo Scientific Surfer automatic volumetric adsorption analyzer (Thermo Fischer Scientific, Berlin, Germany). The specific surface area was calculated by the BET method in the range of relative pressures from 0.05 to 0.30.

Thermogravimetric (TG) measurement was carried out with a PerkinElmer TGS-2 thermoscale in a compressed air atmosphere. The flow rate (volumetric flow) of the gas was 140 ml/min during the test. Approx. 1 mg sample was weighed. The TG furnace heat programme has heated the sample from room temperature (1-minute running time) to 900 °C at a heating speed of 5 °C/min.

Transmission electron microscopic images were taken by a Philips CM-10 transmission electron microscope with an accelerating voltage of 100 kV (University of Szeged).

Adsorption isotherms of the selected samples

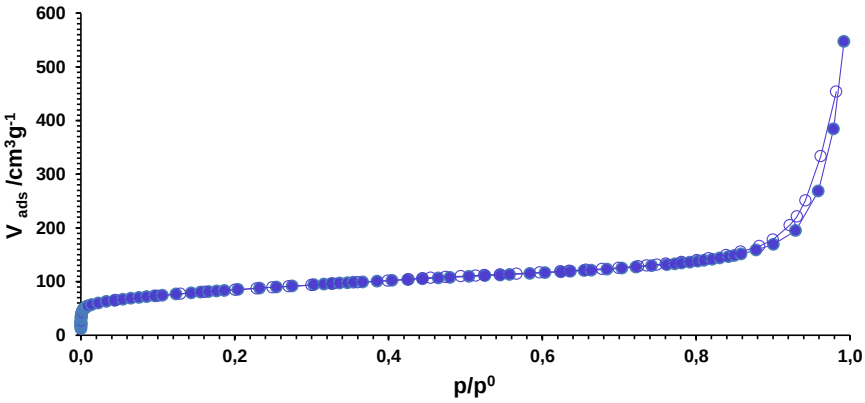

Figure A1. Adsorption isotherm of sample AI003/HT

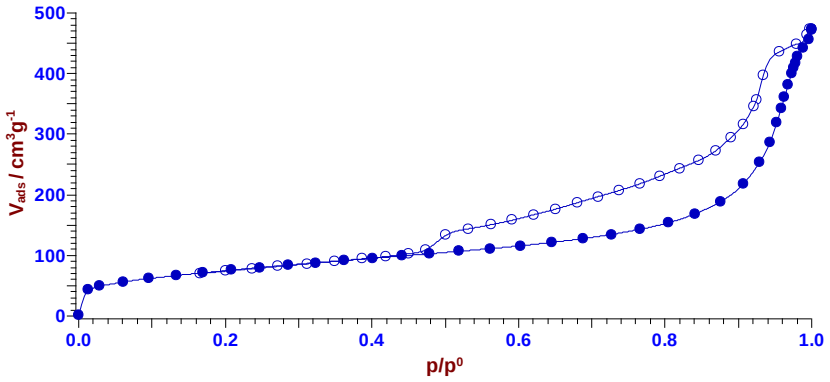

Figure A2. Adsorption isotherm of sample AI004/HT

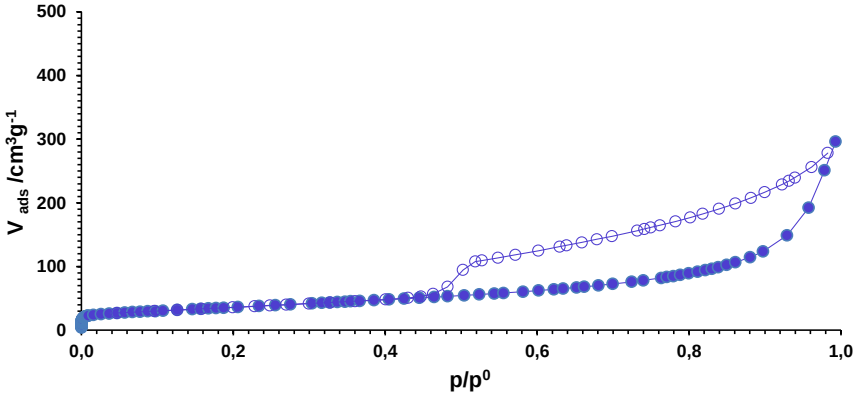

Figure A3. Adsorption isotherm of sample AI005/II/HT

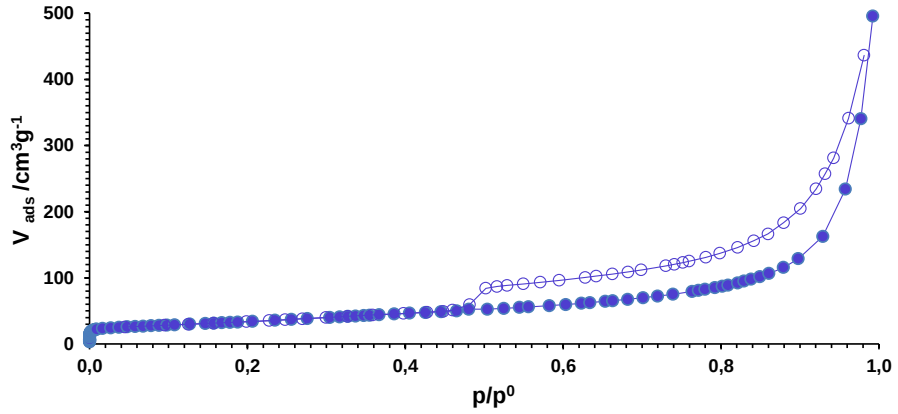

Figure A4. Adsorption isotherm of sample AI005/III/ST/HT

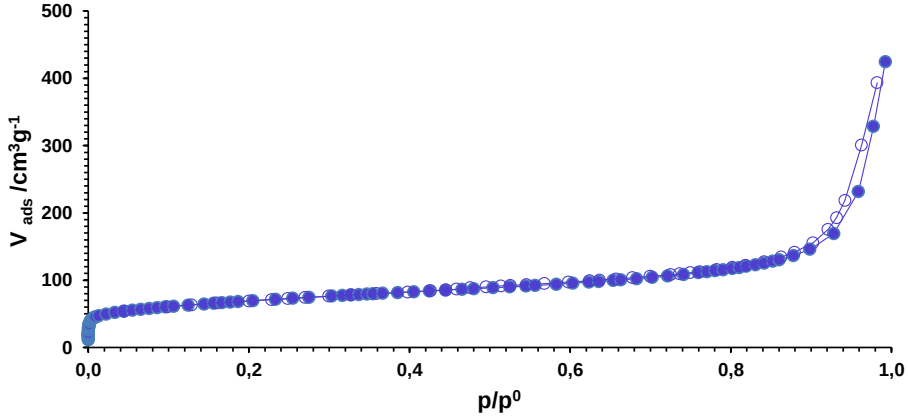

Figure A5. Adsorption isotherm of sample AI007/HT

Results of thermogravimetric test on Mo-containing selected samples

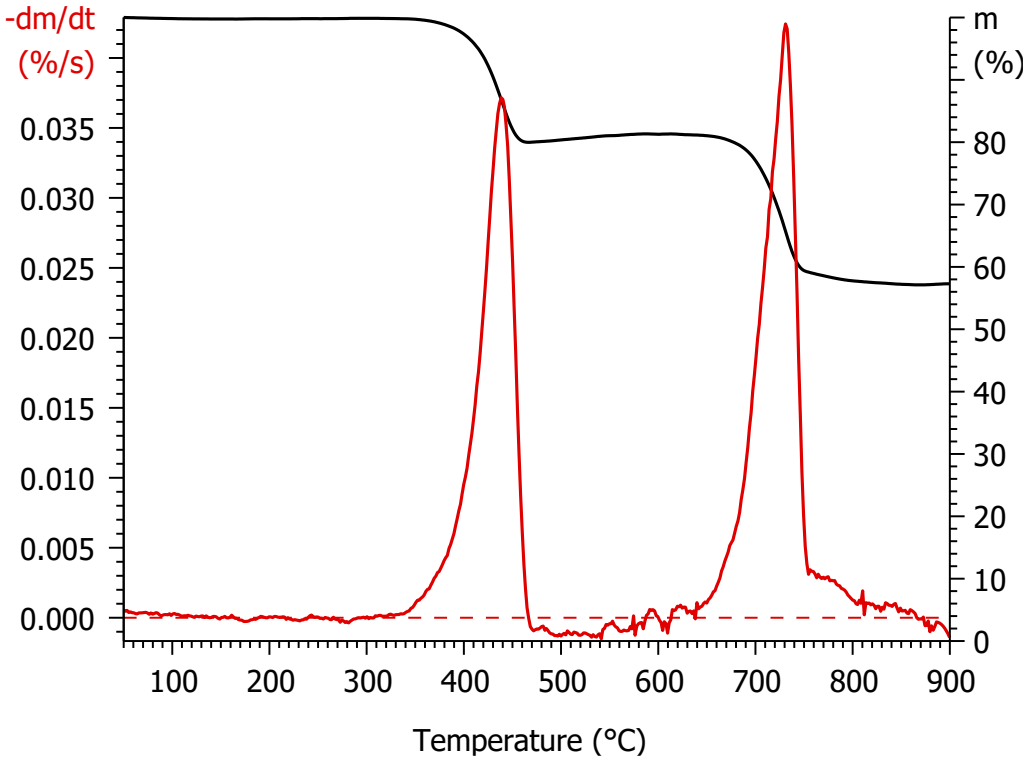

Figure A6. Mass (TGA) and mass loss rate (DTG) curves of sample AI005/II/HT

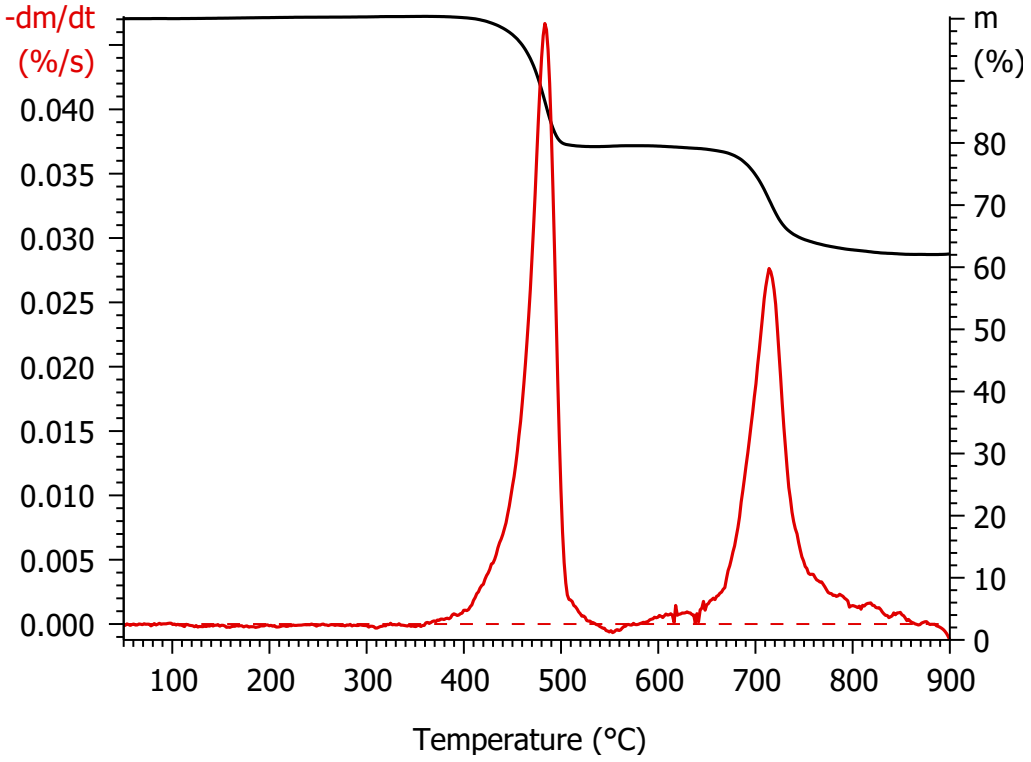

Figure A7. Mass (TGA) and mass loss rate (DTG) curves sample AI005/III/ST/HT

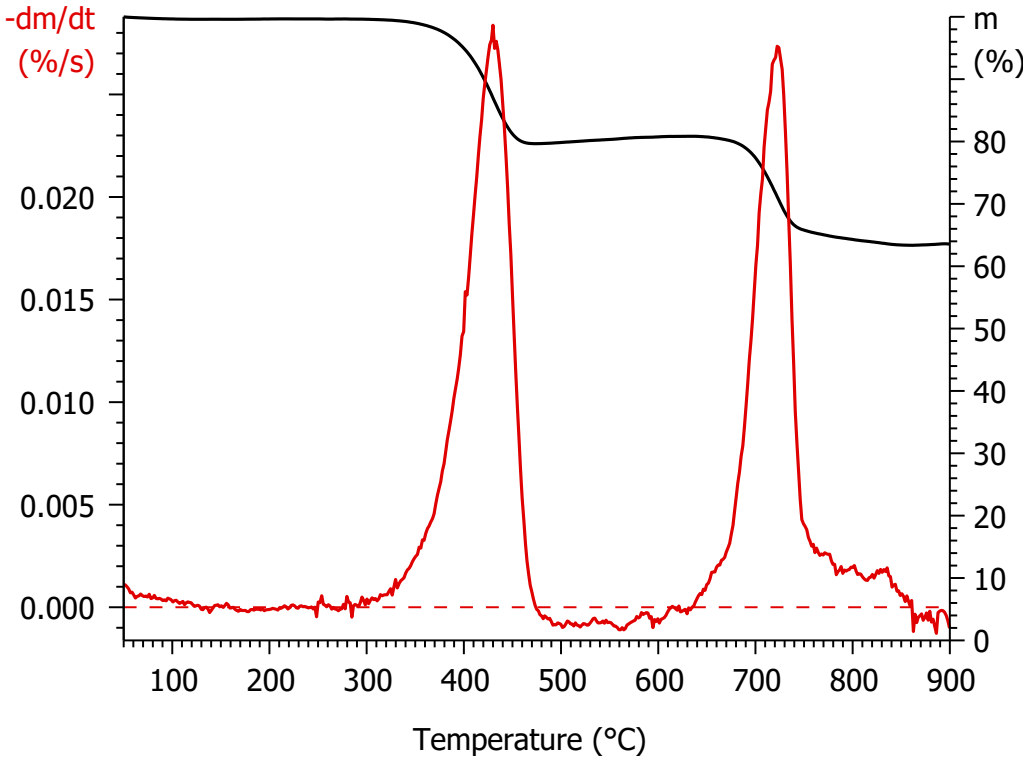

Figure A8. Mass (TGA) and mass loss rate (DTG) curves of sample AI007/HT

References

[1] L. Bicelli, "Hydrogen: a clean energy source," *Int. J. Hydr. Energy 11,* p. 555–565, 1986.

[2] The FreedomCAR and Fuel Partnership, "Hydrogen production: Overview of technology options," U.S. Department of Energy, NY, 2009.

[3] M. El-Shafie, S. Kambara and Y. Hayakawa, "Hydrogen Production Technologies Overview," *Journal of Power and Energy Engineering,* 2019.

[4] M. C. Williams, "Fuel Cell Handbook 7th edition," EG&G Technical Services, Inc., West Virginia, 2004.

[5] B. Viswanatha and M. A. Scibioh, Fuel Cells Principles and Applications, Chennai: Universities Press, 2007.

[6] Y. Wang, K. S. Chen, J. Mishler, S. C. Cho and X. C. Adroher, "A review of polymer electrolyte membrane fuel cells: Technology, applications, and needs on fundamental research," 2010.

[7] G. Wand, "Fuel cell history," *Fuel Cell Today,* vol. Part One. 14, 2006.

[8] G. Sandstede, J. E. Cairns, S. V. Bagotsky and K. Wiesener, "History of low temperature fuel cells," *Handbook of Fuel Cells – Fundamentals, Technology and Applications,* vol. 1, p. 145–218, 2010.

[9] Schönbein and Christian Friedrich, "On Voltaic Series and the Combination of Gases by Platinum," *Philosophical Magazine and Journal of Science,* vol. XIV, p. 86–87, 1839.

[10] O. Z. Sharaf and M. F. Orhan, "An overview of fuel cell technology: Fundamentals and applications," 2014.

[11] A. Lanz, J. Heffel and C. Messer, "Hydrogen Fuel Cell Engines and Related Technologies, Module 4: Fuel Cell Techology," College of the Desert, Energy Technology Training Center, CA, 2001.

[12] D. Hart, F. Lehner, S. Jones and J. Lewis, "The Fuel Cell Industry Review," 2019.

[13] F. Barbir, "Fuel Cell Applications. PEM Fuel Cells," 2013.

[14] G. Hoogers, Automotive Applications. In: Hoogers G, editor. Fuel Cell Technology Handbook., New York: CRC Press, 2003.

[15] Asia Pacific Fuel Cell Technologies Ltd, "APFCT fuel cell scooters complete 280 km run in Taiwan," *Fuel Cells Bulletin,* pp. 2-3, 2011.

[16] Asia Pacific Fuel Cell Technologies Ltd, "APFCT fuel cell scooter completes 'record' 1000 km test drive," *Fuel Cells Bull,* p. 3, 2010.

[17] Asia Pacific Fuel Cell Technologies Ltd, "APFCT wins funding for Taiwan fuel cell scooter test drive," *Fuel Cells Bulletin,* p. 1, 2005.

[18] Asia Pacific Fuel Cell Technologies Ltd, "APFCT for fleet demo of fuel cell scooters, micro cars in Taiwan," *Fuel Cells Bulletin,* p. 2, 2010.

[19] J. J. Hwang, "Review on development and demonstration of hydrogen fuel cell scooters," 2012.

[20] N. Behling, M. C. Williams and S. Managi, "Fuel cells and the hydrogen revolution: Analysis of a strategic plan in Japan," 2015.

[21] B. Paul and J. Andrews, "PEM unitised reversible/regenerative hydrogen fuel cell systems: State of the art and technical challenges," 2017.

[22] S. Mekhilef, R. Saidur and A. Safari, "Comparative study of different fuel cell technologies. Renew Sustain Energy Rev," 2012.

[23] M. Gurz, E. Baltacioglu, Y. Hames and K. Kaya, "The meeting of hydrogen and automotive: A review," 2017.

[24] V. S. BAGOTSKY, Fuel Cells, Moscow: John Wiley & Sons, Inc., 2012.

[25] S. Peighambardoust, S. Rowshanzamir and M. Amjadi, "Review of the proton exchange membranes for fuel cell applications," *International journal of hydrogen energy,* vol. 35, pp. 9349-9384, 2010.

[26] H. Yu, C. Hebling and S. Revathi, "Fuel Cells: Microsystems. Reference Module in Materials Science and Materials Engineering," *Elsevier,* 2016.

[27] X. Ren, Q. Lv, L. Liu, B. Liu, Y. Wang, A. Liu and G. Wu, "Current progress of Pt and Pt-based electrocatalysts used for fuel cells," *The Royal Society of Chemistry,* 2019.

[28] F. Foulkes and A. A.J., Fuel Cell Handbook, Melborne, FL: Krieger Publishing Company, 1993.

[29] T. Ralph and M. Hogarth, "Catalysis for low temperature fuel cells. Part I the cathode challenges platinum.," *Metals Rev.,* vol. 46, p. 3–14, 2002.

[30] I. Borbath, D. Guban, Z. Bakos, Z. Paszti, G. Gajdos, I. Sajo, Á. Vass and A. Tompos, "Exclusive formation of alloy phases via anchoring technique- From bimetallic catalysts to electrocatalysis," *Catal. Today,* vol. 306, pp. 58-70, 2018.

[31] D. Gubán, A. Tompos, I. Bakos, Z. Pászti, G. Gajdos, I. Sajó and I. Borbáth, "CO oxidation and oxygen reduction activity of bimetallic Sn-Pt electrocatalysts on carbon: effect of the microstructure and the exclusive formation of the Pt_3Sn alloy," *React. Kinet. Mech. Cat,* vol. 121, pp. 43-67, 2017.

[32] S. Mukerjee, R. Urian, S. Lee, E. Ticianelli and J. McBreen, "Electrocatalysis of CO tolerance by carbon-supported PtMo electrocatalysts in PEMFCs," *J. Electrochem. Soc.,* vol. 151, pp. A1094-A1103, 2004.

[33] J. P. Ross, K. Kinoshita, A. Scarpellino and P. Stonehart, "Electrocatalysis on binary alloys. II. Oxidation of molecular hydrogen on supported Pt + Ru alloys," *J. Electroanal. Chem.,* vol. 63, pp. 97-110, 1975.

[34] S. Huang, C. Chang, K. Wang and C. Yeh, "Promotion of platinum - ruthenium catalyst for electrooxidation of methanol by crystalline ruthenium dioxide," *Chem. Phys. Chem.,* vol. 8, pp. 1774-1777., 2007.

[35] X. Yu, Q. Zhang, Y. Ling, Z. Yang and H. Cheng, "Promoted stability and electrocatalytic activity of PtRu electrocatalyst derived from coating by cerium oxide with high oxygen storage capacity," *Appl. Surf. Sci.,* vol. 455, p. 815–820, 2018.

[36] D. Gubán, CO-toleráns anódoldali elektrokatalizátorok előállítása polimer elektrolit membrános tüzelőanyag-elemekhez, Budapest: PhD Dissertation, Budapest University of Technology and Economics,, 2015.

[37] B. Meier, C. Galeano, I. Katsounaros, A. Topalov, A. Kostka and F. Schuuth, "Degradation mechanisms of Pt/C fuel cell catalysts under simulated start-stop conditions," *ACS Catal,* p. 832–843, 2012.

[38] Á. Vass, I. Borbáth, Z. Pászti, I. Bakos, I. Sajó, P. Németh and A. Tompos, "Effect of Mo incorporation on electrocatalytic performance of Ti-Mo mixed oxide-carbon composite supported Pt electrocatalysts," *React Kinet Mech Cat 121,* p. 141–160, 2017.

[39] C. Subban, Q. Zhou, B. Leonard, C. Ranjan, H. Edvenson and F. DiSalvo, "Catalyst supports for polymer electrolyte fuel cells," *Phil Trans R Soc A,* pp. 3243-3253, 2010.

[40] S. Huang, P. Ganesan and B. Popov, "Titania supported platinum catalyst with high electrocatalytic activity and stability for polymer electrolyte membrane fuel cell," *Appl Catal B Environ,* pp. 75-81, 2011.

[41] A. Kumar and V. Ramani, "$Ta_{0.3}Ti_{0.7}O_2$ electrocatalyst supports exhibit exceptional electrochemical stability," *J. Electrochem Soc,* vol. 160, pp. F1207-F1215, 2013.

[42] D. Gubán, I. Borbáth, Z. Pászti, I. Sajó, E. Drotár, M. Hegedus and A. Tompos, "Preparation and characterization of novel $Ti_{0.7}W_{0.3}O_2$–C composite materials for Pt-based anode electrocatalysts with enhanced CO tolerance," *Applied Catalysis B: Environmental,* p. 455–470, 2015.

[43] A. Tseung and K. Chen, "Hydrogen spill-over effect on Pt/WO_3 anode catalysts," *Catal Today,* pp. 38:439-43, 1997.

[44] J. Meier, F. Schuüth, K. Mayrhofer, C. Galeano, I. Katsounaros, A. Topalov and A. Kostka, "Degradation mechanisms of Pt/C fuel cell catalysts under simulated start-stop conditions," *ACS Catal 2(5),* p. 832–843, 2002.

[45] Á. Vass, I. Borbáth, I. Bakos, Z. Pászti, I. E. Sajó and A. Tompos, "Novel Pt Electrocatalysts: Multifunctional Composite Supports for Enhanced Corrosion Resistance and Improved CO Tolerance," *Topics in Catalysis,* vol. 61, p. 1300–1312, 2018.

[46] K. Kinoshita, "Carbon," *Wiley,* p. 316–333, 1988.

[47] O. Lori and L. Elbaz, "Advances in Ceramic Supports for Polymer Electrolyte Fuel Cells," *Catalysts,* vol. 5, pp. 1445-1464, 2015.

[48] D. Gubán, Z. Pászti, I. Borbáth, I. Bakos, E. Drotár, I. Sajó and A. Tompos, "Design and Preparation of CO Tolerant Anode Electrocatalysts for PEM Fuel Cells," *Periodica Polytechnica Chemical Engineering,* pp. 29-39, 2016.

[49] K. Kinoshita and J. Bett, "Electrochemical oxidation of carbon black in concentrated phosphoric acid at 135°C," *Carbon,* vol. 11, p. 237, 1973.

[50] K. Kangasniemi, D. Condit and T. Jarvi, "Characterization of vulcan electrochemically oxidized under simulated PEM fuel cell conditions," *J. Electrochem. Soc. 151 (4),* pp. E125-E132, 2004.

[51] R. Borup, J. Meyers, B. Pivovar, Y. Kim, R. Mukundan, N. Garland, D. Myers, M. Wilson, F. Garzon and D. Wood, "Scientific aspects of polymer electrolyte fuel cell durability and degradation," *Chem. Rev. 107,* p. 3904–3951, 2007.

[52] X. Wang, W. Li, Z. Chen, M. Waje and Y. Yan, "Durability investigation of carbon nanotube as catalyst support for proton exchange membrane fuel cell," *J. Power Sources,* p. 154–159, 2006.

[53] X. Zhou, J. Qiao, L. Yang and J. Zhang, "A Review of Graphene-Based Nanostructural Materials for Both Catalyst Supports and Metal-Free Catalysts in PEM Fuel Cell Oxygen Reduction Reactions," *Adv. Energy Mater, 4,* p. 1301523:1–1301523:25., 2014.

[54] Q. Lv, M. Yin, P. Zhao, C. Li, C. Liu and W. Xing, "Promotion effect of TiO_2 on catalytic activity and stability of Pt catalyst for electrooxidation of methanol," *J Power Sources 218,* p. 93–99, 2012.

[55] K. Blackmore, L. Elbaz, E. Bauer, E. Brosha, K. More, T. McCleskey and A. Burrell, "High Surface Area Molybdenum Nitride Support for Fuel Cell Electrodes," *J. Electrochem. Soc. 158,* p. B1255–B1259, 2011.

[56] X. Cui, L. Guo, F. Cui, Q. He and J. Shi, "Electrocatalytic activity and co tolerance properties of mesostructured Pt/WO_3 composite as an anode catalyst for pemfcs.," *J. Phys. Chem. C 113,* p. 4134–4138, 2009.

[57] N. Elezović, L. Gajić-Krstajić, L. Vračar and N. Krstajić, "Effect of chemisorbed CO on MoO_x-Pt/C electrode on the kinetics of hydrogen oxidation reaction," *International Journal of Hydrogen Energy,* vol. 35, pp. 12878-12887, 2010.

[58] E. Santiago, M. Batista, E. Assaf and E. Ticianelli, "Mechanism of CO Tolerance on Molybdenum-Based Electrocatalysts for PEMFC," *J. Electrochem. Soc. 151,* pp. A944-A949, 2004.

[59] Z. Yan, J. Xie, J. Jing, M. Zhang, W. Wei and S. Yin, "MoO_2 nanocrystals down to 5 nm as Pt electrocatalyst promoter for stable oxygen reduction reaction," *Int. J. Hydrogen Energy,* vol. 37, pp. 15948-15955, 2012.

[60] F. Martins Pedro and E. Ticianelli, "Electrocatalytic Activity and Stability of Platinum Nanoparticles Supported on Carbon-Molybdenum Oxides for the Oxygen Reduction Reaction," *Chem. electrochem.,* vol. 2, pp. 1298-1306, 2015.

[61] Y. Takabatake, Z. Noda, S. Lyth, H. A. and K. Sasaki, "Cycle durability of metal oxide supports for PEFC electrocatalysts," *Int. J. Hydrogen Energy,* vol. 39, p. 5074–5082, 2014.

[62] D. Guban, A. Tompos, I. Bakos, A. Vass, Z. Paszti, G. E. Szabo, I. Sajo and I. Borbath, "Preparation of CO-tolerant anode electrocatalysts for polymer electrolyte membrane fuel cells," *International Journal of Hydrogen energy 42,* pp. 13741-13753, 2017.

[63] K. Tiido, N. Alexeyeva, M. Couillard, C. Bock, B. R. MacDougall and K. Tammeveski, "Graphene–TiO_2 composite supported Pt electrocatalyst for oxygen reduction reaction," *Electrochimica Acta 107,* p. 509–517, 2013.

[64] R. Li, H. Hao, T. Huang and A. Yu, "Electrodeposited Pd-MoO_x catalysts withenhanced catalytic activity for formic acid electrooxidation," *Electrochim. Acta,* vol. 76, pp. 292-299, 2012.

[65] T. Ioroi, K. Yasuda, Z. Siroma, N. Fujiwara and Y. Miyazaki, "Enhanced CO tolerance of carbon supported platinum and molybdenum oxide anode catalyst," *J. Electrochem. Soc.,* vol. 150, p. A1225–A1230, 2003.

[66] L. Ordóñez, P. Roquero, P. Sebastian and J. Ramírez, "CO oxidation on carbonsupported PtMo electrocatalysts: Effect of the platinum particle size," *Int. J. Hydrogen Energy,* vol. 32, pp. 3147-3153, 2007.

[67] K. Mayrhofer, K. Hartl, V. Juhart and M. Arenz, "Degradation of CarbonSupported Pt Bimetallic Nanoparticles by Surface Segregation," *J. Am. Chem. Soc.,* vol. 131, pp. 16348-16349, 2009.

[68] Á. Vass, I. Borbáth, I. Bakos, Z. Pászti, G. Sáfrán and A. Tompos, "Stability issues of CO tolerant Pt based electrocatalysts for polymer electrolyte membrane fuel cells: comparison of $Pt/Ti_{0.8}Mo_{0.2}O_2$–C with PtRu/C," *Reaction Kinetics, Mechanisms and Catalysis 126,* p. 679–699, 2019.

[69] A. Aguiar and P. Olivi, "Characterization and voltammetric behavior of $Pt_yMo_zO_x$ C electrodes prepared by the thermal decomposition of polymeric precursors," *J. Power Sources 195,* p. 3485–3489, 2010.

[70] D. Dos Anjos, K. Kokoh, J. Léger, A. De Andrade, P. Olivi and G. Tremiliosi-Filho, "Electrocatalytic oxidation of ethanol o Pt-Mo bimetallic electrodes in acid medium," *J. Appl. Electrochem. 36,* p. 1391–1397, 2006.

[71] S. Mukerjee and R. Urian, "Bifunctionality in Pt alloy nanocluster electrocatalysts for enhanced methanol oxidation and CO tolerance in PEM fuel cells: electrochemical and in situ synchrotron spectroscopy," *Electrochim. Acta 47,* p. 3219–3231, 2012.

[72] G. Papakonstantinou, F. Paloukis, A. Siokou and S. Neophytides, "The electrokinetics of CO oxidation on Pt_4Mo(20wt%)/C interfaced with Nafion membrane," *J. Electrochem. Soc. 154,* p. B989–B997., 2007.

[73] B. Grgur, N. Markovic and P. Ross, "The electro-oxidation of H_2 and H_2/CO mixtures on carbon-supported Pt_xMo_y alloy catalysts," *J. Electrochem. Soc. 146,* pp. 1613-1619, 1999.

[74] J. Hu, L. Z., B. Eichhorn and G. Jackson, "CO tolerance of nanoarchitectured Pt-Mo anode electrocatalysts for PEM fuel cells," *Int. J. Hydrogen Energy 37,* p. 11268–11275, 2012.

[75] F. Micoud, F. Maillard, A. Gourgaud and M. Chatenet, "Unique CO-tolerance of Pt-WO_x materials," *Electrochem. Commun. ,* vol. 11, p. 651–654, 2009.

[76] F. Maillard, E. Peyrelade, Y. Soldo-Olivier, M. Chatenet, E. Chaînet and R. Faure, "Is carbon-supported Pt-WO_x composite a CO-tolerant material?," *Electrochimica Acta 52,* pp. 1958-1967, 2007.

[77] G. Nagy and R. Schiller, "Hydrogen in tungsten bronzes: mechanism of hydrogen intercalation," *International Journal of Hydrogen Energy,* vol. 14, pp. 567-572, 1989.

[78] N. Hammer, I. Kvande, X. Xu, V. Gunnarsson, B. Tøtdal, D. Chen and M. Rønning, "Au-TiO_2 catalysts on carbon nanofibres prepared by deposition-precipitation and from colloid solutions," *Catal. Today 123,* pp. 245-256, 2007.

[79] W. Han, Z. Tang, P. Zhang, G. Lu and X. Pan, "Fabrication and catalytic properties of Pd and Ce decorated carbon nanotube-TiO_2 composite catalysts for low-temperature CO oxidation," *Colloids. Surf. A 460,* pp. 422-428, 2014.

[80] W. Vogel, L. Timperman and N. Alonso-Vante, "Probing metal substrate interaction of Pt nanoparticles: Structural XRD analysis and oxygen reduction reaction.," *Appl. Catal. A: General 377,* p. 167–173, 2010.

[81] K. Huang, K. Sasaki, R. Adzic and Y. Xing, "Increasing Pt oxygen reduction reaction activity and durability with a carbon-doped TiO_2 nanocoating catalyst support," *J. Mater. Chem. 22,* pp. 16824-16832, 2012.

[82] A. Zhao, J. Masa and W. Xia, "Very low amount of TiO_2 on N-doped carbon nanotubes significantly improves oxygen reduction activity and stability of supported Pt nanoparticles," *Phys. Chem. Chem. Phys. 17,* pp. 10767-10773 , 2015.

[83] Y. Wang, A. Tabet-Aoul and M. Mohamedi, "Laser synthesis of hierarchically organized nanostructured TiO_2 films on microfibrous carbon paper substrate: Characterization and electrocatalyst supporting properties," *J. Power Sources 299,* pp. 149-155, 2015.

[84] C. Coromelci-Pastravanu, M. Ignat, E. Popovici and V. Harabagiu, "TiO_2-coated mesoporous carbon: Conventional vs. microwave-annealing process," *J. Hazard. Mater. 278,* pp. 382-390, 2014.

[85] X. Zhang, M. Zhou and L. Lei, "Preparation of photocatalytic TiO_2 coatings of nanosized particles on activated carbon by AP- MOCVD," *Carbon 43,* pp. 1700-1708, 2005.

[86] A. Bauer, C. Song, A. Ignaszak, R. Hui, J. Zhang, L. Chevallier, D. Jones and J. Roziére, "Improved stability of mesoporous carbon fuel cell catalyst support through incorporation of TiO_2," *Electrochim. Acta 55,* pp. 8365-8370, 2010.

[87] X. Liu, J. Chen, G. Liu, L. Zhang, H. Zhang and B. Yi, "Enhanced long-term durability of proton exchange membrane fuel cell cathode by employing Pt/TiO_2/C catalysts.," *J. Power Sources 195,* pp. 4098-4103, 2010.

[88] S. v. Kraemer, K. Wikander, G. Lindbergh, A. Lundblad and A. Palmqvist, "Evaluation of TiO_2 as catalyst support in Pt-TiO_2/C composite cathodes for the proton exchange membrane fuel cell.," *J. Power Sources 180,* pp. 185-190, 2008.

[89] C. Subban, Q. Zhou, A. Hu, T. Moylan, F. Wagner and F. DiSalvo, "Sol-Gel Synthesis, Electrochemical Characterization, and Stability Testing of $Ti_{0.7}W_{0.3}O_2$ Nanoparticles for Catalyst Support Applications in Proton-Exchange Membrane," *Fuel Cells Journal of American chemical Society 132,* pp. 17531-17536, 2010.

[90] S. Iijima and T. Ichihashi, "Single-shell carbon nanotubes of 1-nm diameter," *Nature 363,* p. 603–605, 1993.

[91] D. S. Bethune, C. H. Kiang, M. S. De Vries, G. Gorman, R. Savoy, J. Vazquez and R. Beyers, "Cobalt-catalyzed growth of carbon nanotubes with single-atomic-layer walls," *Nature. 363 (6430),* p. 605–607, 1993.

[92] S. Iijima, "Helical microtubules of graphitic carbon," *Nature 354, 56–58,* 1991.

[93] P. Serp and M. C. P. Kalck, "Carbon nanotubes and nanofibers in catalysis," *Appl. Catal. A: General 253,* p. 337–358, 2003.

[94] V. K. Gupta and T. A. Saleh, "Synthesis of Carbon Nanotube-Metal Oxides Composites; Adsorption and Photo-degradation," 2011. [Online]. Available: http://cdn.intechweb.org/pdfs/16834.pdf.

[95] C. Ming-liang, Z. Feng-jun and W.-c. Oh, "Synthesis, characterization, and photocatalytic analysis of CNT/TiO_2 composites derived from MWCNTs and titanium sources New Carbon Materials," p. 24(2):159–166., 2009.

[96] M. M. Mohamed, S. Eid and A. El-Etre, "Methanol photo-oxidation at graphene and carbon nanotubes modified TiO_2 nanosheets electrocatalysts," *J. Photochem. Photobiol. A: Chemistry 338,* p. 37–48, 2017.

[97] T. S. Natarajan, J. Y. Lee, H. C. Bajaj, W.-K. Jo and R. J. Tayade, "Synthesis of multiwall carbon nanotubes/TiO_2 nanotube composites with enhanced photocatalytic decomposition efficiency," *Catal Today 282,* pp. 13-23, 2016.

[98] K. Woan, G. Pyrgiotakis and W. Sigmund, "Photocatalytic Carbon-Nanotube–TiO_2 Composites," *Adv. Mater.,* p. 2233–2239, 2009.

[99] P. Trogadas, T. F. Fuller and P. Strasser, "Carbon as catalyst and support for electrochemical energy conversion," *Carbon 75,* no. and the references cited therein, pp. 5-42, 2014.

[100] D. Zhou, L. Ding, H. Cui, H. An, J. Zhai and Q. Li, "Fabrication of Pd/TiO_2-multiwall carbon nanotubes catalyst and investigation of its electrocatalytic activity for formic acid oxidation," *Journal of Power Sources 222,* pp. 510-517, 2013.

[101] Y.-X. Wang, J. Xie, G.-S. Cao and T.-J. Zhu, "Electrochemical performance of TiO_2/carbon nanotubes nanocomposite prepared by an in situ route for Li-ion batteries," *Journal of Materials Research 27,* pp. 417-423., 2012.

[102] D.-J. Guo, X.-P. Qiu, L.-Q. Chena and W.-T. Zhua, "Multi-walled carbon nanotubes modified by sulfated TiO_2 – A promising support for Pt catalyst in a direct ethanol fuel cell," *Carbon 47,* p. 1680 –1685, 2009.

[103] S. V. Selvaganesh, P. Dhanasekaran and S. D. Bhat, "TiO_2 nanowire/MWCNT composite with enhanced performance and durability for polymer electrolyte fuel cells," *Electrochem. Energy Technol 3,* p. 9–26, 2017.

[104] F. Hasche, M. Oezaslana and P. Strasser, "Activity, stability and degradation of multi walled carbon nanotube (MWCNT) supported Pt fuel cell electrocatalysts," *Phys. Chem. Chem. Phys, 12,,* p. 15251–15258, 2010.

[105] Z.-Z. Jiang, Z.-B. Wang, W.-L. Qu, D.-M. Gu and G.-P. Yin, "Synthesis and characterization of carbon riveted Pt/MWCNTs@TiO_2–TiC catalyst with high durability for PEMFCs application," *Applied Catalysis B: Environmental 123– 124,* p. 214– 220, 2012.

[106] C. Montero-Ocampo, J. V. Garcia and E. A. Estrada, "Comparison of TiO_2 and TiO_2-CNT as Cathode Catalyst Supports for ORR," *Int. J. Electrochem. Sci., 8,* p. 12780 – 12800, 2013.

[107] M. Eckardt, C. Gebauer, Z. Jusys, M. Wassner, N. Hüsing and R.J. Behm, "Oxygen reduction reaction activity and long-term stability of platinum nanoparticles supported on titania and titania-carbon nanotube composites," *Journal of Power Sources 400,* 2018.

[108] W. Zhang, J. Chen, G. F. Swiegers, Z.-F. Ma and G. G. Wallace, "Microwave-assisted synthesis of Pt/CNT nanocomposite electrocatalysts for PEM fuel cells," *Nanoscale, 2,* p. 282–286, 2016.

[109] B. Smith, K. Wepasnick, K. E. Schrote, H.-H. Cho, W. P. Ball and D. H. Fairbrother, "Influence of Surface Oxides on the Colloidal Stability of Multi-Walled Carbon Nanotubes: A Structure-Property Relationship," *Langmuir, 25(17),* 2009.

[110] IUPAC, "Graphene layer," in *IUPAC Recommendations*, Oxford, Blackwell Scientific Publications, 1995, p. 491.

[111] H. P. Boehm, A. Clauss, G. O. Fischer and U. Hofmann, "Das Adsorptionsverhalten sehr dünner Kohlenstoff-Folien," *Zeitschrift für Anorganische und Allgemeine Chemie. 316 (3–4): 119–127,* 1 July 1962.

[112] K. S. Novoselov, A. K. Geim, S. V. Morozov, D. Jiang, Y. Zhang, S. V. Dubonos, I. V. Grigorieva and A. A. Firsov, "Electric Field Effect in Atomically Thin Carbon Films," *Science. 306 (5696),* p. 666–669, 2004.

[113] A. Halder, M. Zhang and Q. Chi, "Electrocatalytic Applications of Graphene–Metal Oxide Nanohybrid Materials," *Chapter 14,* 2016.

[114] E. Antolini, "Graphene as a new carbon support for low-temperature fuel cell catalysts," *Applied Catalysis B: Environmental 123– 124,* p. 52– 68, 2012.

[115] L. T. Soo, K. S. Loh, A. B. Mohamad, W. R. W. Daud and W. Y. Wong, "An overview of the electrochemical performance of modified graphene used as an electrocatalyst and as a catalyst support in fuel cells," *Applied Catalysis A: General 497,* pp. 198-210, 2015.

[116] K. Tiido, N. Alexeyeva, M. Couillard, C. Bock, B. R. MacDougall and K. Tammeveski, "Graphene–TiO_2 composite supported Pt electrocatalyst for oxygenreduction reaction," *Electrochimica Acta 107,* p. 509–517, 2013.

[117] S. Park and R. S. Ruoff, "Chemical methods for the production of graphenes," *Nature Nanotechnology 4,* pp. 217-224, 2009.

[118] N. Zhang, M. Yang, S. Liu, Y. Sun and Y. J. Xu, "Waltzing with the versatile platform of graphene to synthesize composite photocatalysts," *Chem. Rev. 115,* vol. and the references cited herein, pp. 10307-10377, 2015.

[119] Y. Park, S. Kang and W. Choi, "Exfoliated and reorganized graphite oxide on titania nanoparticles as an auxiliary co-catalyst for photocatalytic solar conversion," *Phys Chem Chem Phys 13,* pp. 9425-9431, 2011.

[120] B. Brodie, "On the atomic weight of graphite," *Phil Trans R Soc Lond 149,* pp. 249-259, 1859.

[121] Hummers WS and Offeman RE, "Preparation of graphitic oxide," *J Am Chem Soc 80,* pp. 1339-1339, 1958.

[122] D. Marcano, D. Kosynkin, J. Berlin, A. Sinitskii, Z. Sun, A. Slesarev, L. Alemany, W. Lu and J. Tour, "Improved synthesis of graphene oxide," *ACS Nano 4,* pp. 4806-4814, 2010.

[123] S. You, S. Luzan, T. Szabó and A. Talyzin, "Effect of synthesis method on solvation and exfoliation of graphite oxide," *Carbon 52,* pp. 171-180, 2013.

[124] T. Szabó, O. Berkesi, P. Forgó, K. Josepovits, Y. Sanakis, D. Petridis and I. Dékány, "Evolution of surface functional groups in a series of progressively oxidized graphite oxides," *Chem Mater 18,* pp. 2740-2749, 2006.

[125] U. Hofman and R. Holst, "Über die Säurenatur und die Methylierung von Graphitoxyd," *Ber. Dtsch. Chem. Ges. 72,* pp. 754-762, 1939.

[126] G. Ruess, "Über das Graphitoxyhydroxyd (Graphitoxyd)," *Monatsh. Chem., 76,* p. 381–417, 1946.

[127] W. Scholz and H. Boehm, "Untersuchungen am Graphitoxid. VI. Betrachtungen zur Struktur des Graphitoxids," *Z. Anorg. Allg. Chem., 369,* p. 327–340, 1969.

[128] T. Nakajima, A. Mabuchi and R. Hagiwara, "A nev structure model of graphite oxide," *Carbon, 26,* p. 357–361, 1988.

[129] N. Tsuyoshi and M. Yoshiaki, "Formation process and structure of graphite oxide," *Carbon, 32,* p. 469–475, 1994.

[130] H. He, T. Riedl, A. Lerf and K. J., "Solid-State NMR Studies of the Structure of Graphite Oxide," *J. Phys. Chem., 100,* p. 19954–19958, 1996.

[131] H. He, J. Klinowski, M. Forster and L. A., "A new structural model for graphite oxide," *Chemical Physics Letters. 287,* pp. 53-56, 1998.

[132] D. R. Dreyer, S. Park, C. W. Bielawski and R. S. Ruoff, "The chemistry of graphene oxide," *Chem. Soc. Rev, 39,* p. 228–240, 2010.

[133] T. Szabó, E. Tombácz, E. Illés and I. Dékány, "Enhanced acidity and pH dependent surface charge characterisation of successively oxidized graphite oxides," *Carbon 44,* pp. 357-545, 2006.

[134] A. Lerf, H. He, M. Foster and J. Klinowski, "Structure of graphite oxide revisited," *J Phys Chem B 102,* pp. 4477-4482, 1998.

[135] P. Ruz, S. Banerjee, M. Pandey, V. Sudarsan, P. Sastry and R. J. Kshirsagar, "Structural evolution of turbostratic carbon: Implications in H_2 storage," *Solid State Sciences 62,* pp. 105-111, 2016.

[136] M. V. Gudkov, S. L. Bazhenov, L. S. Bekhli and V. P. Mel'nikov, "Explosive Reduction of Graphite Oxide Russian," *Journal of Physical Chemistry B, No. 5,* vol. 12, no. and the references cited herein, p. 860–868, 2018.

[137] H. Boehm and W. Scholz, "Der "Verpuffungpunkt" des Graphitoxyds," *Z Anorg Allg Chem, 335,* pp. 74-79, 1965.

[138] A. Klechikov, G. Mercier, T. Sharifi, I. A. Baburin, G. Seifert and A. V. Talyzin, "Hydrogen storage in high surface area graphene scaffolds," *Chemical Communications, 51,* pp. 15280-15283, 2015.

[139] N. Roy, K. T. Leung and D. Pradhan, "Nitrogen doped reduced graphene oxide based Pt-TiO_2 nanocomposites for enhanced hydrogen evolution," *J. Phys. Chem. C, 119,* pp. 19117-19125, 2015.

[140] Q. Zhang, Y. He, X. Chen, D. Hu, L. Li, T. Yin and L. Ji, "Structure and photocatalytic properties of TiO_2-Graphene oxide intercalated composite," *Chinese Sci. Bull. 56,* pp. 331-339, 2011.

[141] Y. Liang, H. Wang, H. Casalongue, Z. Chen and H. Dai, "TiO_2 nanocrystals grown on graphene as advanced photocatalytic hybrid materials," *Nano Res. 3,* pp. 701-705, 2010.

[142] T. Szabó, Á. Veres, E. Cho, J. Khim, N. Varga and I. Dékány, "Photocatalyst separation from aqueous dispersion using graphene oxide/TiO_2 nanocomposites," *Colloids and Surfaces A: Physicochem. Eng. Aspects 433,* pp. 230-239, 2013.

[143] T. Szabó, A. Szeri and I. Dékány, "Composite graphitic nanolayers prepared by self-assembly between finely dispersed graphite oxide and a cationic polymer," *Carbon 43,* pp. 87-94, 2005.

[144] W. Zhuang, L. He, J. Zhu, R. An, X. Wu, L. Mu, X. Lu, L. Lu, X. Liu and H. Ying, "TiO_2 nanofibers heterogeneously wrapped with reduced graphene oxide as efficient Pt electrocatalyst supports for methanol oxidation," *Int. J. Hydrogen Energy 40,* pp. 3679-368, 2015.

[145] H. Zhang, X. J. Lv, Y. Li, Y. Wang and J. Li, "P25-graphene composite as a high performance photocatalyst.," *ACS Nano 4,* pp. 380-386, 2010.

[146] Y. Zhang, Z. Tang, X. Fu and Y. Xu, "TiO_2-graphene nanocomposites for gas-phase photocatalytic degradation of volatile aromatic pollutant: Is TiO_2-graphene truly different from other TiO_2-carbon composite materials?," *ACS Nano, 4,* pp. 7303-7314, 2010.

[147] X. Pan, Y. Zhao, S. Liu, C. Korzeniewski, S.Wang and Z. Fan, "Comparing graphene-TiO_2 nanowire and graphene-TiO_2 nanoparticle composite photocatalysts," *ACS Appl. Mater. Interfaces 4,* p. 3944−3950, 2012.

[148] K. Leong, L. Sim, D. Bahnemann, M. Jang, S. Ibrahim and Ű. Saravanan, "Reduced graphene oxide and Ag wrapped TiO_2 photocatalyst for enhanced visible light photocatalysis," *APL Mater 3,* 2015.

[149] P. Zeng, Q. Zhang, X. Zhang and T. Peng, "Graphite oxide–TiO_2 nanocomposite and its efficient visible-light-driven photocatalytic hydrogen production," *J Alloys Comp 516,* pp. 85-90, 2012.

[150] E. Vasilaki, I. Georgaki, D. Vernardou, M. Vamvakaki and N. Katsarakis, "Ag-loaded TiO_2/reduced graphene oxide nanocomposites forenhanced visible-light photocatalytic activity," *Appl Surf Sci 353,* pp. 865-872, 2015.

[151] B. A. Faraldos M, " Environmental applications of titania-graphene photocatalysts," *Catal Today 285,* pp. 13-28, 2017.

[152] A. A. Ismail, R. Geioushy, H. Bouzid, S. A. Al-Sayari, A. Al-Hajry and D. W. Bahnemann, "TiO_2 decoration of graphene layers for highly efficient photocatalyst: Impact of calcination at different gas atmosphere on photocatalytic efficiency," *Applied Catalysis B: Environmental 129,* p. 62–70, 2013.

[153] G. Nagaraju, K. Manjunath, S. Sarkar, E. Gunter, S. R. Teixeira and J. Dupont, "TiO_2-RGO hybrid nanomaterials for enhanced water splitting reaction," *International Journal of Hydrogen Energy 40,* pp. 12209-12216, 2015.

[154] W. Fan, Q. Lai, Q. Zhang and Y. Wang, "Nanocomposites of TiO_2 and Reduced Graphene Oxide as Efficient Photocatalysts for Hydrogen Evolution," *J. Phys. Chem. C 115,* p. 10694–10701, 2011.

[155] K. Majrik, Á. Turcsányi, Z. Pászti, T. Szabó, A. Domján, J. Mihály, A. Tompos, I. Dékány and E. Tálas, "Graphite Oxide-TiO_2 Nanocomposite Type Photocatalyst for Methanol Photocatalytic Reforming Reaction," *Topics in Catalysis, 61,* p. 1323–1334, 2018.

[156] X. Zhang, Q. Liu, X. Shi, A. M. Asiri, Y. Luo and X. S. T. Li, *J. Mater. Chem. A, 6,* p. 17303–17306, 2018.

[157] H. Zhang, X. Han and Y. Zhao, "Pd-TiO_2 nanoparticles supported on reduced graphene oxide: Green synthesis and improved electrocatalytic performance for methanol oxidation," *Journal of Electroanalytical Chemistry 799,* p. 84–91, 2017.

[158] L. Zhao, Z.-B. Wang, J. Liu, J.-J. Zhang, X.-L. Sui, L.-M. Zhang and D.-M. Gu, "Facile one-pot synthesis of Pt/graphene-TiO_2 hybrid catalyst with enhanced methanol electrooxidation performance," *Journal of Power Sources 279,* pp. 210-217, 2015.

[159] M. Wang, Z. Wang, L. Wei, J. Li, X. Zhao, M. Wang, Z. Wang, L. Wei, J. Li and X. Zhao, "Catalytic performance and synthesis of a Pt/graphene-TiO_2 catalyst using an environmentally friendly microwave-assisted solvothermal method," *Chinese Journal of Catalysis 38,* p. 1680–1687, 2017.

[160] W. Yuan, J. Li, L. Wang, P. Chen, A. Xie and Y. Shen, "Nanocomposite of n-doped TiO_2 Nanorods and Graphene as an Effective Electrocatalyst for the Oxygen Reduction Reaction," *ACS Appl. Mater. Interfaces 6,* p. 21978−21985, 2014.

[161] N. Royaei, T. Shahrabi and Y. Yaghoubinezhad, "The investigation of the electrocatalytic and corrosion behavior of a TiO_2–RuO_2 anode modified by graphene oxide and reduced graphene oxide nanosheets via a sol–gel method," *Catal. Sci. Technol., 8,* pp. 4957- 4974, 2018.

[162] B. Nagy, I. Bakos, I. Bertóti, A. Domán, Alfréd Menyhárd, Miklós Mohai and Krisztina László, "Synergism of nitrogen and reduced graphene in the electrocatalytic behavior of resorcinol - Formaldehyde based carbon aerogels," *Carbon 139,* pp. 872-879, 2018.

[163] G. Yang, Q. Fan, B. Chen, Q. Zhou and H. Zhong, "Reprecipitation synthesis of luminescent $CH_3NH_3PbBr_3$/$NaNO_3$ nanocomposites with enhanced stability," *J. Mater. Chem. C,,* vol. 4, pp. 11387-11391, 2016.

[164] T. Bauer, D. Laing, U. Kröner and R. Tamme, "Sodium Nitrate for High Temperature Latent Heat Storage, Page 1 of 8," in *The 11th International Conference on Thermal Energy Storage – Effstock 1*, Stockholm, Sweden, 2009.

[165] J. A. Navio, M. Macias, A. Justo and C. Real, "THERMAL DECOMPOSITION OF SODIUM NITRITE AND SODIUM NITRATE PRE-ADSORBED ON TiO_2 SURFACES," *Journal of Thermal Analysis,* vol. Vol. 38, pp. 673-682, 1992.

[166] George Feick and R. M. Hainer, "On the Thermal Decomposition of Ammonium Nitrate. Steady-state Reaction Temperatures and Reaction Rate," *J. Am. Chem. Soc.,* Vols. 76, 22, pp. 5860-5863, 1954.

[167] Z. Sebestyen, Z. May, . K. Reczey and E. Jakab, "The effect of alkaline pretreatment on the thermal decomposition of hemp," *J Therm Anal Calorim 105,* p. 1061–1069, 2011.

[168] Z. Li, B. Yang, S. Zhang and C. Zhao, "Graphene oxide with improved electrical conductivity for supercapacitor electrodes," *Applied Surface Science 258,* p. 3726– 3731, 2012.

[169] R. Wang, Y. Tang, M. Xu, C. Meng and F. LI, "Transfer Hydrogenation of aldehydes and ketones with isopropanol under neutral conditions catalyzed by a metal–ligand bifunctional catalyst [Cp*Ir(2,2′-bpyO)(H_2O)]," *J. Org. Chem. 83, 4,* pp. 2274-2281, 2018.

[170] A. V. Talyzin, V. L. Solozhenko, O. O. Kurakevych, T. S. Szabó, I. Dékány, A. Kurnosov and V. Dmitriev, "Colossal Pressure-Induced Lattice Expansion of Graphite Oxide in the Presence of Water," *Angewandte Chemie International Edition. 47 (43):826871,* vol. PMID 18814163, 2008.

[171] Á. Vass, "Szén-monoxid-tűrő katalizátorok tüzelőanyag-elemekhez," *PhD dissertation,* vol. Szegedi Tudományegyetem, 2019.

[172] R. Nagy, "Titán-Nióbium vegyes-oxid alapú hordozós katód elektrokatalizátorok tervezése Polimer Elektrolit Membrán Tüzelőanyag-cellákhoz.," 2017.

[173] F. Maillard, S. Schreier, M. Hanzlik, E. Savinova, S. Weinkauf and U. Stimming, "Influence of particle agglomeration on the catalytic activity of carbon-supported Pt nanoparticles in CO monolayer oxidation," *Phys. Chem. Chem. Phys. 7,* pp. 385-393, 2005.

[174] K. S. Sing and R. Williams, "Adsorption Science & Technology," vol. 22, no. No. 10, pp. 773-782, 2004.

[175] J. Baltrusaitis, B. Mendoza-Sanchez, V. Fernandez, R. Veenstra, N. Dukstiene, A. Roberts and N. Fairley, "Generalized molybdenum oxide surface chemical state XPS determination via informed amorphous sample model," *Appl Surf Sci 326,* pp. 151-161, 2015.

[176] D. O. Scanlon, G. W. Watson, D. J. Payne, G. R. Atkinson, R. G. Egdell and D. S. L. Law, "Theoretical and experimental study of the electronic structures of MoO_3 and MoO_2," *J. Phys. Chem. C 114,* p. 4636–4645, 2010.

[177] Y. Yamada, H. Yasuda, K. Murota, M. Nakamura, T. Sodesawa and S. Sato, *J. Mater. Sci. 48,* pp. 8171-8198, 2013.

[178] L. Stobinski, B. Lesiak, J. Zemek and P. Jiricek, *Appl. Surf. Sci. 258,* pp. 7912-7917, 2012.

[179] D. Diczházi, I. Borbáth, I. Bakos, G. Szijjártó, A. Tompos and Z. Pászti, *Catal. Today,* 2020.

[180] Hartmann SR and Hahn EL , "Nuclear double resonance in the rotating frame," *Phys Rev 128,* pp. 2042-205, 1962.

[181] B. Fung, A. Khitrin and K. Ermolaev, "An improved broadband decoupling sequence for liquid crystals and solids," *J Magn Reson 142,* pp. 97-101, 2000.

[182] N. Fairley, "CasaXPS: Spectrum Processing Software for XPS, AES and SIMS," Cheshire , 2006.

[183] M. Mohai, "XPS MultiQuant: Multimodel XPS Quantification Software," *Surf. Interface Anal., 36,* p. 828–832, 2004.

[184] M. Mohai, "XPS MultiQuant: Multi-model X-ray photoelectron spectroscopy quantification program," 2011.

[185] C. D. Wagner, A. V. Naumkin, A. Kraut-Vass, J. W. Allison, C. J. Powell and J. R. Rumble Jr., "NIST X-ray Photoelectron Spectroscopy Database," Gaithersburg, MD, 2003.

[186] J. Moulder, W.F. Stickle, P.E. Sobol and K.D. Bomben, Handbook of X-ray Photoelectron Spectroscopy, Minnesota, Minnesota: Perkin Elmer Corporation, 1992.

Statement of the internal supervisor

I, Krisztina László as internal supervisor, hereby declare that the thesis written by Ilgar Ayyubov, (Neptune code: EKUD43) entitled “Preparation and characterisation of Pt based electrocatalysts for PEM fuel cells” is his own writing and that I supported his work with regular consultations. I also declare that the thesis meets the formal and professional requirements of the Budapest University of Technology and Economics and those of the Faculty of Chemical Technology and Biotechnology, thus I support its submission.

Budapest, May 31st, 2020

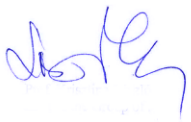

Statement of the external supervisor

I, András Tompos as external supervisor, hereby declare that the thesis written by Ilgar Ayyubov, (Neptune code: EKUD43) titled “Preparation and characterisation of Pt based electrocatalysts for PEM fuel cells” is his own writing prepared under my supervision. Based on its professional merits, I support its submission.

Budapest, June 3rd, 2020

Statement of the student

I, Ilgar Ayyubov (Neptun code: EKUD43) as author of the thesis hereby declare that my thesis titled “Preparation and characterisation of Pt based electrocatalysts for PEM fuel cells” is my original writing and I have not plagiarised any other work. All third-party materials including published and unpublished sources were referenced.

I acknowledge that the intellectual property rights of the methods used and the results of any research or development described in the thesis belong to the participating researchers and institutions/companies, thus their utilization or publication must not be initiated before the approval of all parties.

I also declare that during the preparation and writing the thesis I did not mislead my supervisor(s) and thesis advisor.

Budapest, May 29th, 2020